

**Photoinduced Charge Transfer
in a
Transition Metal Complex
Investigated by Time-Resolved X-ray
Absorption Fine Structure
Spectroscopy:
Setup and Experiment**

DISSERTATION

zur Erlangung des Doktorgrades des Fachbereichs Physik

der Universität Hamburg

vorgelegt von

DENNIS GÖRIES

Hamburg
2014

Gutachter der Dissertation:	Prof. Dr. E. Weckert Prof. Dr. M. Drescher
Gutachter der Disputation:	Prof. Dr. M. Rübhausen Prof. Dr. E. Weckert
Datum der Disputation:	03.07.2014
Vorsitzende des Prüfungsausschusses:	Prof. Dr. C. Hagner
Vorsitzende des Promotionsausschusses:	Prof. Dr. D. Pfannkuche
Dekan der MIN-Fakultät:	Prof. Dr. Heinrich Graener

Abstract

In the framework of this thesis the development of a time-resolved X-ray absorption spectroscopy experiment and its application to fac-Ir(ppy)₃ is described. Such experiments require a very stable setup in terms of spatial and temporal accuracy. Therefore, the stability properties of the present installation were investigated in detail and continuously improved, in particular the synchronization of the ultrashort pulse laser system to the storage ring as well as the spatial stability of both X-ray and laser beam. Experiments utilizing the laser pump and X-ray probe configuration were applied on the green phosphorescence emitter complex fac-Ir(ppy)₃ dissolved in dimethyl sulfoxide. Structural and electronic changes were triggered by photoexcitation of the metal-to-ligand charge transfer band with ultrashort laser pulses at a wavelength of 343 nm. The excited triplet state spectrum was extracted from the measured pump-probe X-ray absorption spectrum using an ionic approximation. The results confirm the anticipated metal-to-ligand charge transfer as shown by an ionization potential shift of the iridium atom. The symmetry of the complex was found to be pseudo-octahedral. This allowed the first experimental determination of the bond length of fac-Ir(ppy)₃ in an octahedral approximation and revealed a decrease of bond length of the first coordination shell in the triplet state. The first and second-order decay kinetics of the triplet state were investigated in a combination of X-ray and laser based experiments and revealed self-quenching as well as triplet-triplet annihilation rate constants.

Kurzfassung

Im Rahmen dieser Arbeit wird die Entwicklung eines Experiments für zeitaufgelöste Röntgenabsorptionsspektroskopie beschrieben. Erste erfolgreiche Experimente wurden mit diesem Aufbau an fac-Ir(ppy)_3 durchgeführt und die Ergebnisse werden im Rahmen dieser Arbeit präsentiert. Für diese Experimente ist ein sehr stabiler Aufbau notwendig. Daher wurde die Synchronisation des Lasersystems zum Speicherring und die räumliche Stabilität vom Röntgen- und Laserstrahl im Detail untersucht und kontinuierlich verbessert.

Der Triplett-Zustand des grünen Phosphoreszenzemitters fac-Ir(ppy)_3 wurde mit der *Anregungs-Abfrage-Technik* genauer untersucht. Für diesen Zweck wurden die strukturellen und elektronischen Änderungen durch einen optisch angeregten Ladungstransfer vom Iridiumatom zu den Liganden bei einer Wellenlänge von 343 nm induziert. Das Röntgenabsorptionsspektrum des angeregten Triplett-Zustands konnte von dem gemessenen *Pump-Probe-Spektrum* durch eine ionische Näherung bestimmt werden. Die Resultate bestätigen den vorhergesagten Ladungstransfer vom Iridiumatom zu den Liganden durch eine gezeigte Verschiebung des Ionisierungspotentials vom Iridiumatom. Die Symmetrie des Komplexes wurde als pseudo-oktahedrisch vorgefunden. Dies erlaubte die erste experimentelle Bestimmung der Bindungslänge von fac-Ir(ppy)_3 in einer oktahedrischen Näherung und zeigte eine Verkürzung der Bindungslänge der ersten Koordinationshülle im Triplett-Zustand. Anschließend wurden die ersten und zweiten Ordnungen der kinetischen Zerfälle des Triplett-Zustandes in einer Kombination aus Röntgen- und Laser-Experimenten untersucht. Dabei konnten die entsprechenden Selbstlöschungs- und Triplett-Triplett Annihilations Ratenkonstanten bestimmt werden.

Inhaltsverzeichnis

1. Introduction	1
2. Theory of X-ray Absorption Fine Structure Spectroscopy	3
2.1. Introduction to X-ray Absorption Fine Structure Spectroscopy	4
2.1.1. Near-Edge Structure and Multiple-Scattering Resonances	5
2.1.2. X-ray Absorption Fine-Structure Region	8
2.1.3. Decay of Excited Atomic States	10
2.2. Experimental Static XAFS	11
2.2.1. X-ray Transmission Mode	11
2.2.2. X-ray Fluorescence Yield Mode	12
2.3. Time-Resolved Pump and Probe XAFS	14
2.3.1. Transient Transmission Signal	14
2.3.2. Transient Fluorescence Signal	15
2.3.3. Estimation of the Initial Excitation Yield	16
2.3.4. Statistical Aspects	17
3. The Transition Metal Complex fac-Ir(ppy)₃	19
3.1. Ground State Structure	19
3.2. Molecular Orbital Diagram and Electronic Structure	20
3.3. UV/VIS Absorption and Emission Spectroscopy	23
3.4. Photocycle of the Metal-to-Ligand Charge Transfer	24
4. Experimental Infrastructure	27
4.1. Synchrotron Radiation X-ray Source PETRA III	27
4.1.1. Working Principle of a Synchrotron Radiation Source	27
4.1.2. Important Synchrotron Quantities	29
4.2. Beamline P11 at PETRA III	31
4.2.1. Undulator Radiation	31
4.2.2. Double Crystal Monochromator	33
4.2.3. High-End Focusing KB Mirror System	34
4.2.4. Experimental Hutch	35
5. Experimental XAFS Setup	37
5.1. Setup Overview	38
5.2. Ultrashort Pulse Lasersystem	39
5.3. Micro-Jet System	40
5.4. On-Axis Microscope	41
5.5. Beam defining Pinhole	42
5.6. Detectors	43
5.6.1. Photon Flux Measurements - Silicon Photodiode	43

5.6.2. X-ray Fluorescence Measurements - Avalanche Photodiode . . .	44
5.7. Data Acquisition Scheme	47
5.7.1. Gating Structures for Bunch Selection	48
5.8. Principle of Spatial and Temporal Overlap	49
5.9. Optimization of the Avalanche Photodiode Signal	51
6. Synchronization and Stability	53
6.1. Theory and Principle of Feedback Control	53
6.1.1. Properties and Modifications of Control Algorithms	54
6.2. Theory of Phase Noise and Signal Source Analyzers	56
6.2.1. Measurement of Phase Noise with Signal Source Analyzers . . .	57
6.2.2. Relationship between Phase Noise and Timing Jitter	58
6.3. Synchronization in Time-Resolved Pump and Probe Experiments	59
6.3.1. Characterization of the RF Signal	59
6.3.2. Laser Oscillator Synchronization	60
6.3.3. Laser Amplifier Synchronization	66
6.4. Laser Feedback	68
6.5. X-ray Feedback	70
6.5.1. Spatial X-ray Beam Stability at Beamline P11	73
7. Time-Resolved Pump and Probe X-ray Absorption Fine Structure Spectro-	
scopy Experiments	83
7.1. Ground State XAFS	83
7.2. Excited State XAFS	85
7.2.1. Spectral Resonance Fitting and Analysis	88
7.3. Time-Resolved XAFS	94
7.3.1. Temporal Resolution - X-ray Bunch Length	95
7.3.2. Excited State Lifetime - Second-Order Decay Kinetics	97
7.4. Influence of Laser Fluence - Excitation Threshold	100
8. Summary and Outlook	103
A. Example of a Deglitching Process	107
B. Optical Spectroscopy - Molar Extinction Coefficients	109
C. Optical Lifetime Measurements - First-Order Decay Kinetics	111
D. Calculation of the Excitation Yield Maximum	115
E. Calculation of the Excitation Yield	119
F. Spectrochemical Series	123
Bibliography	129

1. Introduction

Third generation X-ray radiation¹ sources can be utilized for structural and electronic characterization of materials with techniques such as X-ray absorption² or emission spectroscopy and X-ray crystallography. The gathering and determination of structural and electronic properties of molecular systems can sustain and provide information to our understanding of their functions. Accompanied by the technical development the structural techniques are nowadays transferred to the time domain utilizing the laser pump and X-ray probe configuration to gather information about the photoinduced transient structures^{3,4}.

Amongst others the effort is based on the motivation to establish a basis of knowledge to design and synthesize new compounds with prior determined functions, which is referred to as *molecular engineering*⁵.

It was the goal of the present work to setup and establish an X-ray absorption spectroscopy setup for time-resolved experiments at beamline P11 at the PETRA III storage ring in Hamburg^{6,7}. With regard to future planned time-resolved *photocrystallography* experiments⁸, the spectroscopy setup marks a first milestone for transient structure analysis in the picosecond time domain at PETRA III and can be utilized for charge transfer detection in transition metal complexes^{3,4,9,10}. In addition, with the advent of the fourth generation X-ray radiation sources such as the European XFEL¹¹, this setup can also be regarded as an educational tool for future pump and probe experiments¹² in the femtosecond time domain.

Recently the study of materials which are used for organic light emitting diodes (OLED) has drawn intense attention in spectroscopic and diffraction experiments to investigate their ground states and - to a certain extend - their excited states^{13,14}. In particular a broad class of phosphorescent iridium(III) complexes such as Ir(ppy)₃¹³⁻²¹, Ir(piq)₃²² and FIrpic etc., which are commonly used as emissive dopants in OLED applications, are investigated¹⁴. This class of complexes refers to an ideal representative of molecular engineering since the attachment of different ligands to the central iridium atom leads to completely different properties¹⁴.

For this reason, the green emissive dopant Ir(ppy)₃, which is anticipated to exhibit a strong metal-to-ligand charge transfer character^{13,16}, was chosen as a model compound to prove the utilizability of the developed X-ray absorption experiment.

Time-resolved pump and probe experiments require a very stable setup. Therefore, the stability properties of the present setup were investigated in detail, in particular the synchronization of the ultra-short pulse laser system to the storage ring as well as the spatial stability of both X-ray and laser beam. Results obtained by time-resolved X-ray absorption experiments were further supported by UV/VIS spectroscopic experiments and various numerical calculations.

1. Introduction

This thesis is organized in the following way: Following the introduction, the next chapter briefly introduces into general aspects of X-ray absorption spectroscopy and the extension of the latter to time-resolved experiments based on previous work in this field.

Chapter 3 features a detailed description of the metal organic compound $\text{Ir}(\text{ppy})_3$, including static optical spectroscopy, molecular orbital diagram and the photocycle which was further investigated in this thesis.

In the subsequent chapter the experimental infrastructure, in particular beamline P11 at the synchrotron source PETRA III and key elements of a synchrotron storage ring with their theoretical properties, is described.

Chapter 5 describes the developed X-ray absorption spectroscopy setup and introduces into the temporal and spatial overlap strategy of X-ray and pump laser beam.

Chapter 6 introduces into the theory of feedback control mechanism followed by its applications on the spatial stability of X-ray and laser beam. The characterization of the synchronization between the pump laser system and synchrotron is also part of this chapter.

The time-resolved X-ray absorption studies of $\text{Ir}(\text{ppy})_3$ and the obtained results are presented in Chapter 7. This includes the description of structural and electronic changes in $\text{Ir}(\text{ppy})_3$ triggered upon photoexcitation as well as time-scans where the laser pulse is temporally shifted with respect to the X-ray bunch to characterize the second-order decay kinetics of the triplet state. These experiments further allowed to determine the PETRA III bunch length. Finally, the results are summarized and improvements of the setup are discussed. Various numerical calculations and accompanied UV/VIS experiments are given in the appendices.

2. Theory of X-ray Absorption Fine Structure Spectroscopy

2.1. Introduction to X-ray Absorption Fine Structure Spectroscopy	4
2.1.1. Near-Edge Structure and Multiple-Scattering Resonances	5
2.1.2. X-ray Absorption Fine-Structure Region	8
2.1.3. Decay of Excited Atomic States	10
2.2. Experimental Static XAFS	11
2.2.1. X-ray Transmission Mode	11
2.2.2. X-ray Fluorescence Yield Mode	12
2.3. Time-Resolved Pump and Probe XAFS	14
2.3.1. Transient Transmission Signal	14
2.3.2. Transient Fluorescence Signal	15
2.3.3. Estimation of the Initial Excitation Yield	16
2.3.4. Statistical Aspects	17

*"X-ray Absorption Fine Structure (XAFS) spectroscopy is a unique tool for studying, at the atomic and molecular scale, the local structure around selected elements that are contained within a material"*²⁸.

The main research within this framework is based on this spectroscopic technique and therefore this chapter briefly introduces the theoretical background and the experimental detection of XAFS.

This chapter follows in great detail the introductory reference given by M. Newville^{23,24i} and refers to S. Bare²⁵, F. Sette *et al.*²⁶ or Rehr *et al.*²⁷ and other literature²⁸⁻³¹ to provide further information.

The sections related to time-resolved pump and probe XAFS are mainly based on C. Bressler *et al.*³² and previous work in the field of time-resolved X-ray absorption spectroscopy^{6,33,34}. The outline is inspired by previous work.

ⁱBoth references can be compared vice versa. In the framework of this thesis mainly reference²³ is used.

2.1. Introduction to X-ray Absorption Fine Structure Spectroscopy

"The basic physical quantity that is measured in XAFS is the absorption coefficient $\mu(E)$, which describes how strongly X-rays are absorbed as a function of the X-ray energy E "²⁸.

The absorption coefficient is described by a smooth function of X-ray energy ($\approx 1/E^3$) and further characterized by *element-specific absorption edges*, which are noticeable by a sharp increase in absorption²³ⁱⁱ. These spectral features are of fundamental importance²³ and illustrated in Fig. 2.1 for the element iridium. The absorption edges shown are the K ($n=1$) and L-edge ($n=2$), in which the former refers to an excitation of the $1s_{1/2}$ core electron while the L-edge describes the promotion of a core electron from the $2s_{1/2}$ (L_1) or $2p_{1/2}$ (L_2) and $2p_{3/2}$ (L_3) orbital to continuum²⁵. The transition to an excited atomic state requires an incident X-ray photon with an energy corresponding to the binding energy of a core electron residing in an atomic core level²³.

The element-specific transitions of core electrons can be utilized in X-ray absorption spectroscopy to gather not only electronic but also structural or geometrical information of complexes.

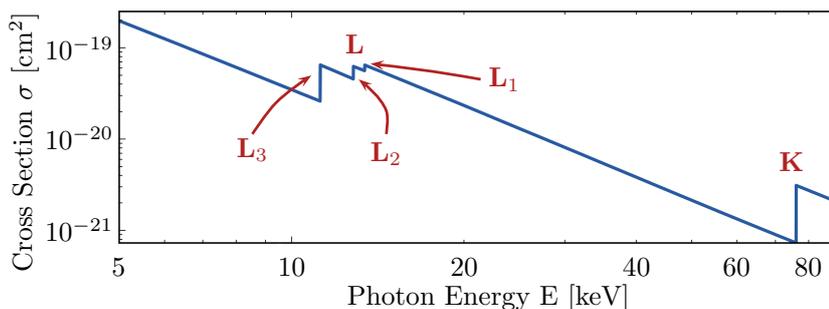


Figure 2.1.: Illustrated X-ray absorption cross section σ of iridium as a function of the X-ray energy E (log-log). The absorption edges of the respective core electrons (K, L) can be identified by a sharp increase in the absorption cross section²³. The X-ray absorption cross sections were calculated using the software XOP³⁵. The figure is based on reference²⁸.

For this purpose, the absorption coefficient is measured as a function of the X-ray energy, yielding an X-ray absorption spectrum. The common experimental techniques are transmission and fluorescence detection, which will be explained in Sec. 2.2.

A hypothetical K-edge XAFS spectrum of a transition metal complex is illustrated in Fig. 2.2, where the position of the absorption edge is denoted with E_0 . Details of the spectrum will be explained in the following sections on the basis of the regions of interest, which are depicted in their photon energy range.

The *X-ray Absorption Near-Edge Structure* (XANES) region is commonly defined up to ~ 50 eV above the absorption edge³⁰ⁱⁱⁱ. The accompanied energy region, which is

ⁱⁱCompare also to reference²⁸.

ⁱⁱⁱNewville²³ assigns the XANES region to within 30 eV of the main absorption edge, while Bare²⁵ characterizes the XANES region as ~ 50 eV around the absorption edge.

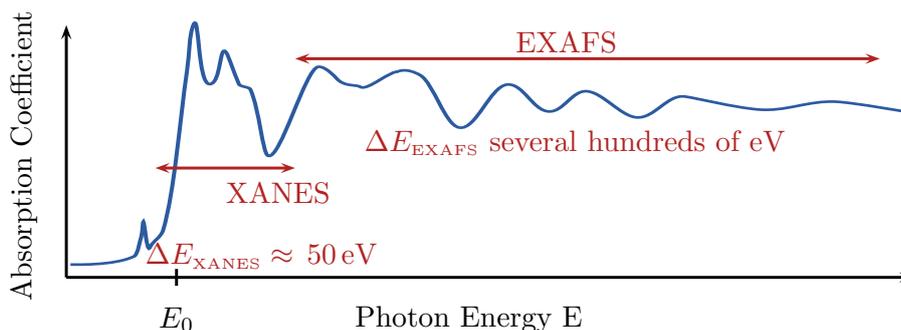


Figure 2.2.: Hypothetical normalized K-edge spectrum of a transition metal complex. The regions XANES and EXAFS are marked in their photon energy range. E_0 : Approximated position of the threshold energy.

typically extending up to several hundreds of eV above the absorption edge, describes the fine structure in the absorption coefficient and is therefore called *Extended X-ray Absorption Fine-Structure* (EXAFS)³⁰.

2.1.1. Near-Edge Structure and Multiple-Scattering Resonances

The absorption of an X-ray photon is related to the *photoelectric effect*²³. Whenever X-ray radiation is absorbed by an atomic core level with a specific binding energy, a pair of a photoelectron (former denoted as core electron) and a core hole are created²³. However, there will be no absorption from an atomic core level if there is no available state with the correct energy and angular momentum for the photoelectron, except the energy of the photoelectron is high enough to be promoted to continuum, thus leaving the atom²³. The absorption coefficient $\mu(E)$ can therefore be described by *Fermi's Golden Rule*²³:

$$\mu(E) \propto |\langle f | \mathcal{H} | i \rangle|^2, \quad (2.1)$$

where $|i\rangle$ denotes the initial state, $\langle f|$ the final state and \mathcal{H} the interaction term. In general, the transitions follow the dipole selection rules²⁵:

$$\begin{aligned} \text{orbital angular momentum quantum number } l & \quad \Delta l = \pm 1, \\ \text{total angular momentum quantum number } j & \quad \Delta j = \pm 1, 0. \end{aligned}$$

There exist minor exceptions for the so-called *pre-edges*, where also quadrupolar transitions have to be taken into account (see below)²⁵. The core electrons are strongly bound to the atomic core levels of the absorber, which implies that neighboring atoms are not affecting the initial states²³. In strong contrast, generated photoelectrons will see the distortion of the final states on their way up to the continuum²³.

The magnified XANES part is illustrated in Fig. 2.3, showing the respective features according to Tab. 2.1.

Since the XANES region does not provide any *characteristic* (visible) feature at the

2. Theory of X-ray Absorption Fine Structure Spectroscopy

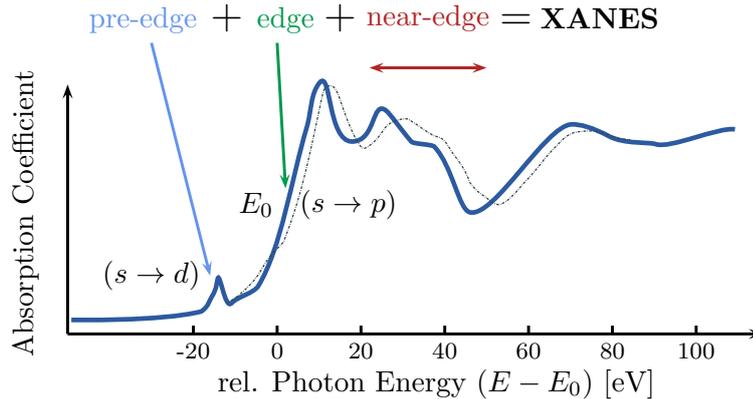


Figure 2.3.: Magnified XANES part of the XAFS spectrum previously shown in Fig. 2.2. A simplified shift of the XANES part to higher energies (blue shift) is shown as a dashed curve, referring to an increase of the oxidation state of the absorbing atom²⁵. E_0 : Approximated position of the threshold energy. The features are denoted according to the notation from Tab. 2.1. The figure is based on reference²⁵.

ionization energy E_0 ^{30iv}, the threshold is in this example typically approximated as the first inflection point on the edge resonance⁴⁸.

Transitions of photoelectrons to empty bound states below the edge resonance occur as pre-edges, whose shape and position can provide information on the geometry around the element under investigation²⁵. As mentioned, this implies the availability of an empty bound state with the right angular momentum, which is typically the case for transition metals at K-edges²⁵. In this example the pre-edge intensity is relatively low, indicating a transition metal complex with a pure octahedral symmetry, allowing only quadrupolar transitions of the photoelectron to empty bound states below the edge²⁵. The edge resonance arises in consequence of dipole allowed transitions of photoelectrons to empty bound states^{25v}. It was shown in several experiments that the energy position of the edge²⁵ (first inflection point) correlates with the formal valency of the absorber and thus the ionization threshold E_0 ³⁶. Depending on the oxidation state, e.g. by increasing the oxidation state, the edge position is shifted to higher energies (illustrated as dashed curve in Fig. 2.3)²⁵, which is commonly referred to as *chemical shift*^{25,36}. Furthermore, the transitions of photoelectrons are sensitive to spin-orbit effects, which can provide information on the molecular symmetry³⁷.

In the *near-edge* region so-called *multiple-scattering resonances* can occur, which will be explained in the following²⁵.

If the incident X-ray photon energy is larger than the specific absorption edge energy, the generated photoelectron will leave the absorbing atom and can be treated as a spherical wave²³

$$\Psi(k, r) = \frac{e^{ikr}}{kr}, \quad (2.2)$$

^{iv}The literature further arguments with a weak density of states at the threshold energy.

^vCompare also to reference³⁷.

where k is the photoelectron wavenumber, given by²³

$$k = \sqrt{\frac{2m_e(E - E_0)}{\hbar^2}}. \quad (2.3)$$

Thereby, m_e denotes the electron mass and \hbar the reduced *Planck* constant. The photoelectron wavenumber can be translated to the photoelectron wavelength λ_e via $k = 2\pi/\lambda_e$ to

$$\lambda_e(k) = \frac{h}{\sqrt{2m_e(E - E_0)}}, \quad (2.4)$$

$$\lambda_e(k) \propto (E - E_0)^{-1/2}. \quad (2.5)$$

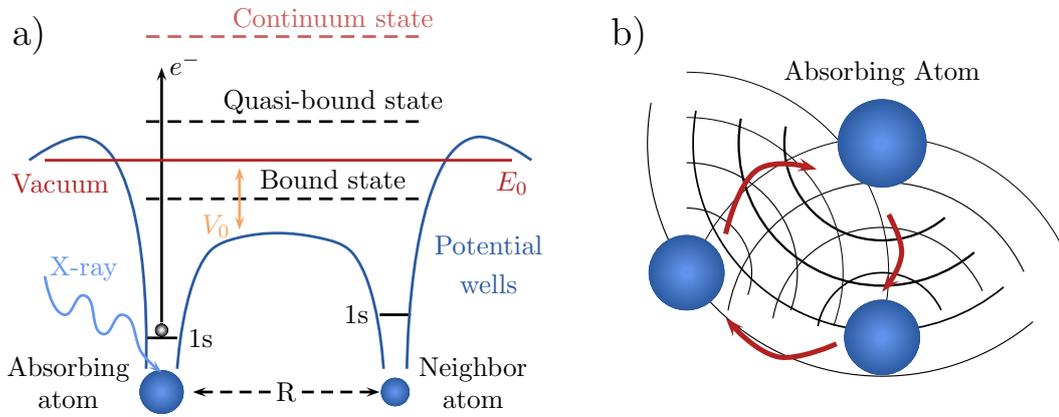


Figure 2.4.: **a)** Illustrated potential wells of a diatomic molecule, in which the energies are referenced to the threshold energy E_0 . The potential between the two atoms, separated by the interatomic distance R , is denoted as V_0 and nearly constant. Its separation from E_0 is denoted as the *inner potential*²⁶. The figure is redrawn and based on reference²⁶. **b)** Multiple-scattering path (red) of a photoelectron wave leaving the absorbing atom and subsequently getting scattered off by neighboring atoms. After each bounce the amplitude of the scattered photoelectron wave decreases²⁷. The figure is redrawn and based on reference²⁷.

In the near-edge region the kinetic energies of the photoelectrons are rather small ($E_{\text{kin}} = E - E_0 \leq 30 \text{ eV}$) and the transitions of the photoelectrons are significantly influenced by the core and valence electron potentials of the absorber and its neighboring atoms²⁶. Besides transitions of photoelectrons to empty bound states below or near the threshold energy E_0 further transitions can occur, which is exemplarily shown in Fig. 2.4 in case of a diatomic molecule²⁶.

At low energies above the threshold energy, multiple-scattering resonances arise in consequence of transitions of photoelectrons to quasi-bound states, which are trapped by potentials originating from the valence electrons, in the continuum²⁶. These spectral resonances are further described in the literature²⁶ as a back-and-forth scattered photoelectron wave between the absorber and its neighboring atoms. However, the

2. Theory of X-ray Absorption Fine Structure Spectroscopy

probability of a resonantly scattered photoelectron wave depends on the type of the molecular system²⁶. In a more common picture the excited photoelectron is multiple diffracted by neighboring atoms, which is illustrated in Fig. 2.4b in case of a triangular path^{27vi}. Consequently the amplitudes of all the backscattered photoelectron waves in the vicinity of the absorber add either destructively or constructively to the further outgoing photoelectron wave, which modulates the transition probability between the initial and final states and thus the absorption coefficient (see Eq. 2.1)²⁷. These *multiple-scattering interference effects* are sensitive to the interatomic distances and bond angles etc., as can be seen from Fig. 2.4²⁶. A quantitative analysis of these spectral features is not straightforward but can provide a deeper insight into the structural arrangements around the element under investigation. The reader is referred to the literature^{26,27} for further information. The most interesting features and their information are summarized in Tab. 2.1.

Table 2.1.: Summarized XANES information according to the respective feature (Table is adapted and the information is taken from reference²⁵).

Region	Transitions	Information
pre-edge	Features transitions of photoelectrons to empty bound states. The transitions are governed by dipole selection rules, however, quadrupolar transitions are possible ($ \Delta l = 2$).	Provides information on the local geometry around the absorbing atom. For example in transition metal complexes at K-edges, the pre-edge intensity depends on the symmetry. Regarding a complex with a pure octahedral symmetry only quadrupolar transitions are allowed. With increasing distortion to tetrahedral alignment the pre-edge amplitude rises due to hybridization of p and d orbitals, allowing dipole transitions in the pre-edge.
edge	Electronic transitions follow dipole selection rules ($ \Delta l = 1$). Typically approximated as the ionization threshold to continuum states.	Position depends on oxidation state (chemical shift) of the absorbing atom.
near-edge	Dominated by multiple-scattering features.	Provides information on the atomic position of neighbors: bond angles and distances.

2.1.2. X-ray Absorption Fine-Structure Region

As described in the previous section, the photoelectrons leaving the absorbing atom are subsequently scattered by neighboring atoms and return to the absorber modu-

^{vi}The amplitude of the photoelectron wave decreases after each bounce²⁷.

lating the transition probability between the initial and final states via interference effects and thus the absorption coefficient. This phenomenon is referred to as the origin of XAFS²³. In the near-edge region the modulation of the absorption coefficient is referenced to complex multiple-scattering paths of the photoelectrons along the inter-nuclear axis before they return to the absorber as described in Sec. 2.1.1 and shown in Fig. 2.4b^{26,27}.

In the fine structure region, however, the prominent type of photoelectron scattering is their reflection by neighboring atoms directly back to the absorber, which is referred to as single scattering or simply backscattering²⁷. The description follows and summarizes now the introductory reference^{23,24vii}.

The *EXAFS* (fine-structure) function $\chi(E)$ is defined as

$$\chi(E) = \frac{\mu(E) - \mu_0(E)}{\Delta\mu_0}, \quad (2.6)$$

where $\mu(E)$ is the (measured) absorption coefficient, $\mu_0(E)$ is a smooth background function which represents the absorption of an isolated atom and $\Delta\mu_0$ is the (measured) absorption jump at the threshold energy E_0 .

To derive a general expression for the fine structure, the photoelectron wavefunction is described as a damped spherical wave

$$\Psi(k, r) = \frac{e^{ikr} e^{-2r/\lambda(k)}}{kr}, \quad (2.7)$$

where λ now represents the mean free path of the photoelectron. With this description only travel distances of the photoelectron are considered before it scatters inelastically and before the excited atomic state decays, thus accounting for the core-hole lifetime. The *EXAFS Equation*, in terms of the photoelectron wavenumber k , can then be derived as

$$\chi(k) = \sum_j \frac{N_j e^{-2k^2\sigma_j^2} e^{-2R_j/\lambda(k)} f_j(k)}{kR_j^2} \sin[2kR_j + \delta_j(k)], \quad (2.8)$$

where j denotes the coordination shell of identical atoms N_j at approximately the same distance R_j from the excited atom. Furthermore, $f_j(k)$ and $\delta_j(k)$ are scattering properties of the neighboring atoms and the factor σ_j^2 describes their disorder in distance²³. In addition, an amplitude reduction term S_0^2 is introduced to account for the relaxation of other core electrons (not the photoelectron) into the empty core hole:^{viii}

$$\chi(k) = \sum_j \frac{N_j S_0^2 e^{-2k^2\sigma_j^2} e^{-2R_j/\lambda(k)} f_j(k)}{kR_j^2} \sin[2kR_j + \delta_j(k)]. \quad (2.9)$$

As can be seen in Eq. (2.9), the $\chi(k)$ spectrum consists of a sum of sine waves, which leads to use a Fourier transformation of the spectrum to determine the interatomic

^{vii}Furthermore, the reader is referred to reference²⁹ which describes a free-photoelectron assumption based on the effective average potential (inner potential) V_0 experienced by the photoelectrons on their way up to continuum (see Fig. 2.4). Thereby, the band effects, formerly described in a diatomic molecule as potentials from the valence electrons, are at sufficient energies above the Fermi level (≥ 50 eV) of minor relevance and therefore also the multiple-scattering effects decrease.²⁹

^{viii}The amplitude reduction term is typically chosen as a constant ($0.7 < S_0^2 < 1$).

2. Theory of X-ray Absorption Fine Structure Spectroscopy

distances R_j between the absorber and the surrounding coordination shells³⁸. In order to perform a quantitative analysis, the scattering amplitude $f(k)$ and phase-shifts $\delta(k)$ are typically determined by softwares³⁹ such as *FEFF*. For a detailed description of XAFS data handling the reader is referred to the literature^{23,28}.

2.1.3. Decay of Excited Atomic States

After the absorption of an X-ray photon the atom is referred to be in an excited state²³. The excited atomic state then decays by either a radiative or nonradiative transition³¹, the *X-ray fluorescence* and the *Auger effect*, respectively, which can be eventually utilized to determine the absorption coefficient during measurements, since both processes are proportional to the absorption of X-rays²³.

The radiative decay is more probable for heavy atoms while the nonradiative decay is more likely for light atoms³¹. The following description is taken from the literature²³.

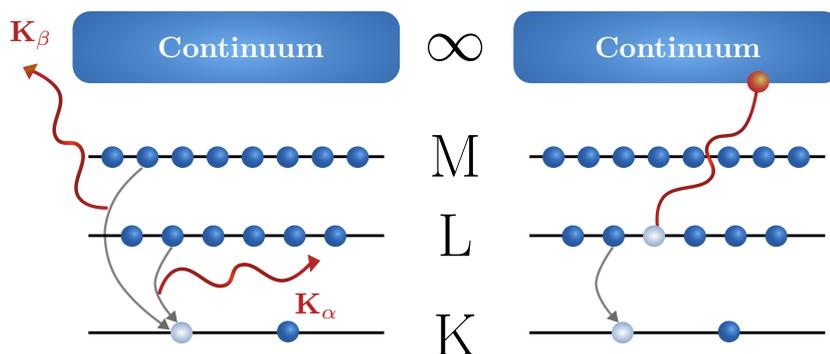


Figure 2.5.: X-ray fluorescence (left) and the Auger effect (right) during the excited state decay of an atom. The figure is adapted from reference²³.

The X-ray fluorescence and the Auger effect are illustrated in Fig. 2.5. Regarding the X-ray fluorescence in Fig. 2.5, the core hole is filled by a higher lying core electron, which results into the emission of an X-ray fluorescence photon with a well-defined energy. The emission lines and efficiencies of the X-ray fluorescence photons are tabulated in the literature^{40,41}. In this example the emission lines K_α and K_β are shown, which are related to the transition of a core electron from the L or M-shell to the lowest K-shell, respectively. In case of an iridium atom the average fluorescence efficiency at the L-edges is ≈ 0.3 ^{40,41}.

The Auger effect describes the transition of a higher lying core electron into the empty core hole, which results into the promotion of a second core electron, denoted as *Auger electron*, to the continuum.

2.2. Experimental Static XAFS

In the following sections the X-ray transmission- and X-ray fluorescence yield mode are briefly introduced on the basis of the sample geometry used within this thesis. Thereby, the total absorption coefficient $\mu_{\text{tot}}(E)$ of the whole sample is considered for the respective detection mode²³:

$$\mu_{\text{tot}}(E) = \mu_{\chi}(E) + \mu_{\text{other}}(E), \quad (2.10)$$

where $\mu_{\chi}(E)$ denotes the absorption of the element of interest and $\mu_{\text{other}}(E)$ is the absorption of the other atoms (solvent etc.).

2.2.1. X-ray Transmission Mode

The geometry of the X-ray transmission mode is illustrated in Fig. 2.6 and the following description is based on and summarizes the literature^{23,24}.

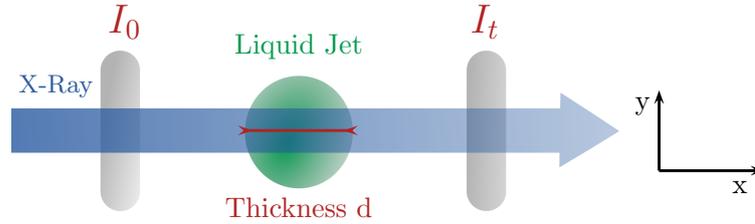


Figure 2.6.: Sketched geometry of the sample (liquid jet) with respect to the incident X-ray beam and the detectors in X-ray transmission mode. This method requires two linear detectors for incident intensity I_0 and transmitted intensity I_t measurements.

The absorption coefficient is determined by measuring the incident X-ray intensity $I_0(E)$ and transmitted X-ray intensity $I_t(E)$ through a sample of thickness d . Hence, the absorption is described by the well-known *Lambert-Beer law*:

$$I_t(E) = I_0(E) e^{-\mu_{\text{tot}}(E)d}. \quad (2.11)$$

Although the existing sample is a circular liquid jet implying a non-uniform thickness, the mathematical description treats the thickness uniformly to follow the literature ($d \rightarrow d'$). The absorption coefficient can therefore be derived by

$$\begin{aligned} \mu_{\text{tot}}(E)d' &= -\ln\left(\frac{I_t(E)}{I_0(E)}\right), \\ \mu_{\text{tot}}(E)d' &= \ln\left(\frac{I_0(E)}{I_t(E)}\right). \end{aligned} \quad (2.12)$$

From an experimental point of view the transmission mode represents a fairly simple way to measure the absorption coefficient because sample and detector alignment are pretty straightforward. The transmission mode requires the application of linear detectors and a homogeneous sample.

2. Theory of X-ray Absorption Fine Structure Spectroscopy

In case of a concentrated sample ($\mu_\chi \geq \mu_{\text{other}}$), XAFS measurements are normally performed in X-ray transmission mode and the sample thickness is typically adjusted to

$$d' \approx \frac{2.5}{\mu_{\text{tot}}(E \geq E_0)}, \quad (2.13)$$

for energies above the ionization threshold E_0 . For thin or dilute thick samples it is beneficial to detect the X-ray fluorescence instead of the transmitted intensity.

2.2.2. X-ray Fluorescence Yield Mode

The geometry of the X-ray fluorescence yield mode is illustrated in Fig. 2.7 and the following description is based on and summarizes the literature²³ if not stated otherwise.

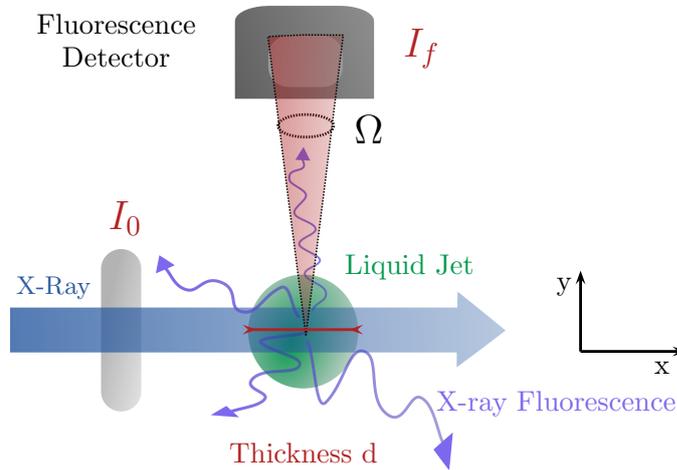


Figure 2.7.: Sketched geometry of the X-ray fluorescence yield mode showing the sample (liquid jet), the detector and the incident X-ray beam utilized in X-ray fluorescence yield mode. Ω : Detector solid angle. The figure is based on reference^{23,42}.

In contrast to the X-ray transmission mode this method exhibits one further consideration, the detector solid angle Ω . The emerging fluorescence photons from the sample are emitted isotropically, thus the detector solid angle Ω covers only a fraction of the total X-ray fluorescence intensity. Furthermore, the generated elastic scattering from the X-ray beam is not emitted isotropically due to the inherent horizontal polarization of the X-ray beam in the plane of the synchrotron. The polarization implies that the intensity of the elastically scattered photons is significantly reduced at a right angle with respect to the incident X-ray beam in the plane of polarization. Hence, this detection mode requires a careful alignment of the fluorescence detector to reduce elastic scattering contributions in the measured fluorescence yield.

In an oversimplified expression the absorption coefficient of the element of interest μ_χ

is proportional to the fluorescence intensity normalized to the incident intensity I_0 ^{ix}:

$$\mu_\chi(E) \propto \frac{I_f(E)}{I_0(E)}. \quad (2.14)$$

However, the generated fluorescence photons have to travel through the sample along the y direction to the detector, which damps the fluorescence intensity due to the *self-absorption effect*.

Regarding Fig. 2.7, the effective optical path for the incident intensity is approximated by $x \approx z/\alpha$ to describe the sample thickness, while the optical path for the generated fluorescence photons can be introduced as $y \approx z/(\alpha\beta)$. Both geometrical factors α and β are needed to derive an expression for the present sample geometry similar to existing literature^x.

Therefore, we can define our fluorescence intensity from a slice dz at a depth z_n in the sample as follows^{31,42xi}

$$dI_f(E, z_n) = I_0(E) e^{-(\mu_{\text{tot}}(E)z_n/\alpha_n)} \frac{\Omega}{4\pi} \varepsilon_\chi \Phi \mu_\chi(E) e^{-(\mu_{\text{tot}}(E_f)z_n/(\alpha_n\beta_n))} \frac{dz_n}{\alpha_n}, \quad (2.15)$$

where ε_χ is the fluorescence efficiency, Ω is the detector solid angle, E_f is the energy of the fluorescence photons, E denotes the incident X-ray beam energy, $\mu_\chi(E)$ is the absorption coefficient of the element of interest and $\mu_{\text{tot}}(E)$ is the total absorption coefficient (see Eq. (2.10)). Furthermore, the efficiency factor Φ has been introduced, accounting for the detector efficiency as well as intensity losses caused by absorption in the atmosphere and shielding foils in front of the detector.

The term $I_0(E) \exp(-\mu_{\text{tot}}(E)z_n/\alpha_n)$ describes the number of incident X-ray photons which made it to a depth z_n , while $\exp(-\mu_{\text{tot}}(E_f)z_n/(\alpha_n\beta_n))$ accounts for the attenuation of the fluorescence intensity that is generated in a depth z_n ⁴². The integration of Eq. (2.15) over the liquid jet delivers

$$I_f(E) \approx I_0(E) \frac{\Omega}{4\pi} \varepsilon_\chi \Phi \frac{\mu_\chi(E) \left[1 - e^{-(\mu_{\text{tot}}(E) + \mu_{\text{tot}}(E_f)/\beta)d'} \right]}{\mu_{\text{tot}}(E) + \mu_{\text{tot}}(E_f)/\beta}, \quad (2.16)$$

where $d' = d/\alpha$ denotes now the effective (uniform) sample thickness. Based on the literature²³ and the expression for the total fluorescence intensity, two important sample limits are considered in the following.

The *thin-sample limit*, which implies

$$(\mu_{\text{tot}}(E) + \mu_{\text{tot}}(E_f)/\beta) d' \ll 1. \quad (2.17)$$

Thereby, Eq. (2.16) can be rewritten as

$$I_f(E) \approx I_0(E) \frac{\Omega}{4\pi} \varepsilon_\chi \Phi \mu_\chi(E) d'. \quad (2.18)$$

The *dilute and thick-sample limit*, which implies

$$(\mu_{\text{tot}}(E) + \mu_{\text{tot}}(E_f)/\beta) d' \gg 1 \quad \text{and} \quad \mu_\chi \ll \mu_{\text{other}}. \quad (2.19)$$

^{ix}The expression is rephrased to the absorption of the element of interest.

^xThe reader is also referred to other literature⁴²⁻⁴⁴ for comparison.

^{xi}The effective optical paths are substituted in comparison to the literature^{31,42}. Furthermore, the efficiency factor Φ is introduced.

2. Theory of X-ray Absorption Fine Structure Spectroscopy

In this case Eq. (2.16) can be rewritten as

$$I_f(E) \approx I_0(E) \frac{\Omega}{4\pi} \varepsilon_\chi \Phi \frac{\mu_\chi(E)}{\mu_{\text{tot}}(E) + \mu_{\text{tot}}(E_f)/\beta}. \quad (2.20)$$

Furthermore, the energy dependence of the total absorption coefficient can be neglected

$$I_f(E) \propto I_0(E) \mu_\chi(E). \quad (2.21)$$

In both sample limits the measured fluorescence intensity is proportional to the absorption coefficient of the element of interest $\mu_\chi(E)$.

2.3. Time-Resolved Pump and Probe XAFS

This section presents the extension of the previous theoretical background of transmission and fluorescence yield detection of X-ray absorption spectroscopy to time-resolved pump and probe experiments. With the development of ultrafast lasersystems, X-ray absorption spectroscopy has been established as a powerful tool for photochemistry down to the picosecond time domain^{3,4}. In a pump-probe configuration, laser pulses excite the molecular system of interest at specific time delays with respect to the following probing X-ray pulses⁴⁵. X-ray absorption spectroscopy is used to take so-called *molecular snapshots* (at a fixed time delay) by measuring the X-ray absorption over the chosen energy range to study the laser induced changes⁴⁵.

Therefore, definitions of the transient transmission and fluorescence signals will be presented. Afterwards an approach to estimate the initial excitation yield of a molecular system for a given sample geometry is briefly introduced followed by a section presenting the statistical aspects of a time-resolved pump and probe experiment. This section is based on the literature³² and follows previous work in the field of time-resolved X-ray absorption spectroscopy^{6,33,34}.

2.3.1. Transient Transmission Signal

According to the literature^{10,32,34} the transmitted intensity $I_t(E)$ in a laser pump and X-ray probe configuration depends on the fraction of the excited species.

Therefore, the literature introduces the photoexcitation yield $f(t)$ to account for the fraction of sample molecules which reside in the excited state in the pump process at time delay t .

The transient transmission signal is by definition the difference between the (time-

resolved) pumped signal $I_t(E, t)$ and the (static) unpumped signal $I_t(E)$ ^{32,34xii}

$$S_t(E, t) = \ln \left(\frac{I_0(E)}{I_t(E, t)} \right) - \ln \left(\frac{I_0(E)}{I_t(E)} \right), \quad (2.22)$$

$$= \ln \left(\frac{I_t(E)}{I_t(E, t)} \right), \quad (2.23)$$

$$= f(t) \Delta \mu_\chi(E) d', \quad (2.24)$$

where $I_0(E)$ is the incident intensity, d' denotes the effective sample thickness and $\Delta \mu_\chi(E) = \mu_\chi^{ex}(E) - \mu_\chi^{gr}(E)$ is the difference in the absorption of the element of interest between the excited state and the ground state. The absorption coefficient can be expressed in terms of the absorption cross section by^{32,34}

$$\Delta \mu_\chi(E) = c \cdot N_A \cdot \Delta \sigma_{ex}(E) \quad (2.25)$$

$$\Delta \sigma_{ex}(E) = \sigma_{ex}(E) - \sigma_{gr}(E), \quad (2.26)$$

where c denotes the sample concentration, N_A is the Avogadro constant and $\Delta \sigma_{ex}(E)$ represents the difference between the absorption cross sections $\sigma_{ex}(E)$ and $\sigma_{gr}(E)$ of the element of interest in the excited state and the ground state, respectively. For a detailed description regarding the modification of the Lambert-Beer law the reader is referred to the literature, where the pump process is explained as a function of the sample concentration^{32,34}.

2.3.2. Transient Fluorescence Signal

Similar to the X-ray transmission mode the photoexcitation yield $f(t)$ is introduced to account for the temporal excited state fraction and the transient fluorescence signal $S_f(E, t)$ is defined in comparison to Eq. (2.14) as the difference between the (time-resolved) pumped signal $I_f(E, t)$ and the (static) unpumped signal $I_f(E)$ as follows³⁴:

$$S_f(E, t) = \frac{I_f(E, t) - I_f(E)}{I_0(E)}, \quad (2.27)$$

where $I_0(E)$ denotes the incident intensity. Based on the literature^{32,34}, both sample limits introduced in Eq. (2.18) and Eq. (2.20) are considered in the following.

The transient signal for the thin-sample limit can be introduced as

$$S_f(E, t) = \frac{\Omega}{4\pi} f(t) \varepsilon_\chi \Phi \Delta \mu_\chi(E) d', \quad (2.28)$$

where Ω denotes the detector solid angle, ε_χ represents the fluorescence efficiency and Φ accounts for the detector efficiency as well as fluorescence intensity losses caused by absorption in the atmosphere or in shielding foils. Furthermore, $\Delta \mu_\chi$ refers to the difference in the absorption of the element of interest between excited state and ground state and d' is the effective sample thickness.

^{xii}The literature^{32,34} describes the pump process in terms of the absorption cross section as a function of the sample concentration. With regard to Sec. 2.2, the expressions are rewritten in terms of the absorption coefficient as a function of the time delay t .

2. Theory of X-ray Absorption Fine Structure Spectroscopy

According to Eq. (2.21), the transient signal of the dilute and thick sample is simply proportional to the difference in the absorption coefficient.

$$S_f(E, t) \propto f(t) \Delta\mu_\chi(E) \quad (2.29)$$

In both sample limits the transient fluorescence signal is proportional to the transient transmission signal.

2.3.3. Estimation of the Initial Excitation Yield

The initial excitation yield is governed by the ratio of the number of absorbed laser photons N_{ph}^{Abs} and the number of sample molecules^{4,6xiii}:

$$f(0) = \frac{q \cdot N_{Abs}^{ph}}{c N_A V_{ex}}, \quad (2.30)$$

where q denotes the quantum efficiency of the photoexcited state, c is the sample concentration, N_A is the Avogadro constant and V_{ex} represents the illuminated volume.

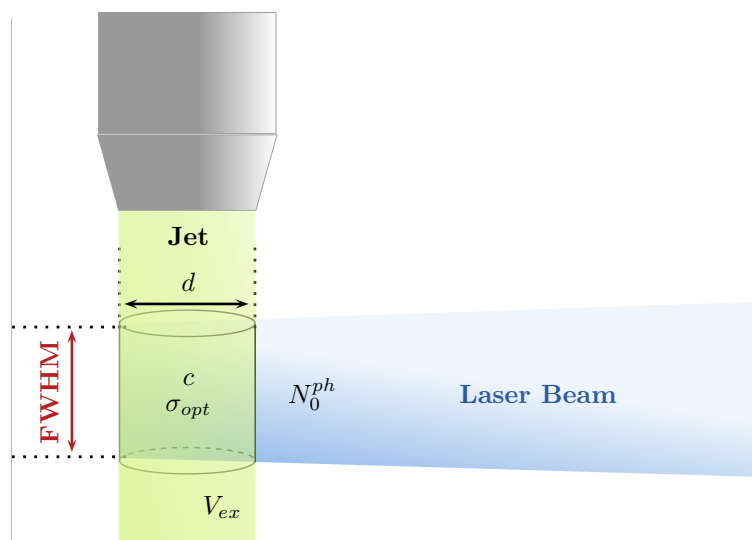


Figure 2.8.: Illustration of the photoexcitation process within the present sample geometry. The cylindrical volume V_{ex} , which is defined by the laser focus size (FWHM) and the liquid jet diameter d , is illuminated by a number of laser photons N_0^{ph} . The excitation process further depends on the concentration of sample molecules c and the optical cross section σ_{opt} for a given wavelength⁶. The figure is adapted from reference⁶.

^{xiii}Based on reference⁶ while the implementation of the quantum efficiency q was inspired by the literature⁴.

The number of absorbed laser photons can then be obtained via the Lambert-Beer law^{6xiv}

$$N_{\text{Abs}}^{\text{ph}} = N_0^{\text{ph}} \left(1 - e^{-cN_A(1-f(0))\sigma_{\text{opt}}d} \right), \quad (2.31)$$

where N_0^{ph} denotes the number of incident laser photons, d is the sample thickness and σ_{opt} represents the optical cross section of the sample molecules for a given wavelength. Inserting Eq. (2.31) into Eq. (2.30) leads to

$$f(0) = \frac{q \cdot N_0^{\text{ph}}}{cN_A V_{\text{ex}}} \left(1 - e^{-cN_A(1-f(0))\sigma_{\text{opt}}d} \right), \quad (2.32)$$

which is similar to the expression given in the literature³². The complete process with variables is shown in Fig. 2.8. Additionally, the laser beam profile has to be approximated by a gaussian profile and the varying sample thickness has to be considered, thus Eq. (2.32) can only be solved numerically.

2.3.4. Statistical Aspects

Assuming a full photoexcitation yield ($f = 1$) possible changes in the X-ray absorption cross section relative to the absorption edge-jump are up to 100% in the XANES region, while in the fine-structure region the photoinduced X-ray absorption cross section modulations are relatively weak with $< 10\%$ ³².

Typically, the changes in the X-ray absorption cross section decrease with increasing energy, making detectable signals after the first fine-structure (EXAFS) modulation a real experimental challenge.

Therefore, experiments within the pump and probe configuration strongly depend on their achievable *signal-to-noise ratios* (S/N). On the one hand, high signal-to-noise ratios can be obtained by driving the photoexcitation yield to very high values with the restriction not to risk the generation of other photoproducts or nonlinear effects, since the S/N ratio increases exactly linear with $f(t)$ for a given sample concentration^{32,34xv}. On the other hand, the transient signals can be measured for a very large number of laser and X-ray shots m which is - depending on the repetition rate of the data acquisition - a time-consuming factor since the S/N ratio increases with \sqrt{m} .^{32,34} Supposing that noise contributions only originate from the inherent shot noise of the X-ray pulses one obtains the expressions³⁴

$$N_t(E, t) = \sqrt{\frac{1}{I_t(E, t)} + \frac{1}{I_t(E)}}, \quad (2.33)$$

$$N_f(E, t) = \frac{\sqrt{I_f(E, t) + I_f(E)}}{I_0(E)}, \quad (2.34)$$

for the respective detection mode. Thereby, the static expressions represent the unpumped signals while the pumped signals account for the photoexcitation process at time delay t .

^{xiv}The Lambert-Beer law was modified in a previous work⁶ and accounts only for the ground state molecules in the photoexcitation process.

^{xv}The reference³⁴ describes the aiming for a nonlinear excitation process.

2. *Theory of X-ray Absorption Fine Structure Spectroscopy*

3. The Transition Metal Complex

fac-Ir(ppy)₃

3.1. Ground State Structure	19
3.2. Molecular Orbital Diagram and Electronic Structure . . .	20
3.3. UV/VIS Absorption and Emission Spectroscopy	23
3.4. Photocycle of the Metal-to-Ligand Charge Transfer	24

This chapter introduces the fac-Tris[2-phenylpyridinato-C²,N]iridium(III) complex, usually denoted as fac-Ir(ppy)₃ or simply Ir(ppy)₃. This complex was chosen with regard to its anticipated strong photoinduced charge transfer reaction to demonstrate that the developed XAFS setup is suitable for charge transfer detection. This chapter follows the typical description of a transition metal complex shown in previous work^{33,34}.

3.1. Ground State Structure

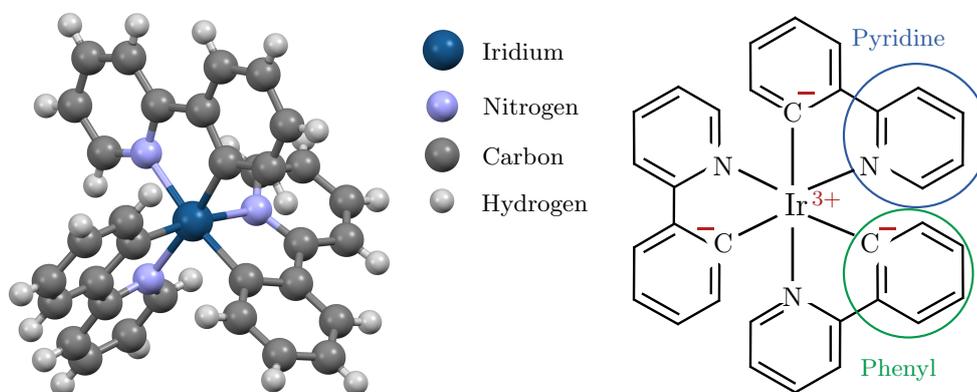


Figure 3.1.: Illustrated structure of fac-Ir(ppy)₃ (reproduced from reference¹⁸). Right figure is based on reference⁴⁶.

The ground state structure of fac-Ir(ppy)₃ is reported in reference¹⁸ and was characterized by X-ray crystallography. In this transition metal complex three 2-phenylpyridine anions (ppy⁻) are attached to the central iridium ion, which is coordinated by one nitrogen and one carbon atom per ligand¹⁸. The complex exhibits a strong dipole moment with an ionic valence state of the metal atom (III) while each ligand exhibits a single negative valency (see Fig. 3.1)¹⁸. The site symmetry of the molecule

3. The Transition Metal Complex *fac-Ir(ppy)*₃

is reported as C₃, thus depicting a slightly distorted octahedral symmetry^{17,18,98}. This results in a symmetry-averaged bond length of the first coordination shell (Ir-N and Ir-C) of 2.063 Å¹⁸.

The complex was purchased from Sigma-Aldrich Co. in Germany⁴⁷.

3.2. Molecular Orbital Diagram and Electronic Structure

The molecular orbital diagram and electronic structure are commonly described by the crystal field theory and more complex by the ligand field theory^{5,48}.

Since the octahedral symmetry (*O_h*) is typically well documented in the literature^{5,48} and reference¹³ actually characterizes Ir(ppy)₃ as *quasi-octahedral*, the following description illustrates the molecular orbital structure of this complex on the basis of an octahedral environment. In case of transition metal complexes the focus is on the metal d-orbitals.

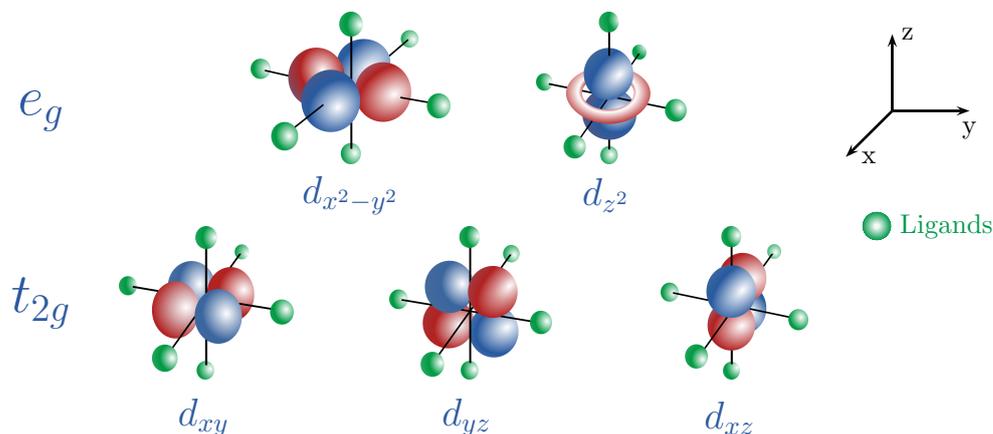


Figure 3.2.: Illustrated metal d-orbital geometry in an octahedral complex. The orbitals *d_{xy}*, *d_{yz}* and *d_{xz}* form the *t_{2g}* set and their lobes are oriented in space between the coordinate axes, while the lobes of the orbitals in the *e_g* set (*d_{x²-y²}* and *d_{z²}*) are oriented exactly along the coordinate axes⁵. The ligands are indicated as green clouds. The figure is based on the literature⁴⁹.

The d-orbital geometry is shown in Fig. 3.2, where the lobes of three orbitals *d_{xy}*, *d_{yz}* and *d_{xz}* are oriented in space between the coordinate axes, while the lobes of the orbitals *d_{x²-y²}* and *d_{z²}* are oriented exactly along the coordinate axes⁵. As described in Sec. 3.1, three 2-phenyl pyridine anions are attached to the central iridium ion forming a ML₆ configuration. The σ -bonding between metal and ligands occurs along the coordinate axes (see Fig. 3.2).

Therefore, to participate in the interaction of bonding, the lobes of the metal orbitals need to point along the coordinate axes⁴⁸ⁱ. As a consequence the metal d-orbitals are

ⁱThe description follows now in great detail reference⁴⁸.

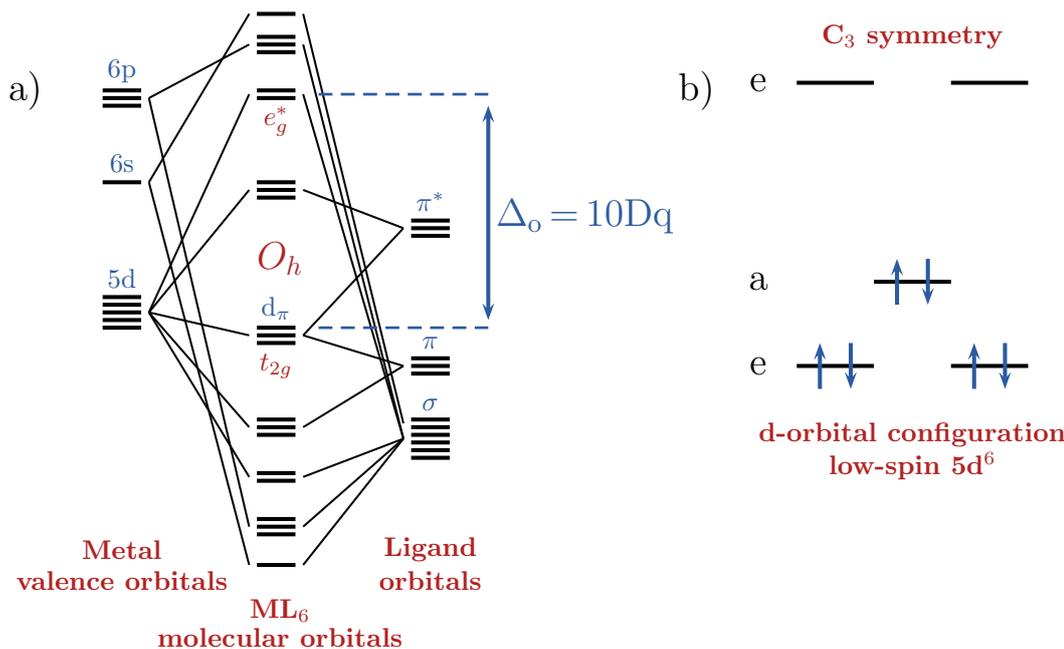


Figure 3.3.: **a)** Molecular orbital diagram of an octahedral complex with π back-bonding in which the metal d-orbitals are split into t_{2g} and e_g sets. The figure is based on the literature^{33,48}. **b)** In C_3 symmetry the t_{2g} set further splits into a non-degenerate a and a doubly degenerate e set of orbitals,. Furthermore, the metal valence electron configuration is shown¹³.

split into a threefold-degenerate (t_{2g}) and a twofold-degenerate (e_g) set of orbitals⁴⁸. In more detail, the orbitals of the t_{2g} set are not involved in the formation of bonds and become nonbonding orbitals (d_π)⁴⁸.

Bonding is then achieved by hybridization of one s, three p and two d orbitals (e_g) of the metal atom creating identical d^2sp^3 hybrids in which each orbital can accept two electrons⁴⁸. These six bonding orbitals interact or mix with six lone pair orbitals on the ligands to create six σ -bonding and six σ -antibonding orbitals⁴⁸. The bonding orbitals are stabilized in energy (lowered) with respect to their parent orbitals, while the other antibonding orbitals are destabilized with respect to their parents and are therefore of higher energy⁴⁸. In conclusion, this leads to an energy splitting of the metal d-orbitals where the electron energies of the nonbonding orbitals (t_{2g}) are not affected⁴⁸.

Typically a flow of electron density from metal d_π to empty π^* orbitals located on the ligands takes place²¹, which is referred to as π back-bonding⁴⁸. Including the concept of π back-bonding into the molecular orbital diagram leads to a fall (stabilization) of the t_{2g} set and thus increases the splitting of the metal d-orbitals⁴⁸. Hence, the flow of electron density stabilizes the metal-ligand bonding⁴⁸.

The splitting of the metal d-orbitals is referred to as the (*octahedral*) *crystal field splitting* $10Dq$ and is attributed to characterize the metal-ligand interaction⁵⁰ⁱⁱ:

ⁱⁱThe notation of the crystal field splitting parameter varies from literature to literature. In the framework of this thesis the notation $10Dq$ is used. Furthermore, the metal-ligand interaction based on the crystal field theory is nicely summarized in reference⁵⁰. For this reason, the description follows

3. The Transition Metal Complex *fac-Ir(ppy)*₃

- The ordering of the ligands based on their potential to induce crystal field splittings 10Dq is characterized by the *spectrochemical series*^{13,50}. The ppy ligands are attributed to induce a strong crystal field splitting 10Dq (see App. F)¹³.
- Larger crystal field splittings 10Dq imply a shorter metal-ligand bonding⁵⁰. More specifically, the crystal field splitting *"is inversely proportional to the fifth power of bond length."*⁵⁰
- The crystal field splitting 10Dq increases with the oxidation state of the central metal atom (M)⁵⁰.

$$M(\text{II}) \ll M(\text{III}) < M(\text{IV})$$

10Dq increases →

- Considering a complex with the same ligands, the crystal field splitting 10Dq is referred to increase by 30-40 % when the central metal ion of the first row of transition metals in the Periodic Table is exchanged by a metal ion of the second row¹³. The field splitting increases similarly when a second-row metal ion is exchanged by a third-row metal ion¹³.

The molecular orbital diagram of the ground state is shown in Fig. 3.3, in which the superscript (*) denotes antibonding orbitals while the subscript *g* represents the parity (gerade) of the inversion operation.

In C₃ symmetry the *t*_{2g} set further splits into a doubly degenerate *e* and a non-degenerate *a* representation (see Fig. 3.3b)¹³. In case of Ir(ppy)₃ the strong crystal field splitting leads to a low-spin 5d⁶ configuration where the *t*_{2g} set is completely filled with electrons¹³.

now the aforementioned reference and refers to the literature¹³ to provide further information.

3.3. UV/VIS Absorption and Emission Spectroscopy

The measured UV/VIS absorption spectrum of the Ir(ppy)₃ complex dissolved in dimethyl sulfoxide is shown in Fig. 3.4. The following description and information is mainly taken from the literature^{15,16}.

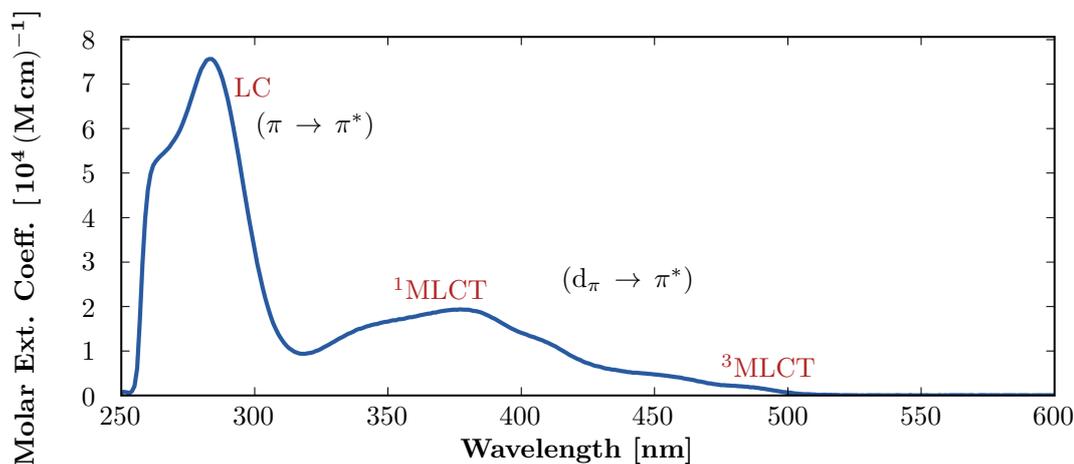


Figure 3.4.: Measured UV/VIS absorption spectrum of the Ir(ppy)₃ complex dissolved in dimethyl sulfoxide at room-temperature. The absorption bands are classified as ligand-centered (LC) or metal-to-ligand charge transfer (MLCT) transitions according to the literature^{15,16}.

First of all, it is characterized by an intense absorption band occurring in the UV part of the spectrum between 260 and 320 nm, which is assigned to spin-allowed ligand-centered transitions (LC) ($\pi \rightarrow \pi^*$)¹⁶.

In addition, there is a broad absorption band centered around 380 nm, which is extending to the visible region up to around 500 nm and corresponds to allowed as well as spin-forbidden metal-to-ligand charge transfer states (MLCT)¹⁶. The first part up to 390 nm of the MLCT band is classified as the spin-allowed ($d_\pi \rightarrow \pi^*$) metal-to-ligand charge transfer band (¹MLCT)^{15,16}. Further bands at longer wavelengths, which are identified by peaks around 410 and 460 as well as 480 nm, involve formally spin-forbidden ³MLCT transitions^{15,16}. However, these assignments are referred to as guidelines in the literature due to the spin-orbit coupling¹⁵.

In the present work the metal-to-ligand charge transfer band is excited with ultra-short pulses at a wavelength of 343 nm. The corresponding excited state dynamics will be introduced in the following section. The photoluminescence spectrum at room-temperature was measured with a concentration of 1 mM Ir(ppy)₃ dissolved in dimethyl sulfoxide. The emission spectrum is illustrated in Fig. 3.5 and shows broad emission wavelengths centered around 535 nm. At lower concentrations we observed a shift of a few nanometers to shorter wavelength (≈ 3 nm).

3. The Transition Metal Complex $\text{fac-Ir}(\text{ppy})_3$

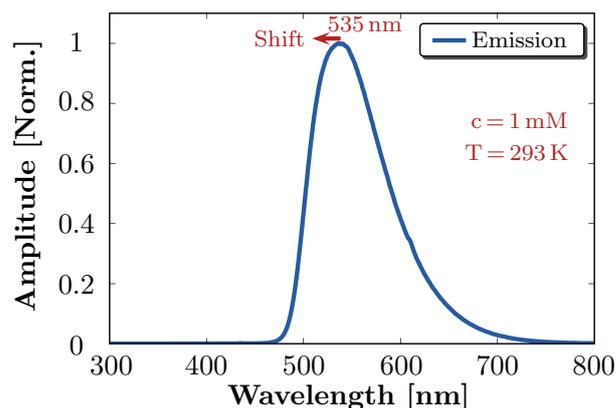


Figure 3.5.: Measured UV/VIS emission spectrum of the $\text{Ir}(\text{ppy})_3$ complex dissolved in dimethyl sulfoxide (1 mM) at room-temperature.

3.4. Photocycle of the Metal-to-Ligand Charge Transfer

The photocycle of $\text{Ir}(\text{ppy})_3$ depicting the metal-to-ligand charge transfer is illustrated in Fig. 3.6. The following description is based on and summarizes the literature^{19–21}. After photoexcitation of the metal-to-ligand-charge transfer band the excited electron density, mainly located on a metal valence orbital (5d), is transferred to π^* orbitals located on the ppy ligands, leading to the formation of the singlet $^1\text{MLCT}$ state²⁰.

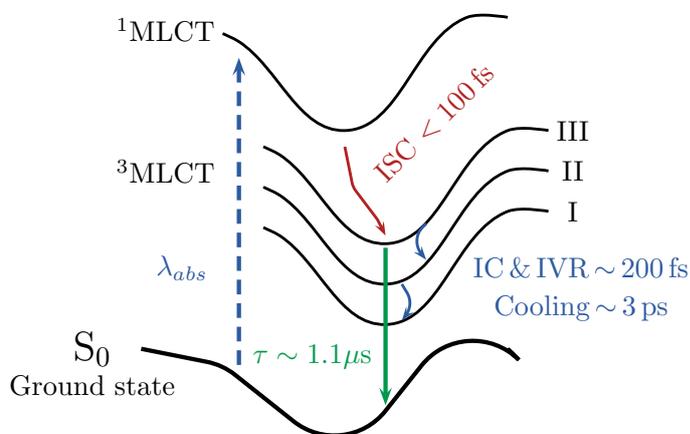
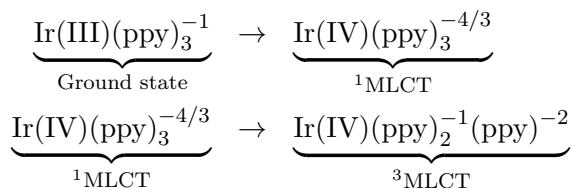


Figure 3.6.: Illustrated photocycle of $\text{Ir}(\text{ppy})_3$ describing the excited state dynamics. Following the photoexcitation the electron density, mainly located on a metal valence orbital (5d), is transferred to π^* orbitals located on the ppy ligands forming the $^1\text{MLCT}$ state²⁰. A fast intersystem crossing ($\text{ISC} < 100 \text{ fs}$) leads to the formation of the triplet state $^3\text{MLCT}$ ²⁰. The triplet state decays to the ground state by emission of visible light²⁰. Figure is adapted from reference²⁰.

Due to the strong spin-orbit interaction a mixing of singlet and triplet states is favored and therefore the $^1\text{MLCT}$ state subsequently crosses within $\leq 100 \text{ fs}$ to the triplet state

3.4. Photocycle of the Metal-to-Ligand Charge Transfer

$^3\text{MLCT}$ ²⁰. In an ionic approximation the photocycle can be described asⁱⁱⁱ:



The excited system initially populates the substate level III (see Fig. 3.6)^{iv} and further relaxes to the lower two substate levels via internal conversion (IC)²⁰. Thereby, the excited electron density localizes on one ppy ligand, especially on the pyridine moiety, and the molecular symmetry changes from C_3 to C_1 ²¹. The excited state then decays to the ground state \mathcal{S}_0 by phosphorescence²⁰. The visible emission mainly originates from substate level III, which is itself fed by thermal populations from the other substate levels (II, I)²⁰. Substate level III exhibits a decay time of several hundreds of nanoseconds while substate II and I have decay times of a few microseconds and about hundred microseconds, respectively^{13,19,20}.

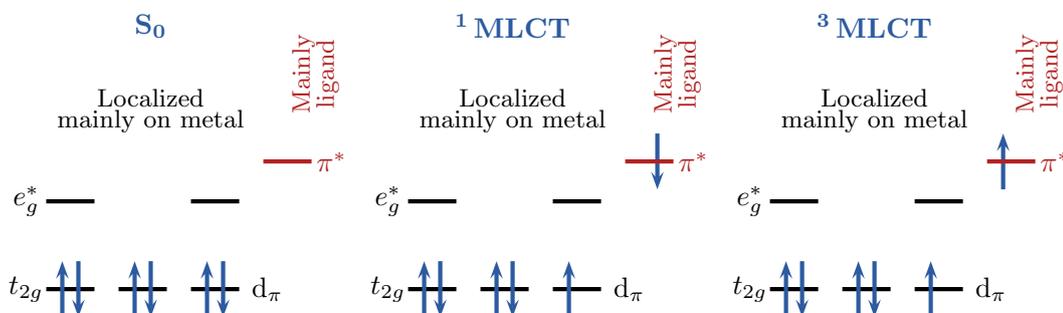


Figure 3.7.: Illustrated metal valence orbital configuration of Ir(ppy)₃ in an ionic approximation. Inspired by the literature^{22,51}.

In particular, the transitions between the substate levels II or III and the ground state are significantly allowed, while the remaining transition between the substate level I and the ground state is relatively weak or forbidden¹⁹. In this example the resulting decay time of a degassed solution of Ir(ppy)₃ in toluene is reported as $\sim 1.1 \mu\text{s}$ ²⁰.

Further theoretical investigations describe the triplet state mainly as a mixture between LC and MLCT states due to the strong spin-orbit coupling²¹. To complete the description of the photocycle the electronic configuration of the metal valence orbitals for the ground state \mathcal{S}_0 and the excited states $^1\text{MLCT}$ and $^3\text{MLCT}$ is shown in Fig. 3.7.

ⁱⁱⁱ Compare to the similar photocycle of Ru(bpy)₃ shown in reference⁹.

^{iv} According to the literature²¹, the lowest excited states exhibit mainly triplet character.

3. The Transition Metal Complex $fac\text{-Ir}(ppy)_3$

4. Experimental Infrastructure

4.1. Synchrotron Radiation X-ray Source PETRA III	27
4.1.1. Working Principle of a Synchrotron Radiation Source	27
4.1.2. Important Synchrotron Quantities	29
4.2. Beamline P11 at PETRA III	31
4.2.1. Undulator Radiation	31
4.2.2. Double Crystal Monochromator	33
4.2.3. High-End Focusing KB Mirror System	34
4.2.4. Experimental Hutch	35

This chapter describes the experimental infrastructure, in particular beamline P11, which is part of the PETRA III synchrotron radiation source at DESY in Hamburg, Germany^{52,53}. In the following sections, a brief overview about the general working principle of a synchrotron is provided and beamline P11 is described in more detail.

4.1. Synchrotron Radiation X-ray Source PETRA III

PETRA III (Positron-Electron-Tandem-Ring-Accelerator) is a third generation synchrotron radiation source located in Hamburg (Germany) as part of the *Deutsches Elektronen Synchrotron* (DESY). It is the third reincarnation of the PETRA storage ring, which was foremost used as electron-positron collider in the 1980s and afterwards utilized to support the lepton-proton collider HERA as pre-accelerator⁵².

The storage ring was rebuilt in 2007 to the most brilliant synchrotron source worldwide providing the first synchrotron radiation for photon science experiments since 2010⁵². Up to now, fourteen different beamlines offer their experiments to the worldwide community⁵².

4.1.1. Working Principle of a Synchrotron Radiation Source

The following description of a synchrotron radiation source is based on and summarizes the literature⁵⁴ if not stated otherwise. A schematic drawing of the operation principle and key elements of a synchrotron is shown in Fig. 4.1. Thereby, electrons are typically produced by a thermionic (electron) gun and afterwards pre-accelerated by an *injector* consisting of a linear accelerator (LINAC) and a booster (storage) ring to the desired kinetic energy (\sim GeV) before they are extracted into the core element,

4. Experimental Infrastructure

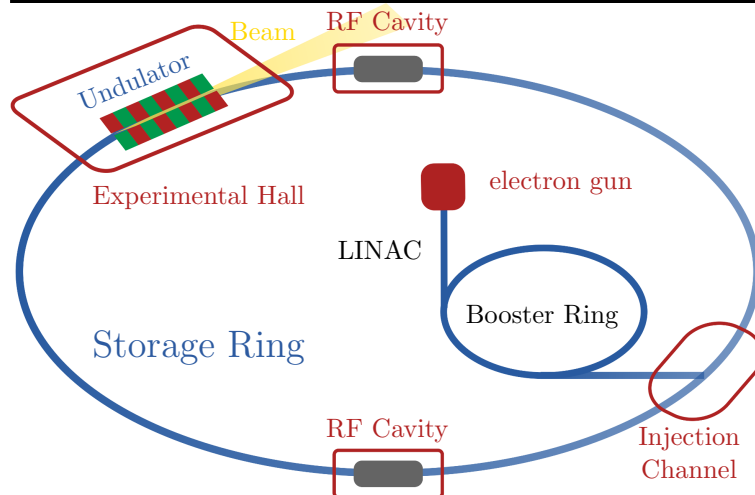


Figure 4.1.: Operation principle of a synchrotron radiation source with electron gun, LINAC, storage (booster) ring, RF cavities, storage ring and undulators to generate synchrotron radiation. The figure is based on reference⁵³.

the *storage ring*ⁱ. Here they orbit under ultrahigh vacuum conditions for many hours forced on a closed trajectory by *bending magnets* via the Lorentz forceⁱⁱ. *Insertion devices*, so-called *undulators*, are located on several straight sections, forcing the electrons to oscillate and generate synchrotron radiation. The emitted radiation is finally delivered to the beamlines and experimental endstations.

In a synchrotron or storage ring the circulating electrons are emitting electromagnetic radiation, called synchrotron radiation. However, after emission the energy of the electrons has to be corrected, else they would rapidly lose energy and cannot circulate in the storage ring. This issue is solved by installed *radiofrequency cavities* (RF), where the electrons are accelerated by the electric field whenever they pass the cavity, thus increasing their kinetic energy. This concept is even refined in a way that only electrons which have lost a certain amount of energy are accelerated, while the other electrons pass without any further action.

The application of RF cavities implies that synchrotron radiation sources are synchronized and pulsed light sources. Thereby, the pulse spaces are separated by distances defined by the pulsed electric field of the cavities. Commonly the pulse spaces are referred to as *buckets* and called *bunches* if they are further filled with electrons⁵³. The time period for a complete turn of a bucket (revolution time) is defined by the ratio of the circumference of the storage ring and the speed of light (\sim electron speed). The inverse of the time period defines the characteristic revolution frequency of the synchrotron. In order to provide a constant ring current electrons are periodically injected to the weakest bunches, which is referred to as *top-up* mode⁵³ⁱⁱⁱ. An overview

ⁱThe description is also based on the technical design report of PETRA III. According to the technical design report of PETRA III, the electron gun provides electrons with an energy of 150 keV. The electrons are then pre-accelerated up to a kinetic energy of 450 MeV at the LINAC and afterwards boosted up to an energy of \sim 6 GeV at the DESY II storage ring.

ⁱⁱThe ultrahigh vacuum is essential to reduce the electron loss due to their collisions with residual atoms.

ⁱⁱⁱCompare also to reference⁵⁴.

about the most important parameters of PETRA III is given in Tab. 4.1^{iv}. In the following the RF signal and the revolution frequency are abbreviated as 500 MHz and 130 kHz, respectively.

Table 4.1.: Specifications of the synchrotron radiation source PETRA III⁵⁵.

Parameter	Magnitude
Energy	6.08 GeV
Circumference	2304 m
RF signal	499.564 MHz
Revolution Time	7.685 μ s
Revolution Frequency	130.1 kHz
Number of buckets	3840
Number of bunches	40 # – 960 #
Bucket separation	2 ns
Bunch separation	192 ns (40 #) - 8 ns (960 #)
Bunch length	44 ps (rms)
Beam current	100 mA
Operation	Top-up mode (\sim 1 %)

4.1.2. Important Synchrotron Quantities

In general, the quality of synchrotron radiation is characterized by the *brilliance*, which is by definition proportional to the number of emitted photons per second F and inversely proportional to the total photon source sizes in horizontal σ_{T_h} and vertical σ_{T_v} direction and the related total divergence $\sigma_{T'_h}$ and $\sigma_{T'_v}$, respectively, for a given bandwidth^{53,54v}:

$$B = \frac{F}{4\pi^2 \cdot \sigma_{T_h} \cdot \sigma_{T_v} \cdot \sigma_{T'_h} \cdot \sigma_{T'_v} \cdot 0.1 \% \text{ Bandwidth}}. \quad (4.1)$$

Thereby, the number of emitted photons per second is commonly referred to as *photon flux*⁵⁴.

$$[F] = \frac{[\textit{photons}]}{[s]} \quad (4.2)$$

Furthermore, the total source sizes and divergences are provided in a Gaussian approximation with their rms values and are further characterized by the convolution of the electron beamsizes (σ_h , σ_v) and divergences ($\sigma_{h'}$, $\sigma_{v'}$) with the intrinsic radiation characteristics (σ_r , $\sigma_{r'}$) related to a single electron⁵³:

$$\sigma_{T_h} = \sqrt{\sigma_h^2 + \sigma_r^2}, \quad (4.3)$$

$$\sigma_{T'_h} = \sqrt{\sigma_{h'}^2 + \sigma_{r'}^2}. \quad (4.4)$$

^{iv}The energy is corrected.

^vThe reference⁵³ uses the description of a spectral photon flux. In the framework of this thesis the common photon flux is used according to reference⁵⁴.

4. Experimental Infrastructure

Following the literature⁵³, the horizontal emittance, which is referred to be of *crucial importance* for X-ray beam parameters, is described by

$$\varepsilon_h = \sigma_h \cdot \sigma_{h'}. \quad (4.5)$$

The vertical emittance can then be derived by⁵³

$$\varepsilon_v = \kappa \cdot \varepsilon_h, \quad (4.6)$$

where κ is the so-called *coupling factor*. The quality parameters, establishing PETRA III as one of the most brilliant synchrotron world-wide, are shown in Tab. 4.2.

Table 4.2.: Quality parameters of the synchrotron radiation source PETRA III⁵⁵.

Parameter	Magnitude
Horizontal Emittance ε_h	1 nmrad (rms)
Vertical Emittance ε_v	0.01 nmrad (rms)
Coupling κ	1 %

4.2. Beamline P11 at PETRA III

Beamline P11 at PETRA III is dedicated to imaging, diffraction and - of special in-house interest - time-resolved pump and probe experiments⁵⁶. Since all experiments within this framework have been conducted at beamline P11, the basic elements are explained in further detail. The optical layout of beamline P11 is shown in Fig. 4.2 where the main elements are highlighted in blue color.

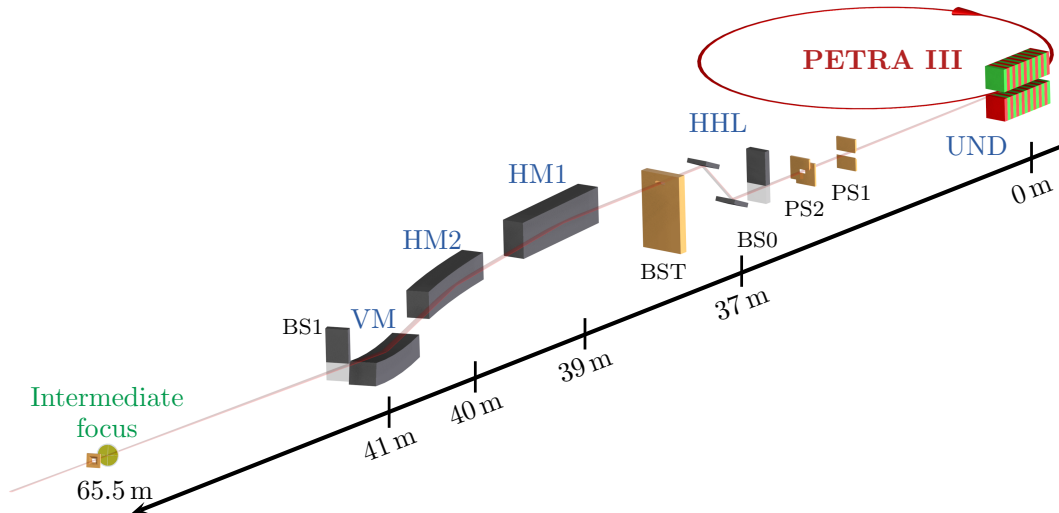


Figure 4.2.: Schematic view of the optical layout of beamline P11. UND: Undulator, PS: Power slit, BS: Beam shutter, HHL: High-heat load monochromator, BST: Beam stop; HM: Horizontal Mirror, VM: Vertical mirror. [By Courtesy of T. Pakendorf]

At first the theoretical background of the insertion device is briefly introduced. Afterwards, the monochromator (HHL) is described with a focus on the geometry of the two crystals inside the monochromator chamber followed by an explanation of the high-end focusing mirror system. At the end of this section an overview of the experimental end-station is given.

4.2.1. Undulator Radiation

The following description of an undulator is based on and summarizes the literature⁵⁴ if not stated otherwise.

Insertion devices are key elements of third generation synchrotrons to generate electromagnetic radiation. A schematic illustration of an undulator is depicted in Fig. 4.3. It consists of a periodic array of magnets, which force the electrons to oscillate (undulate) around the straight line of propagation. Thereby, the amplitudes of the oscillations

4. Experimental Infrastructure

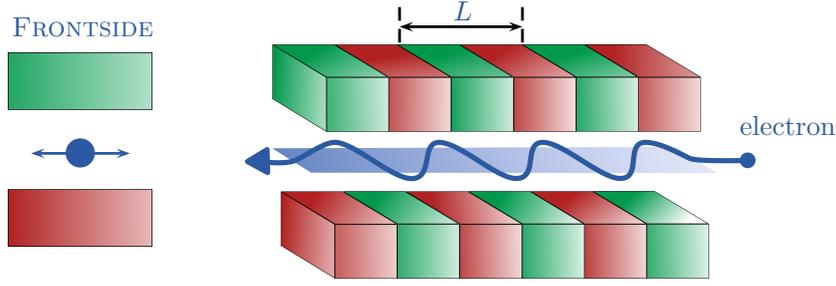


Figure 4.3.: Schematic explanation of an undulator source. The figure adapted from reference⁵⁴.

are on a scale set by the inverse of the relativistic factor⁵⁷

$$\gamma = \frac{1}{\sqrt{1 - \frac{v_e^2}{c^2}}}, \quad (4.7)$$

where v_e is the electron velocity and c denotes the speed of light. In contrast to other insertion devices the magnet period length L of an undulator is designed in a way that, related to a given electron, the emitted radiation from all oscillations are in phase with each other⁵⁷. Thereby, the period L is shrunk by the Lorentz contraction to L/γ . This also applies for the straightforwardly emitted wavelength λ_L which gets additionally Doppler-shifted by a factor $\approx 1/(2\gamma)$, thus leading to

$$\lambda_L \approx \frac{L}{2\gamma^2}. \quad (4.8)$$

The resulting electromagnetic radiation is horizontally polarized and forms a cone with an opening angle of $1/(\gamma\sqrt{N})$, where N is the number of undulator periods⁵⁷. The parameter characterizing an insertion device is defined as

$$K = 0.934 \cdot L[\text{cm}] \cdot B[\text{T}], \quad (4.9)$$

where B denotes the amplitude of the applied magnetic field^{vi}. Finally, a transverse correction of the electron velocity as well as an angular correction is applied to the emitted wavelength in Eq. (4.8), yielding^{vii}

$$\lambda_L \approx \frac{L}{2\gamma^2} \cdot \left(1 + \frac{K}{2} + \gamma^2\theta^2\right), \quad (4.10)$$

where θ represents the takeoff-axis angle. Furthermore, Eq. (4.9) implies that the emitted wavelength can be controlled by adjusting the magnetic field strength B and therefore K . This can be achieved by either increasing or decreasing the gap size between the periodic magnet arrays.

The emitted fundamental wavelength is further accompanied by its related higher harmonics (λ_L/n), while only odd harmonics ($n = 1, 3, 5, \dots$) are discovered for small

^{vi}The K -parameter of an undulator is ~ 1 ⁵⁷.

^{vii}The formula has been corrected.

deviations from the forward direction ($\theta \rightarrow 0$). The relative bandwidth of the emitted harmonic wavelength is given by

$$\frac{\Delta\lambda_L}{\lambda_L} = \frac{1}{Nn}. \quad (4.11)$$

The parameters of the U32 undulator installed at beamline P11 are shown in Tab. 4.3.

Table 4.3.: U32 undulator parameters at beamline P11⁵⁸.

Parameter	Magnitude
Total length	2 m
Periods	63
Period length L	31.4 mm
Polarization	Horizontal

4.2.2. Double Crystal Monochromator

The monochromator installed at beamline P11 is the standard PETRA III high-heat load (HHL) double crystal monochromator. The monochromator is operated in Bragg geometry⁶¹ with a fixed exit beam and can be utilized either with a pair of Si(111) or Si(311) crystals to extract an X-ray energy E from the synchrotron beam⁵⁸. Both crystal pairs are mounted on the same Bragg axis, which is driven by a servo motor in a closed loop ensuring high precision. In addition, all crystals are cooled with liquid nitrogen.

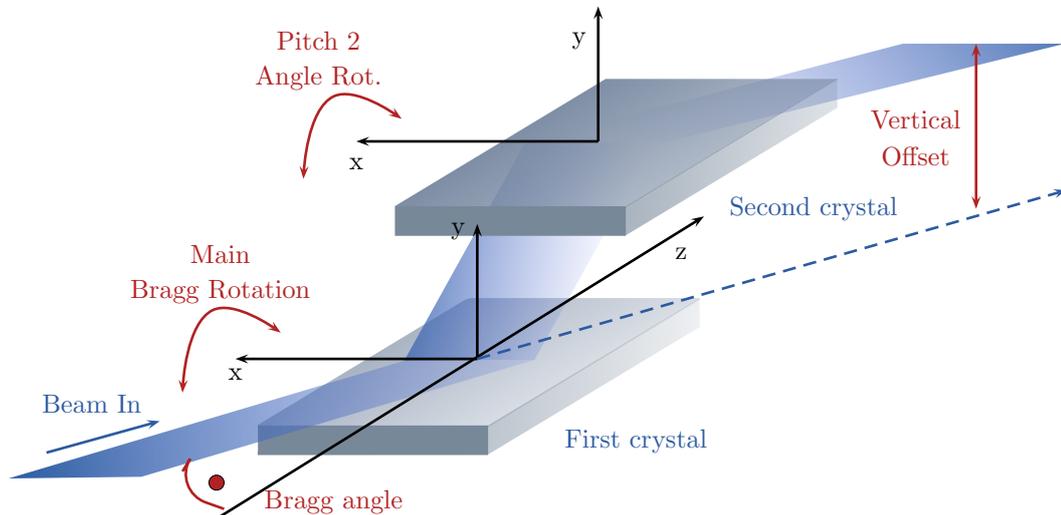


Figure 4.4.: Sketch of the silicon crystal geometry inside the monochromator chamber with fixed vertical offset and indication of the pitch 2 angle. The figure is based on reference⁶².

4. Experimental Infrastructure

The geometry of the two crystals inside the monochromator is illustrated in Fig. 4.4. The illustrated *pitch 2 angle* allows to correct the vertical beam position and is utilized for an active feedback control of the X-ray beam. According to the beam-line specifications⁵⁸, the monochromator provides X-ray photon energies between 2.4 and 30 keV. At 12 keV the feasible energy resolution for the Si(111) crystal corresponds to $\Delta E/E = 1.3 \cdot 10^{-4}$, while the Si(311) crystal provides a bandwidth of $\Delta E/E = 0.28 \cdot 10^{-4}$. The maximum flux at an energy of 12 keV is $\sim 2.0 \cdot 10^{13}$ photons per second⁶⁰.

4.2.3. High-End Focusing KB Mirror System

The following description of the mirror system is based on and summarizes the literature⁶⁰ if not stated otherwise. Beamline P11 shares its straight section with beamline P12, which makes it necessary to separate the beam paths in order to obtain a sufficient spacing between the experiments. Therefore, the mirror system at beamline P11 has been designed to consist of two horizontal deflecting mirrors for beam separation and one vertical deflecting mirror, creating a so-called *Kirkpatrick-Baez*⁵⁹ (*KB*) *Mirror System*. The mirror surfaces are of high optical quality in order to preserve the coherence properties of the X-ray beam⁵⁶.

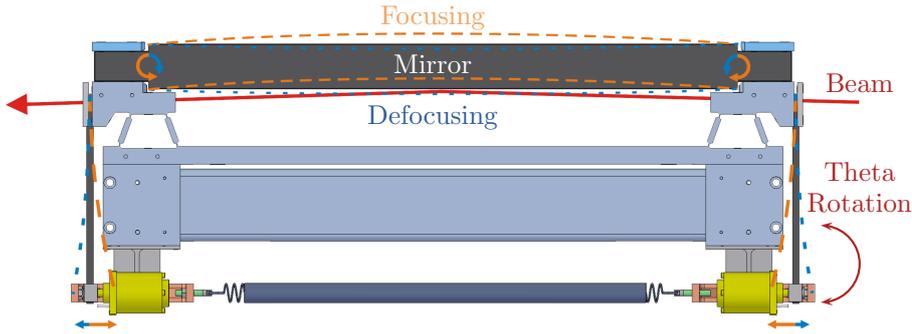


Figure 4.5.: Bending principle of the second horizontal mirror (top view). The mirror features three different coatings and is located on a rotation stage. [By Courtesy of T. Pakendorf]

Regarding Fig. 4.2, the mirror system is located at a source distance of roughly 40 m behind the double crystal monochromator. All three mirrors are mounted on a solid granite support starting with the horizontal mirrors. Every mirror is dynamically bendable and features three different coatings, uncoated silicon, palladium and platinum for the respective wavelengths⁵⁸. Moreover, concave and convex bending operations are possible, in order to generate different beam sizes at the experiment. The bending principle of the second horizontal mirror is shown in Fig. 4.5. The mirror is held by two flexure based stages at both ends to maintain the pivot point in the center. The bending mechanism is driven by two linear actuators with a resolution of 50 nm. Both horizontal deflectors can achieve a radius of curvature between -12 km and 10 km while the vertical deflector has a feasible radius of curvature ranging from -100 km to 10 km, leading to minimum X-ray beam sizes of $(43 \times 363) \mu\text{m}$ (FWHM) ($v \times h$) at 68.5 m

distance from the source. The horizontal mirrors are placed on a flexure based rotation stage driven by piezo actuators. The rotation angle of the second horizontal mirror is of special interest since it is utilized for feedback control of the horizontal X-ray beam position.

4.2.4. Experimental Hutch

Key element of the experimental hutch is an 8 meter long granite block with a weight of 10 tons, ensuring high vibrational stability⁵⁶. A basic scheme of the hutch is shown in Fig 4.6.

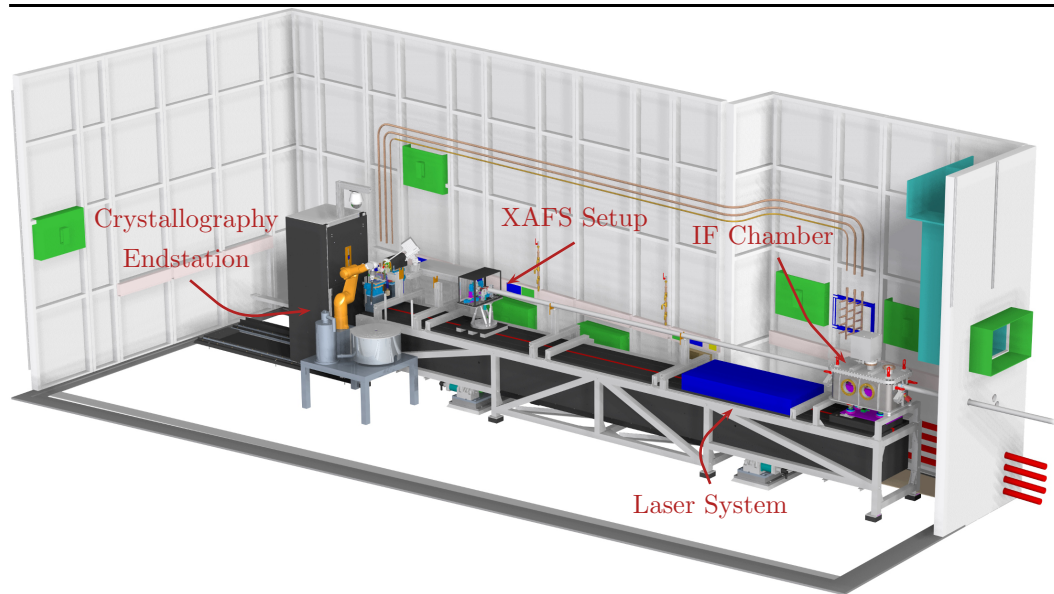


Figure 4.6.: Inside view of the beamline endstation P11. [By Courtesy of N. Stuebe]

A station for crystallographic data collection is located at the end of the granite, whereas the in-house developed setup for time-resolved X-ray absorption studies is placed on a hexapod shortly before. At the beginning of the granite the so-called *intermediate focus chamber* is located, directly followed by the ultra-short pulse laser system.

The intermediate focus chamber houses beamline essentials such as adjustable absorbers, slit systems and beam position monitors (see Sec. 6.5). The setup derives from the idea to generate focus at 65 m distance from the source inside the chamber allowing beam manipulation and treating the intermediate focus chamber as secondary source (see Fig. 4.2).

An additional KB mirror system will allow further reduction of the spot size by imaging the secondary source onto the crystallography endstation down to sizes of a few micrometers. The experiments described in this thesis were carried out using the first KB system only.

4. *Experimental Infrastructure*

5. Experimental XAFS Setup

5.1. Setup Overview	38
5.2. Ultrashort Pulse Lasersystem	39
5.3. Micro-Jet System	40
5.4. On-Axis Microscope	41
5.5. Beam defining Pinhole	42
5.6. Detectors	43
5.6.1. Photon Flux Measurements - Silicon Photodiode	43
5.6.2. X-ray Fluorescence Measurements - Avalanche Photodiode	44
5.7. Data Acquisition Scheme	47
5.7.1. Gating Structures for Bunch Selection	48
5.8. Principle of Spatial and Temporal Overlap	49
5.9. Optimization of the Avalanche Photodiode Signal	51

This chapter presents the developed setup for time-resolved pump and probe X-ray absorption spectroscopy experiments. The first setup was built up together with Benjamin Dicke⁶ and Moritz Schlie⁷. The experiment was subsequently improved together with Philip Roedig. The focus of this work was in particular on the following aspects:

- Implementation and commissioning of the data acquisition and the timing device bunchclock.
- Redesign of the on-axis microscope.
- Redesign of the complete setup to perform experiments in helium atmosphere.
- The establishment of a feedback mechanism for X-ray beam position control (see Sec. 6.5.1).
- Shielding development to reduce the amount of elastically scattered photons in the measured fluorescence intensity.
- User-friendly design to perform a rapid adjustment of the temporal overlap between X-ray and laser pulse with a single motorized fast photodiode.
- The laser system, laser synchronization and laser safety commissioning as well as their full implementation into the beamline software.

5. Experimental XAFS Setup

- The software development for automatic and user-friendly control of the experiment and beamline essentials, which accumulated in more than sixty thousand lines of python code.

Similar descriptions of the setup can therefore be also found in previous work.

5.1. Setup Overview

The XAFS setup for time-resolved measurements is placed on top of a six-axle kinematic positioning system (hexapod), which is located on the granite block before the crystallography endstation in the P11 experimental hutch. A schematic sketch of the setup illustrating both the UV/VIS and X-ray path is shown in Fig. 5.1. The X-ray

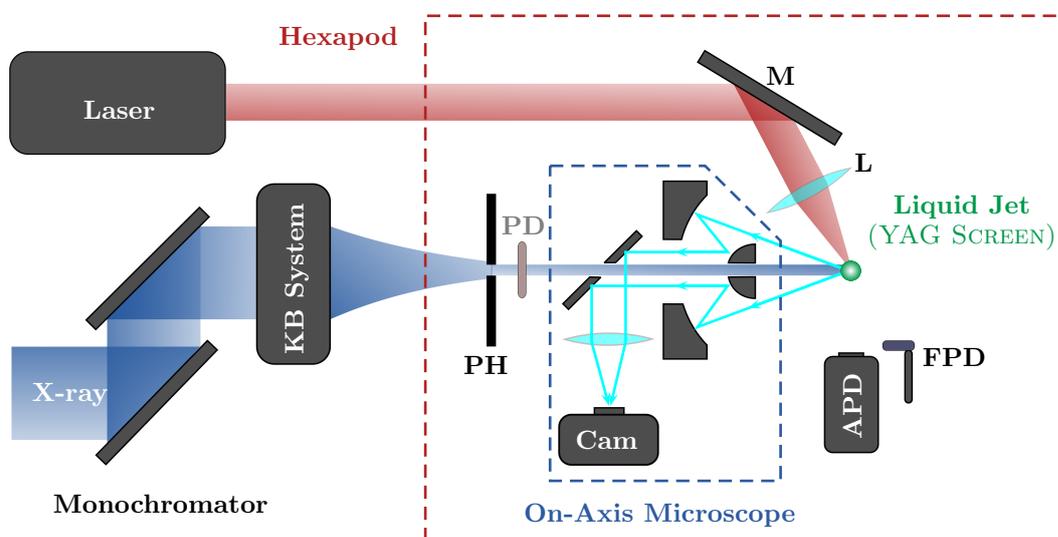


Figure 5.1.: Simplified optical layout of the experimental XAFS Setup. KB: Kirkpatrick-Baez system, PH: Pinhole, PD: Photodiode, Cam: CCD camera, APD: Avalanche photodiode, FPD: Fast photodiode, M: Mirror, L: Lens. Figure is based on reference⁶⁶.

beam coming from the undulator is passing through the double crystal monochromator for energy selection and is afterwards focused with a dynamically bendable KB mirror system. At the experiment the beam is further shaped by a pinhole, defining the X-ray spot size. The beam then passes through a silicon photodiode for I_0 measurements and finally through a small hole in the on-axis microscope before interacting with the sample. The sample is delivered by a liquid jet system, which is mounted onto a three-axle translational motor tower. An avalanche photodiode (APD) is placed on an identical three-axle positioning system at an angle of 90 degrees with respect to the incident beam direction to collect the X-ray fluorescence from the sample.

The pump laser beam is guided to the sample by a set of mirrors and focused by a lens shortly before the sample.

For a better understanding the most important parts of the setup are described in the following sections.

5.2. Ultrashort Pulse Lasersystem

A femtosecond laser system from *Light Conversion* was installed at beamline P11 in the framework of this thesis. It consists of the pump laser *PHAROS*, the harmonic generator *HIRO* and the optical parametric amplifier *ORPHEUS* with its dedicated harmonic generator *LYRA*. With a footprint of $\sim 1 \text{ m}^2$ the whole system fits perfectly onto the solid granite support in the experimental hutch, as shown in Fig. 5.2. Based on their technical manual and website, the laser system is further introduced in the following^{63,64}. The magnitudes are also taken from the service report⁶⁵.

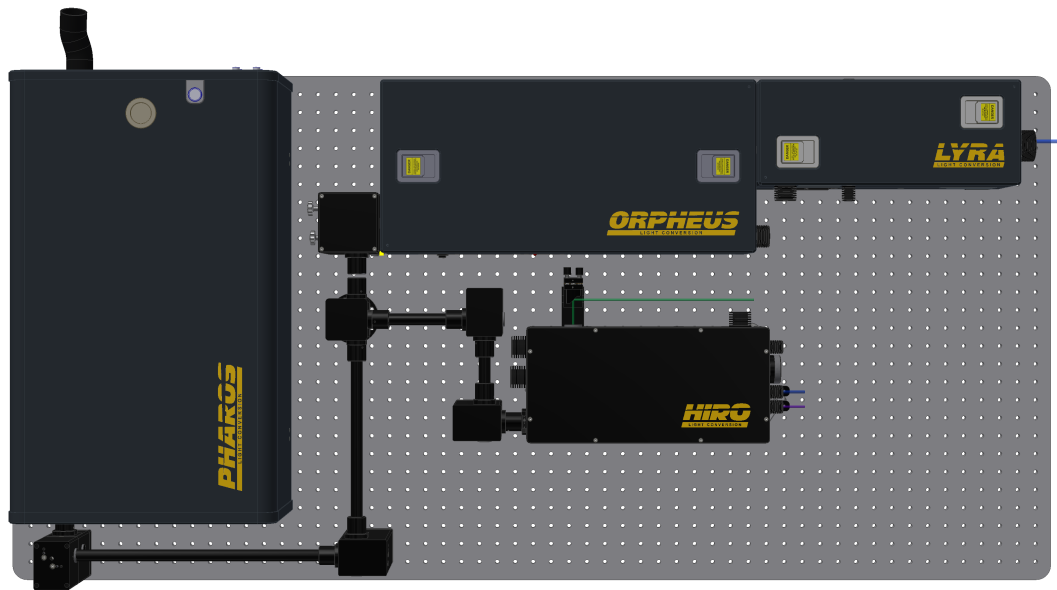


Figure 5.2.: Setup of the ultrashort pulse laser system at the beamline P11. The setup consists of the pump laser *PHAROS* and three passive modules, the harmonic generator *HIRO* as well as the optical parametric amplifier *ORPHEUS* with its dedicated harmonic generator *LYRA*. [Courtesy of Light Conversion]

The pump laser is a single-unit integrated femtosecond laser system based on the CPA¹ technique combining a seed oscillator working with Kerr-lens modelocking, regenerative amplifier and a single stretcher/compressor unit⁶³. Both oscillator and regenerative amplifier are based on Yb:KGW as lasing medium, thus leading to a fundamental wavelength of 1030 nm, and are pumped by active solid-state laser diodes⁶³. Typically a BBO pockels cell triggers amplifier operation, while another Pockels cell is located directly before the beam exit and acts as *pulse picker*⁶³. The repetition rate of the laser pulses can be varied between single shot operation and 300 kHz utilizing both Pockels cells. Typical pulse energies are limited to 1 mJ at frequencies up to 5 kHz and are further decreasing at higher repetition rates. The overall maximum output power is given with 6 W and the pulse durations after the compressor are in the range of 180 fs - 10 ps.

¹CPA stands for Chirped-Pulse Amplification and is briefly described in reference⁶⁷.

5. Experimental XAFS Setup

Additional passive modules make this system a real workhorse for spectroscopic experiments. On the one hand, the harmonic generator HIRO is designed to provide second-harmonic (SH), third-harmonic (TH) and fourth-harmonic (FH) generation at high repetition rates, e.g. 65 kHz and 130 kHz. On the other hand, the optical parametric amplifier ORPHEUS is designed to perform best at repetition rates between 5 kHz and 10 kHz. The application of these modules strongly depends on the experimental requirements. For liquid samples including a fast sample exchange as applied in the

Table 5.1.: Typical conversion efficiencies with output pulse energies obtained with the harmonic generator HIRO installed at beamline P11.

Conversion	Efficiency	Pulse Energy [65 kHz]	Pulse Energy [130 kHz]
SH (515 nm)	55%	50 μ J	25 μ J
TH (343 nm)	30%	28 μ J	14 μ J
FH (257 nm)	10%	9 μ J	5 μ J

XAFS setup, the HIRO is utilized in order to benefit from the higher repetition rates allowing a faster data acquisition. The typical conversion efficiencies and pulse energies at different repetition rates for the higher harmonics are listed in Tab. 5.1. The optical parametric amplifier ORPHEUS in combination with the harmonic generator LYRA allows to freely select a wavelength between 260 nm and 2600 nm at different pulse energies ranging from $\approx 10 \mu$ J in deep UV to $\approx 100 \mu$ J into the infrared photon energy regime. This combination is ideally suited for experiments with solid-state samples where the amount of induced thermal energy should be kept at a minimum.

5.3. Micro-Jet System

For XAFS experiments in this thesis the sample was delivered by a liquid jet system. The micro-jet setup was developed by B. Dicke as part of his PhD thesis⁶. It is a circular flow system based on swagelok components consisting of a sample reservoir, a fluidic pump, a glass nozzle and a sample catcher. A laminar jet is hereby created by pressing the sample solution from the reservoir through the glass nozzle⁶. Afterwards, the sample solution is collected by the catcher and lead back to the reservoir, creating a closed cycle. Typical lengths of the nozzles are 50 mm, while the inner diameter can be selected between 15 μ m and 300 μ m⁶. A sketch of the jet mount including glass nozzle is shown in Fig. 5.3. The glass nozzle is clamped by a plastic ferrule into a swagelok adapter, which is in turn screwed to a particle filter. The micro-filter is needed to avoid blockage of the nozzle due to coagulation of the sample solution. A tool holder is attached to the nozzle mount, holding a cerium doped YAG crystal to visualize both the laser and X-ray beam. Additionally, a sharp silicon edge is mounted close to the nozzle to perform edge scans in order to determine X-ray and pump laser beam sizes.

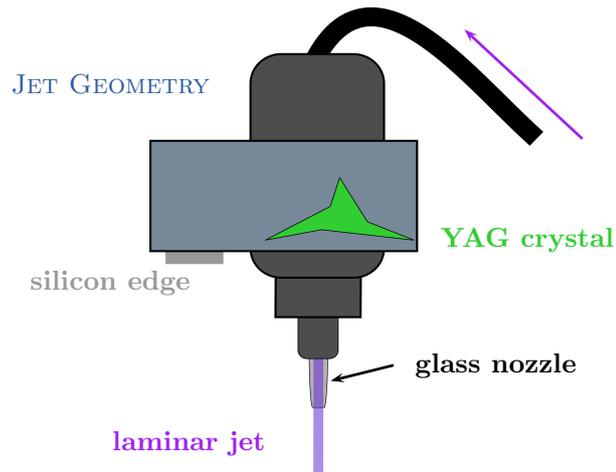


Figure 5.3.: Sketch of the liquid jet holder with different tools attached. A scintillator screen is mounted directly above the jet nozzle and can be moved into the focal plane of the on-axis microscope to visualize the X-ray and laser beam. A sharp silicon edge is placed close to the nozzle to perform edge scans.

5.4. On-Axis Microscope

The on-axis microscope (OAM) is an essential part of the setup. The corresponding schematic drawing is shown in Fig. 5.4. The OAM concept is based on three optical elements, a reflective microscope objective (RMO) with a drill hole of 1.5 mm in the center of the secondary mirror, a mirror with a drill hole of 2 mm in the center and a tube lens. The drill holes allow the X-ray beam to pass without any absorption losses

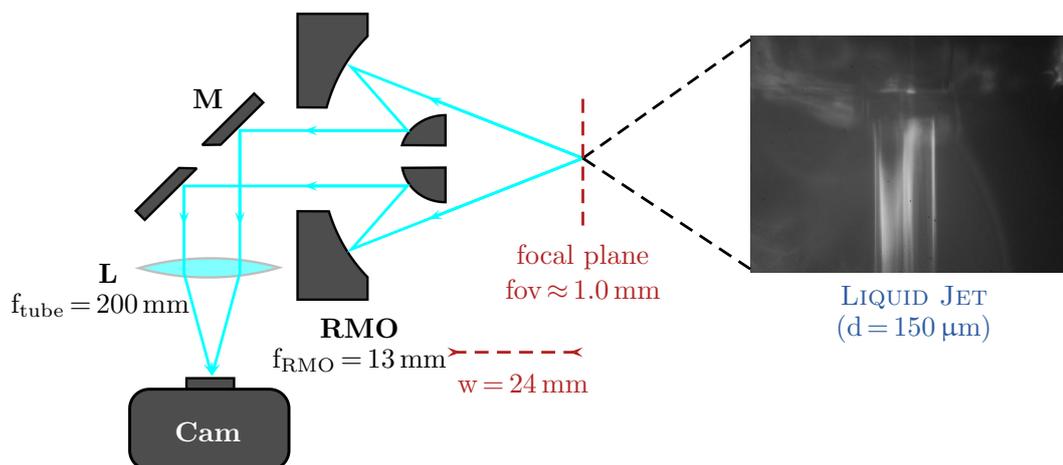


Figure 5.4.: Detailed sketch of the on-axis microscope (OAM) used in the XAFS experiment (see Fig. 5.1). RMO: Reflective microscope objective, M: Mirror, L: Lens, w: Working distance, f: Focal length, fov: Field of view, Cam: CCD camera.

5. Experimental XAFS Setup

to the sample. This geometry also serves as an excellent shielding of air scattering from the intense X-ray beam, while the contrast of the image is only slightly affected by the drill holes. The light coming from the focal plane (≈ 1 mm field of view) is collimated by the reflective microscope objective and passing through the tube lens and further imaged onto a CCD camera. The total magnification is given by the ratio of the two focal lengths.

$$M = \frac{f_{\text{tube}}}{f_{\text{RMO}}} \approx 15.38$$

The objects are visualized depending on the sensor quality of the used CCD Camera. Here a camera with $7.4 \mu\text{m}$ pixel-size and 1600×1200 pixels is installed. The reproduction scale is roughly $0.5 \mu\text{m}$ per pixel.

5.5. Beam defining Pinhole

Pinholes to define the X-ray beam size were mainly required due to beam position fluctuations caused by the monochromator of the beamline. Within a pump and probe experiment a well-defined sample volume has to be illuminated by the X-ray beam with ideally no intensity fluctuations. Since the monochromator vibrations cause beam position shifts of several tens of micrometer especially in the vertical plane, the focusing capabilities of the KB system could not be fully explored. In order to obtain a stable illumination of the sample without significant intensity variations only a vertically semi-focused X-ray beam was used to over-illuminate a pinhole. By selecting only the central part of the beam a relatively stable X-ray beam could be obtained at the cost of photon flux.

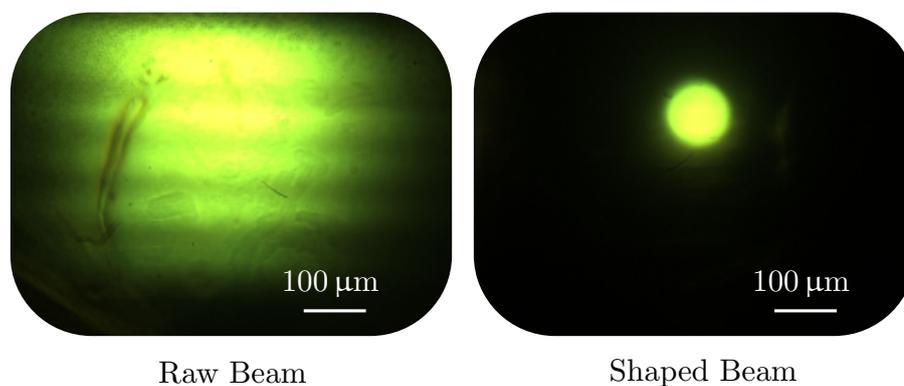


Figure 5.5.: Typical shaping process with platinum pinholes to define the spot size. **Left:** Raw X-ray beam visualized with the OAM. **Right:** Final beam size defined by a $100 \mu\text{m}$ pinhole.

The pinhole diameter is typically chosen to match the liquid jet size ($50 \mu\text{m} - 300 \mu\text{m}$). Additionally, these pinholes lead to a higher experimental stability, because they avoid the non-excited sample volume to be probed by the X-ray beam. The pinholes used in this setup are made of platinum and commonly used in electron microscopy. A typical

beam shaping process is illustrated in Fig. 5.5, where on the left the raw X-ray beam is visualized with the on-axis microscope using the YAG screen as scintillator. The pinhole can be moved by an inhouse developed piezo motor to the desired position, defining the final beam size and position.

5.6. Detectors

The detectors used in the experiments were a silicon photodiode operating in transmission geometry for flux measurements and an avalanche photodiode (APD) for X-ray fluorescence detection.

5.6.1. Photon Flux Measurements - Silicon Photodiode

The silicon photodiode used for flux measurements has an active area of $10 \times 10 \text{ mm}^2$ and is used to monitor intensity changes of the X-ray beam and to normalize the fluorescence data with respect to the incident photon flux at a certain X-ray energy. The photodiode has a thickness of $10 \mu\text{m}$ and can therefore be used in transmission geometry at energies $> 5 \text{ keV}$ with relatively small absorption losses only. For noise reduction the diode is shielded with a $25 \mu\text{m}$ thick black capton foil. Technical parameters are provided in Fig. 5.6.

Parameter	Magnitude
Layer	Silicon
Thickness	$10 \mu\text{m}$
Diode Area	$10 \times 10 \text{ mm}^2$
max. Current	2 mA
Operation	Transmission
Capton Shield	$25 \mu\text{m}$

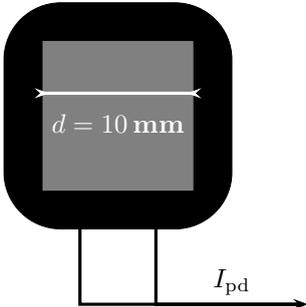


Figure 5.6.: Detailed parameters silicon photodiode used for flux measurements. Magnitudes are based on the datasheet from Hamamatsu (Cat. No. KPIN107E01, Jul. 2006). The flux can be calculated according to the literature⁶⁸.

According to the literature⁶⁸, a simple model based on energy deposition in silicon can be utilized to determine the incident X-ray photon flux using a silicon photodiode. The following description is based on and summarizes the literature⁶⁸.

Upon X-ray radiation electron-hole pairs are created in the depletion layer, while $\epsilon = 3.66 \text{ eV}$ are needed for one pair, thus depositing energy and inducing the photocurrent I_{pd} . This photocurrent can be further used to count back to the X-ray photon flux Φ . The transmitted photon flux is expressed by

$$\Phi_{\text{Trans}} = \Phi \exp(-At_{\text{si}}\rho_{\text{si}}), \quad (5.1)$$

5. Experimental XAFS Setup

where Φ is the incident photon flux, A the cross section of the active layer, t_{si} the thickness of the diode and ρ_{si} the density of silicon. With the assumption of a linear diode response and by using the relationship $I_{\text{pd}} = \Phi Q$, where Q is the charge created upon X-ray radiation, the photoconversion ratio can be expressed as

$$\frac{\Phi}{I_{\text{pd}}} = \frac{\epsilon}{eE [1 - \exp(-A_{\text{pe}} t_{\text{si}} \rho_{\text{si}})]}. \quad (5.2)$$

Here A_{pe} represents the photoelectric cross-section of silicon at a given energy, e the elementary charge and ϵ is the amount of energy needed to create an electron-hole pair. This relationship is used throughout this thesis to calculate the incident photon flux.

5.6.2. X-ray Fluorescence Measurements - Avalanche Photodiode

The detector system used for fluorescence detection consists of an avalanche photodiode (APD) head and an electronic pulse processing controller^{71,72}. The APD head is based on the *reach-through* principle and exhibits a $5 \times 5 \text{ mm}^2$ silicon layer of $110 \mu\text{m}$ thickness with a multi-stage amplifier^{71,72}. Similar to pin diodes electron-hole pairs are created in an APD in the depletion layer upon X-ray radiation, but the electrons are now in contrast to them accelerated by electric fields towards the *avalanche region*⁷³. Thereby, their kinetic energy reaches an extent that collisions⁷⁴ with the crystal lattice produce additional electron-hole pairs, which is commonly referred to as *avalanche process*⁷³ resulting in signals amplified by factors of 200 and more⁷². The electric field is created by a reverse bias originating from the pulse processing unit⁷². The most important features are summarized in Fig. 5.8. In the following, the electronic signal circuit will be explained (see Fig. 5.7) based on their technical manuals^{71,72}. The

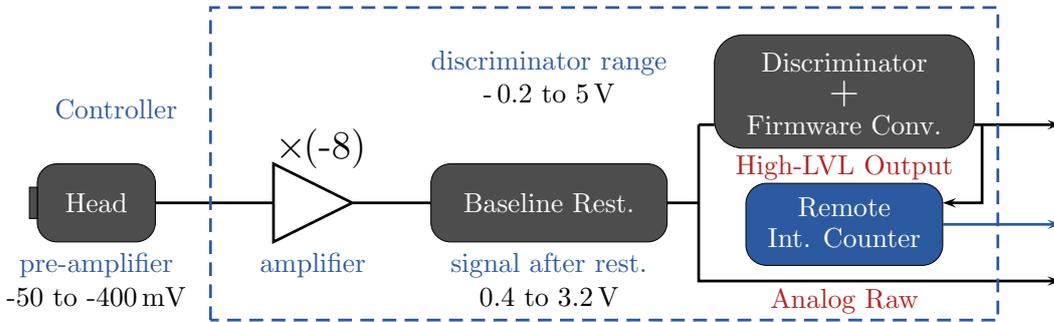


Figure 5.7.: Electronic circuit of the avalanche photodiode signal⁷¹.

deposited energy inside the depletion layer of the APD head is converted by a pre-amplifier into a voltage between -50 and -400 mV⁷¹. By entering the pulse processing unit the signal is further inverted and amplified by a factor of 8 and enters the baseline restoration circuit. Afterwards, the voltage signal is transformed to the discriminator range of -0.2 to 5 V for further signal processing⁷¹. Both signals, the raw voltage signal and the high-level output from the discriminator, can be used for data acquisition. The discriminator output is of essential importance and therefore explained in detail.

Within the discriminator a low-level and a high-level threshold as well as the operation

mode can be set⁷¹. In *integral mode* an output pulse is generated every time the signal reaches the low-level threshold, while in the *window mode* every signal level between both thresholds triggers an output pulse⁷¹. The discriminator exhibits an internal counter⁷¹ which was made remotely accessible through the TANGO systemⁱⁱ.

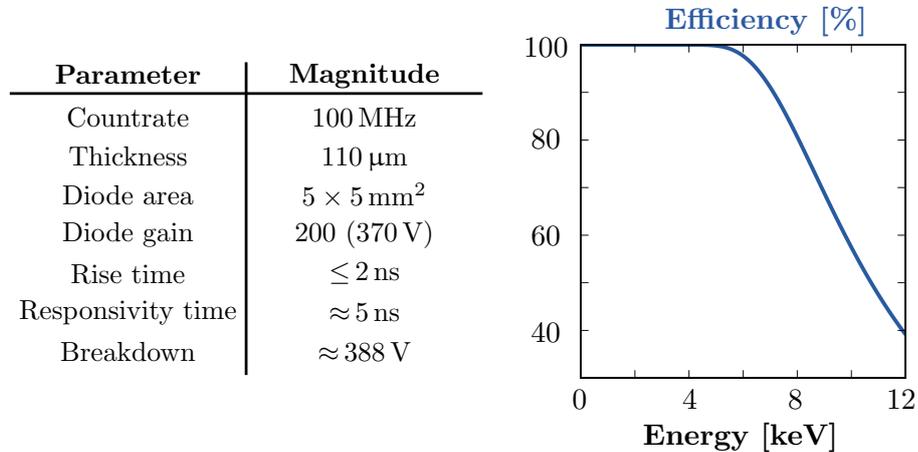


Figure 5.8.: Detailed parameters of the APD head used in the experimental setup^{71,72}. The efficiency has been calculated using a similar approach as described in the literature⁶⁸.

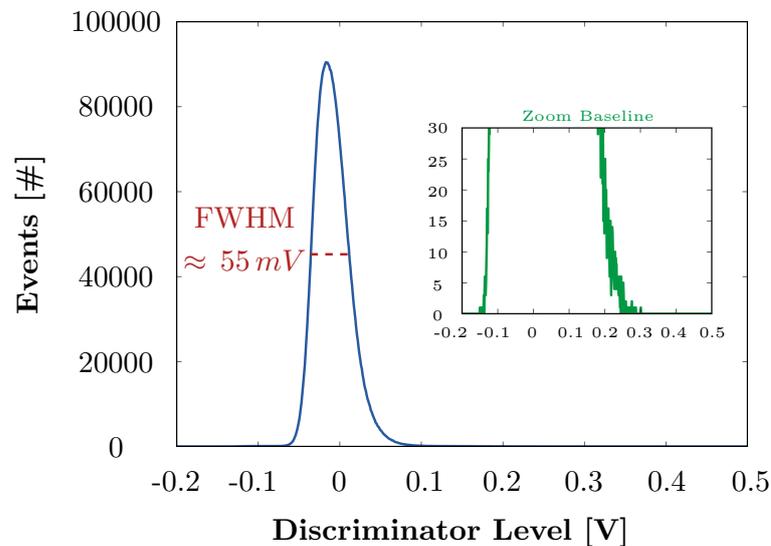


Figure 5.9.: Measured noise of the pre-amplifier located in the avalanche photodiode head. Band-pass window: 1 mV, Step size: 1 mV, Integration time: 1 ms. X-rays: OFF.

Both operation modes are needed in order to perform the experiment. The integral mode is used for general X-ray fluorescence detection, while the window mode is used

ⁱⁱTANGO is the standard control system used at PETRA III. For a detailed description the reader is referred to the web page⁸⁹.

5. Experimental XAFS Setup

for calibration and verification of the low-level threshold set in integral mode. For this purpose, the pre-amplifier noise inside APD head at 300 V bias is characterized without X-ray beam by scanning a small window of 1 mV with 1 ms acquisition time per level throughout the beginning of the discriminator range reading the internal counter. The outcome is depicted in Fig. 5.9 and shows a Gaussian distribution centered around 0 V with a width of 55 mV (FWHM). Therefore, in order to avoid pulses in the experimental data triggered by pre-amplifier noise, the low level threshold has to be set ≥ 0.25 V. Secondly, a typical discriminator scan is shown, this time with a scanning window of 10 mV and 1 ms acquisition time per level in order to characterize the photon statistics with X-ray beam exposure on the sample. The outcome is shown

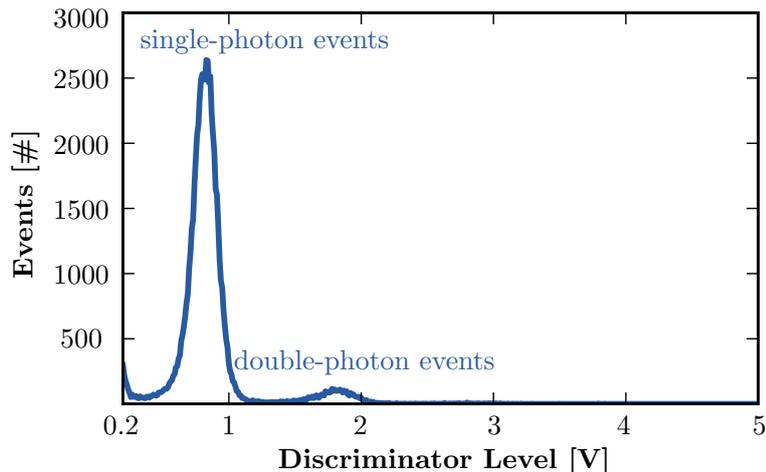


Figure 5.10.: Measured discriminator spectrum (stopped after 4 V), in which two features can be identified. The first peak represents single-photon events, while the second one corresponds to two-photon events. No further multi-photon events are detected, thus the so-called *single photon counting* (SPC) regime is almost fulfilled. Band-pass window: 10 mV; Step size: 10 mV; Integration time: 1 ms. X-rays: ON.

in Fig. 5.10, where two features can be identified. The first peak represents single photon events, while the second one represents the first multi-photon event. This occurs if two X-ray fluorescence photons deposit their energy within the responsivity time, doubling the voltage signal. The experiment has to be performed in the so-called *single photon counting* (SPC) regime since the data acquisition electronics can not handle multi-photon events for now. Therefore, the probability for multi-photon events has to be kept small. This is almost fulfilled since the multi-photon intensity is very small compared to the single-photon intensity.

5.7. Data Acquisition Scheme

The block diagram of the data acquisition scheme is illustrated in Fig. 5.11 showing two main circuits. One shows the signal flow for obtaining the X-ray fluorescence data, the other one shows the signal flow for I_0 measurements.

The fluorescence photons deposit energy inside the APD head, triggering high level output pulses from the discriminator of the pulse processing unit as described in Sec. 5.6.2. These pulses are fed into *Constant Fraction Discriminators* (CFD)⁷⁰, which are gated by reference signals originating from the RF cavity. The basic working principle of a CFD is not of interest, they are only used for filtering the fluorescence signal in order to obtain the so called *pumped* and *unpumped* signals from the gated bunches. The gating of the X-ray fluorescence signal is mandatory since the repetition rate of the laser system does not match the repetition rate of the synchrotron. The corresponding gating structure is described in Sec. 5.7.1 in greater detail. The filtered high level pulses are further registered by a multi-channel scaler (MCS), counting the gated events separately for each discriminator. The MCS is turned active by a software-triggered hardware timer, where the gate time corresponds to the actual measurement period for each data point. After the gate time has passed off, the scaler is read out by the beamline computer via TANGO.

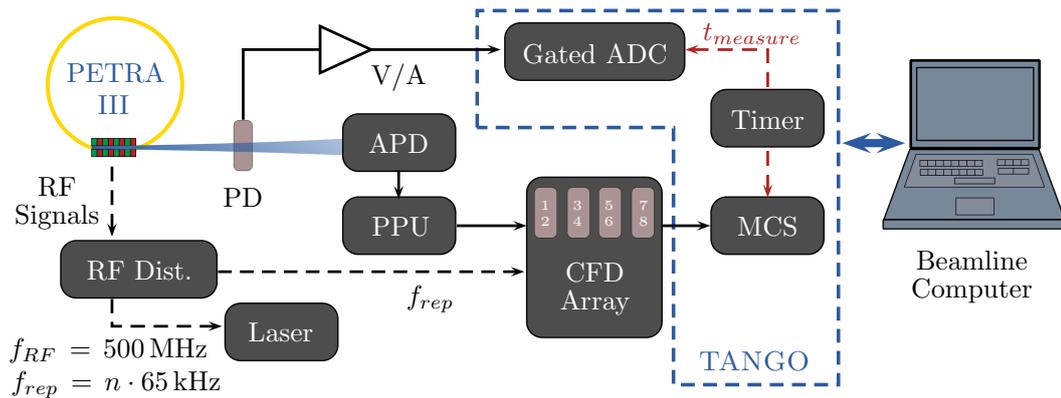


Figure 5.11.: Detailed sketch of the data acquisition circuit. RF: Radio Frequency, V/A: Volt-Amp Converter/Amplifier, t_{measure} : Measurement period, CFD: Constant Fraction Discriminator, PPU: Pulse Processing Unit, APD: Avalanche photodiode, PD: Photodiode, RF Dist: RF Distributor/Bunchclock, MCS: Multi-Channel-Scaler, ADC: Analog-to-Digital-Converter. Compare to the previous data acquisition shown in reference⁶.

The second circuit illustrates the processing of the measured photo current from the silicon photo diode for X-ray flux determination. The current signal is amplified and converted into a voltage signal, which is guided into a gated ADC⁶⁹. The ADC averages the voltage signal over exactly the same time as used for the fluorescence signal gating. After the timer has passed off, the voltage is read out by the beamline computer via TANGO.

5.7.1. Gating Structures for Bunch Selection

Ideally the data acquisition scheme utilizes the signals from all X-ray bunches for the measurements. However, within a pump and probe XAFS experiment the data acquisition is basically limited by the repetition rate of the laser system. Thus only X-ray bunches directly following the optical laser excitation have to be included for the measurement of the pumped signal. In order to optimize the signal-to-noise ratio it is favorable to always select the same bunch if the full repetition rate of the synchrotron cannot be matched by the laser repetition rate.

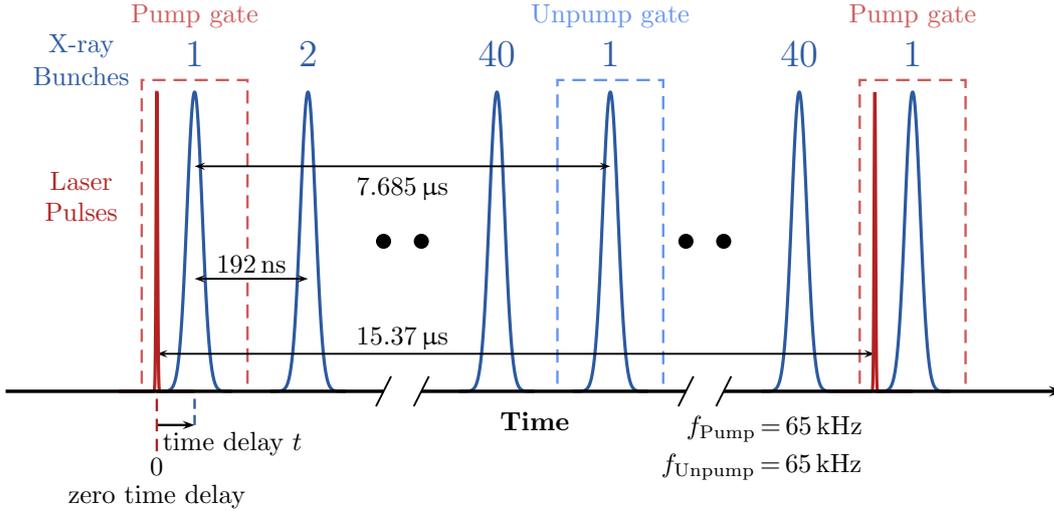


Figure 5.12.: Temporal structure of the data acquisition for 40 bunch mode and simultaneous measuring of pumped and unpumped XAFS spectra. The laser repetition rate is set to 65 kHz, leading to a data acquisition operating at 130 kHz.

For the laser system at beamline P11 basically two gating structures for bunch selection are possible. The first temporal sequence which is typically applied in the 40 bunch mode of the synchrotron is depicted in Fig. 5.12, where the laser repetition rate is set to the half of the revolution frequency of the synchrotron ($f_{\text{rep}} = 65 \text{ kHz}$). Furthermore, the X-ray bunches are well separated with 192 ns . With two gating signals equal to the laser repetition rate, this offers the possibility to measure both excited and ground state of the sample with X-rays from the same electron bunch. Thereby, the pump gate covers the X-ray bunch with prior laser excitation while the unpump gate is phase-shifted by one revolution ($7.685 \mu\text{s}$) with respect to the pump gate. In conclusion, this leads to a data acquisition processing at 130 kHz where the fluorescence signals of a single bunch are utilized for data acquisition. Additionally, the direct measurement of the unpumped signal after the pumped signal reduces the noise contributions from X-ray beam fluctuations.

The second sequence is basically used if limitations by the sample are given, in particular the lifetime of the excited state. If the lifetime exceeds the spacing of $7.685 \mu\text{s}$ between unpump and pump gate, it is not possible to measure the ground state directly after the excited state. In this case the laser repetition rate is set to 130 kHz and

only a single gate is used for the data acquisition. The pumped and unpumped signals are then measured in an On-Off-sequence. Each data point is measured alternately by turning the laser beam on and off. In this sequence noise contributions play a major role and have to be reduced. Ideally each data point should be measured over a full timing cycle of the PETRA III *top-up*. However, this gating structure can be exploited to measure so-called *molecular movies*, where multiple energy spectra are measured simultaneously at different time delays between laser excitation and X-ray pulses in order to visualize the decay of the excited state. This is achieved by setting multiple gates at the revolution frequency choosing the first adjacent bunches.

5.8. Principle of Spatial and Temporal Overlap

The spatial and temporal overlap of X-ray and laser beam plays the most significant role for pump and probe experiments. The feasibility to perform a rapid and reproducible overlap typically decides about the success of an experiment. This setup relies on a visualized spatial overlap utilizing the on-axis-microscope, while for the temporal overlap a fast photodiode mounted next to the APD detector, is required.

For spatial overlap the YAG crystal is placed in the focal plane of the on-axis microscope to visualize the X-ray beam. Afterwards, a digital marker defining the spot size and position is placed exactly at the X-ray position. The scintillator is removed and the liquid jet is roughly placed at the pre-defined X-ray position in the focal plane of the microscope to perform a motor scan. The horizontal position of the liquid jet (perpendicular to beam direction) is sequentially scanned while the fluorescence is measured in order to optimize the jet position as determined by the maximum measured fluorescence intensity. Moving the jet now to the optimized horizontal position should yield a perfect agreement with the pre-defined X-ray marker.

Afterwards, the laser beam is guided onto the liquid jet, hitting exactly in the center of the defined overlap position. In this case the visible emission of the sample, either fluorescence or phosphorescence, is exploited to visualize the laser beam. In cases where no direct emission is visible, the laser beam has to be aligned using the YAG crystal. Setting the correct vertical position corresponding to the marked X-ray beam position is very important. The horizontal position usually has to be corrected by looking at the scattered light from the liquid jet since the laser hits the sample at a different angle than the X-rays.

For temporal alignment the liquid jet is moved out and a fast photodiode (FPD), which is sensitive to both X-ray and UV/VIS radiation, is placed at the cross point of X-ray and laser beam. The FPD signal is monitored with a fast oscilloscope to obtain temporal overlap between X-ray and laser pulses. This is achieved by selecting the laser pulse which is nearest to the X-ray pulse by setting the correct Pockels cell trigger signal for the regenerative amplifier of the pump laser. Furthermore, the laser pulse can be temporally shifted in fine steps using a phase shifter (see Sec. 6.3). The entire overlap strategy is summarized and illustrated in Fig. 5.13.

5. Experimental XAFS Setup

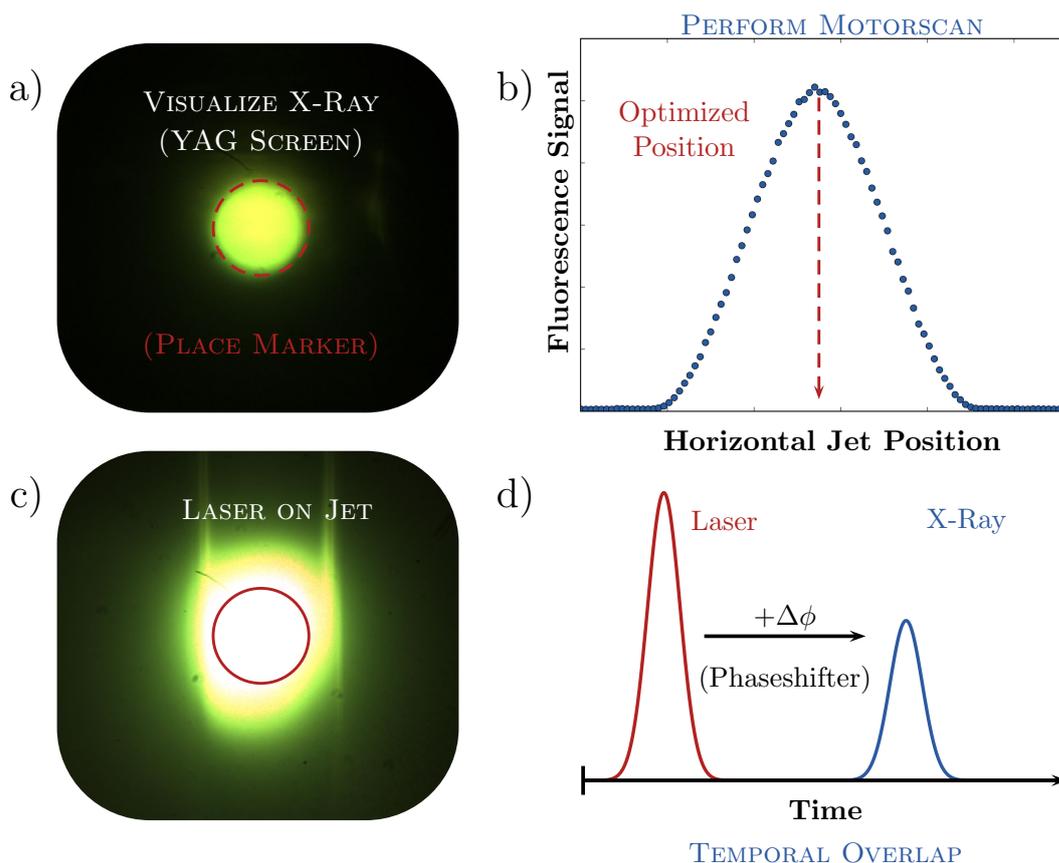


Figure 5.13.: Overlap strategy in chronological order in case of visible emission from the sample upon laser excitation.

a) At first a scintillator is placed in the focal plane of the on-axis microscope to visualize the X-ray beam. Afterwards, a marker defining the size and position is set at the X-ray position.

b) Secondly, the scintillator is removed and the liquid jet position is scanned in the focal plane of the microscope while measuring the X-ray fluorescence signal to optimize the jet position.

c) Moving the jet to the optimized horizontal position yields a perfect agreement with the pre-defined X-ray marker. In addition, the laser beam is now positioned onto the liquid jet, hitting exactly in the center of the defined overlap position.

d) After the spatial overlap, the liquid jet is moved out and a fast photodiode (FPD) is placed at the cross point of X-ray and laser beam. The FPD signal can then be monitored with an oscilloscope to visualize temporal overlap between X-ray and laser pulses. This is achieved in selecting the laser pulse which is nearest to the X-ray pulse by setting the correct Pockels cell trigger signal for the regenerative amplifier of the pump laser. Afterwards, the laser beam can be temporally shifted in fine steps utilizing the synthesizer of the synchronization unit (see Sec. 6.3).

5.9. Optimization of the Avalanche Photodiode Signal

In most fluorescence detecting experiments it is sufficient to place the detector at a right angle in the horizontal plane with respect to the X-ray beam direction, thus utilizing the horizontal beam polarization to minimize the number of measured elastically scattered photons (see Sec. 2.2.2). However, in pump and probe experiments typically small differences between the pump and unpump signals have to be resolved at high signal-to-noise ratios (see Sec. 2.3.4). For this purpose, these experiments can be conducted in a helium atmosphere to reduce the amount of air-scattered X-ray photons. However, enclosing the setup in a helium atmosphere makes the experiment not only expensive but also impractical. Therefore, a shielding aperture has been developed to reduce the influence of elastically scattered photons. The shielding principle is shown in Fig. 5.14. The core element of the shielding is a high Z material such as molybdenum

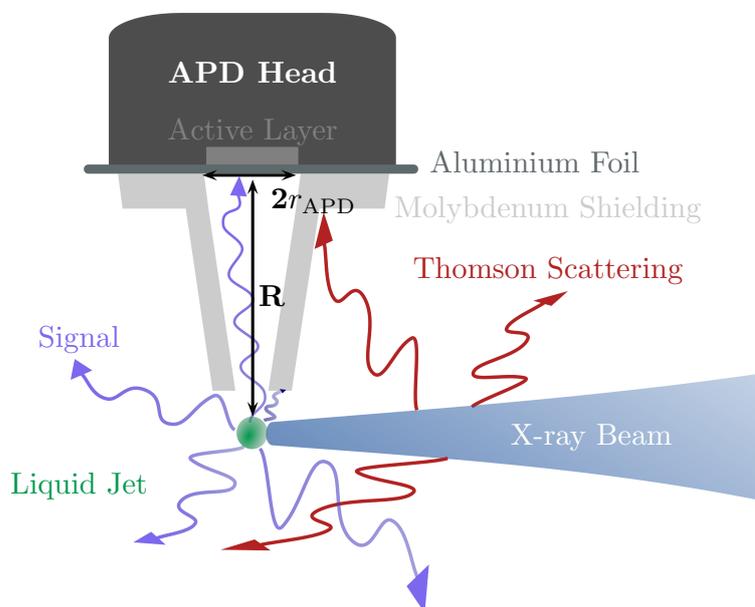


Figure 5.14.: Simplified sketch of the used avalanche photodiode shielding in order to obtain high signal-to-noise ratios by reducing the detection of air-scattered X-ray photons.

in our case, forming a cone to preserve the solid angle. With a K-shell ionization energy of roughly 20 keV⁴⁰ molybdenum is a first choice material to block elastic scattering for experiments at energies of 12 keV or below. The APD head is further shielded with an aluminum foil to suppress low energy radiation background and UV/VIS contributions.

The entrance width of the cone is fixed to 1 mm. As mentioned in Sec. 2.2, the emerging fluorescence photons from the sample are emitted isotropically and the detector solid angle Ω covers only a fraction of the total X-ray fluorescence intensity. The solid angle

5. Experimental XAFS Setup

is characterized by the active area of the APD head and its distance to the sample R^{iii} :

$$\frac{\Omega}{4\pi} = \frac{1}{4\pi} \frac{\text{Active Area}}{R^2} = \frac{1}{4\pi} \frac{\pi r_{\text{APD}}^2}{R^2}, \quad (5.3)$$

where r_{APD} denotes the radius of the active layer. In order to optimize the fluorescence signal the APD detector position is sequentially scanned at a fixed sample distance R in the horizontal and vertical direction measuring the X-ray fluorescence. A typical X-ray fluorescence map of this scan type is shown in Fig. 5.15. The optimum position

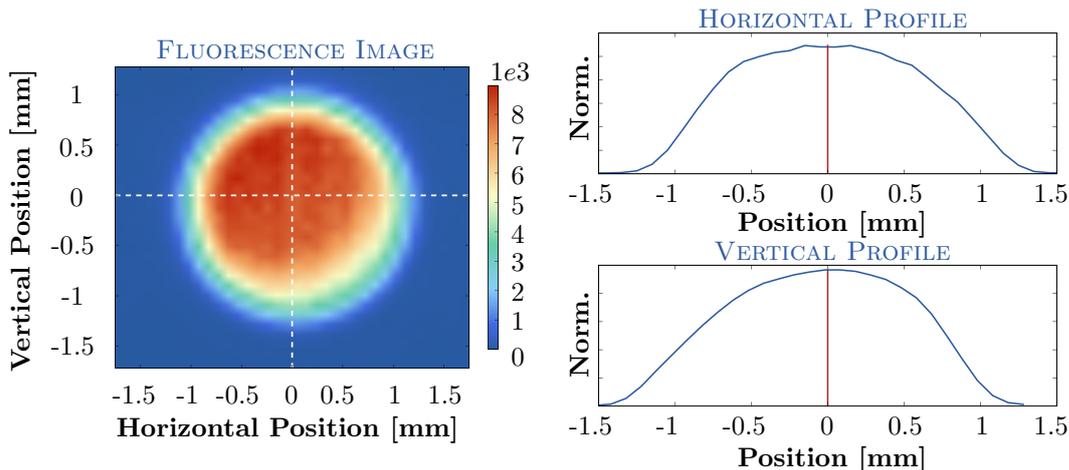


Figure 5.15.: **Left:** Measured X-ray fluorescence dependent on the lateral APD position. Within the horizontal shape of the measured X-ray fluorescence even a local minimum can be identified which can be assigned as the absolute minimum of elastic scattering, thus identifying the optimum position.

Right: Normalized averaged profile of the respective direction. The calculated optimum positions are marked with red lines.

of the detector head is simply the central position of the measured X-ray fluorescence profile in both directions. Furthermore, during this scan a jet diameter of $200 \mu\text{m}$ was used, which can even be identified as a local minimum in the horizontal profile of the measured X-ray fluorescence, delivering now the optimum position. Typically, the APD detector head is placed at a certain distance R from the sample to guarantee that the experiment is performed in the single photon counting regime.

ⁱⁱⁱCompare to previous work^{6,34}.

6. Synchronization and Stability

6.1. Theory and Principle of Feedback Control	53
6.1.1. Properties and Modifications of Control Algorithms	54
6.2. Theory of Phase Noise and Signal Source Analyzers	56
6.2.1. Measurement of Phase Noise with Signal Source Analyzers	57
6.2.2. Relationship between Phase Noise and Timing Jitter	58
6.3. Synchronization in Time-Resolved Pump and Probe Experiments	59
6.3.1. Characterization of the RF Signal	59
6.3.2. Laser Oscillator Synchronization	60
6.3.3. Laser Amplifier Synchronization	66
6.4. Laser Feedback	68
6.5. X-ray Feedback	70
6.5.1. Spatial X-ray Beam Stability at Beamline P11	73

This chapter introduces into the stability properties of the present setup, in particular the spatial and temporal stability. Within this thesis two feedback control systems for the spatial stability have been designed and implemented.

Therefore, a brief overview of theory of feedback control is given at first. Afterwards, the theory of phase noise is introduced, followed by a detailed investigation of the laser synchronization which was commissioned in the framework of this thesis at beamline P11. This chapter closes with an analysis of the spatial stability of the laser and X-ray beam.

6.1. Theory and Principle of Feedback Control

Feedback control loops are utilized for many different applications, e.g. driving of servo motors, synchronization applications or for temperature control. The most representative control mechanism is the *Proportional-Integral-Derivative-Controller* (PID) and will therefore be introduced in this section⁷⁵. The mathematical description of the parallel PID control mechanism is given by⁷⁵:

$$u(t) = K_p \left(e(t) + \frac{1}{T_i} \int_0^t e(\tau) d\tau + T_d \frac{d}{dt} e(t) \right), \quad (6.1)$$

in which K_p denotes the proportional gain, T_i the integral time, T_d the derivative time and t the actual time. The control error $e(t)$ is calculated as the difference between

6. Synchronization and Stability

a setpoint $y_{sp}(t)$ and the process output $y(t)$. Quite commonly Eq. (6.1) is rewritten as⁷⁶

$$u(t) = K_p e(t) + K_i \int_0^t e(\tau) d\tau + K_d \frac{d}{dt} e(t), \quad (6.2)$$

where K_p , K_i and K_d are now the proportional, integral and derivative gain, respectively. The most important properties are summarized in Tab. 6.1 while the information is taken from the literature⁷⁵.

Table 6.1.: Summarized PID Controller information according to the literature⁷⁵.

Term	Information	Function
Proportional	The action of the proportional term is simply linear to the actual control error. Pure proportional actions normally result in a steady-state control error.	Basic controller action.
Integral	The action of the integral term is linear to the time integral of the control error.	Removal of the steady-state control error.
Derivative	The derivative action allows the prediction of a future process output by a linear extrapolation of the error curve and consequently damps the oscillatory behaviour of the closed-loop system.	Improvement of the closed-loop stability.

6.1.1. Properties and Modifications of Control Algorithms

In this section the different characteristics and properties of control algorithms are illustrated on the basis of different simulated controllers. This section closes with a brief introduction about common modifications of control algorithms. The reader is referred to the literature⁷⁵ for a more detailed description.

A pure proportional controller action for different gains is simulated in Fig. 6.1a. It can be identified that higher proportional gains decrease the *rise time* of the controller, but additionally increase the so-called *overshoot*^{75,76}.

A simulated PI feedback control algorithm is shown in Fig. 6.1b. It is illustrated that higher integral gains cause a faster rising of the controller output, lead to an increased overshoot and, due to the oscillatory behaviour, an increased *settling time*^{75,76}.

A complete PID control algorithm is simulated in Fig. 6.1c. It is shown that the overall oscillatory process is now damped and decreases for higher derivative gains. As a consequence the settling time decreases, which in turn improves the closed-loop stability^{75,76}. The properties are summarized in Tab. 6.2 by means of increasing gains⁷⁶.

Table 6.2.: Summarized properties by means of increasing gains. Table is adapted from reference⁷⁶.

Increasing Gain	Rise Time	Overshoot	Settling Time
Proportional	Decrease	Increase	No definite trend
Integral	Decrease	Increase	Increase
Derivative	No definite trend	Decrease	Decrease

The common modifications of control algorithms, in particular the so-called *deadband*- and *integral threshold*, are explained in the following.

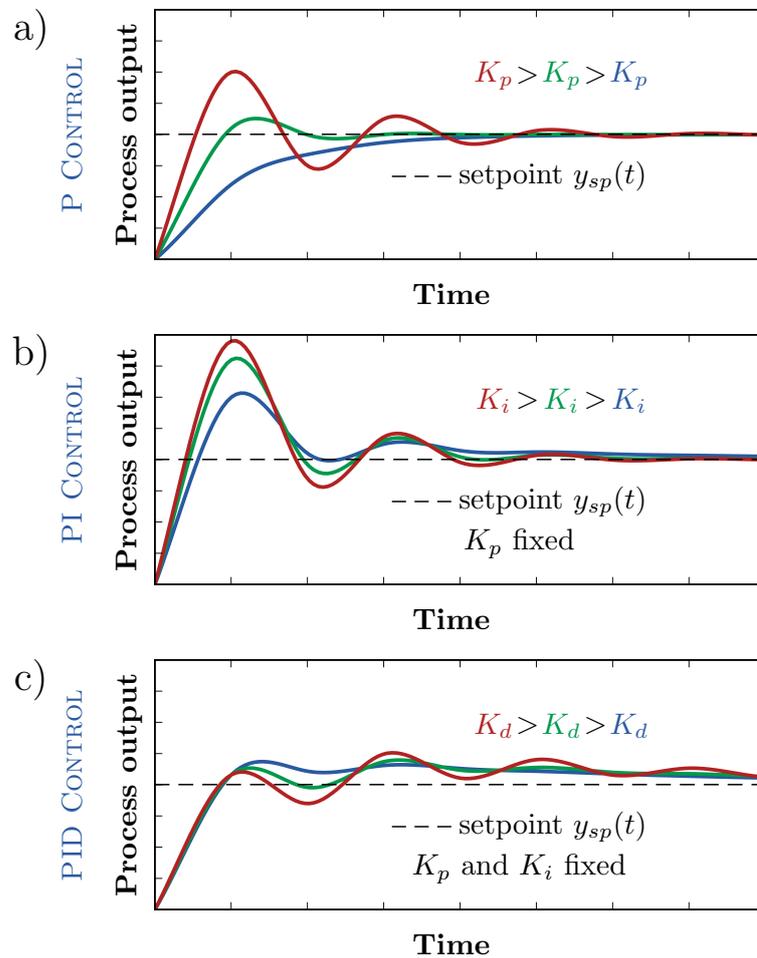


Figure 6.1.: Illustrated process output for different simulated control mechanism with varying gains. **a)** Pure proportional controller with varying gains K_p . **b)** PI controller with varying integral gains while K_p remains fixed. **c)** PID controller with varying derivative gains while K_p and K_i remain fixed.

Deadband threshold

The deadband threshold, negative as well as positive, defines a region around the desired setpoint in which no control action is performed if the actual control error lies within this region. The purpose of a deadband threshold is to make the control algorithm less sensitive to measurement noise, thus increasing the stability. Depending on different applications for feedback control, the thresholds in this framework are determined in a trial and error sequence.

Integral threshold

Integral thresholds address a nonlinear effect occurring in the nature of process outputs, the *integral windup*⁷⁵. For example motors have limitations, e.g. a limited travel range or a non-negligible amount of backlash⁷⁵.

In the first case, it is assumed that the control variable reaches the actuator limits, thus the closed loop mechanism starts to break and runs open loop⁷⁵. The motor will then physically remain at the same position independently of the controller action and thus the integral action grows larger by time, called integral windup⁷⁵.

In the second case, a backlash disturbs the controller action if the feedback direction is reversed. Usually it takes several control actions until the gear shaft has turned, thus leading to a *winded up* integral. Once the shaft starts turning, the subsequent feedback action commonly results in a strong overshoot.

Both scenarios can be prevented by limiting factors⁷⁵. In the framework of this thesis either a threshold of integral action or the limitation of the integration time, where the controller only accounts a small amount of the previous process outputs, is used.

6.2. Theory of Phase Noise and Signal Source Analyzers

Phase noise is an important element for many applications based on radio frequencies⁷⁸ and is briefly explained in the following according to the literature^{77,78}. Firstly, an ideal oscillator

$$u(t) = A_c \sin(2\pi f_c t)$$

is assumed, where f_c is the carrier frequency and A_c the corresponding amplitude⁷⁷. Performing a Fourier transformation to look closely at the related amplitude spectrum, this ideal sine signal would then appear as a sharp peak with an amplitude A_c at frequency f_c ⁷⁷. Nevertheless, in reality the oscillator performance is limited and small random signal fluctuations in amplitude and phase will occur, thus leading to the description⁷⁷

$$u(t) = [A_c + A_n(t)] \sin(2\pi f_c t + \phi(t)),$$

where $A_n(t)$ and $\phi(t)$ are noise contributions in amplitude and in phase, respectively. These contributions lead to additional spectral components in the amplitude spectrum, whereupon in the power spectral density \mathcal{S}_Φ sidebands are formed, centered around the carrier frequency f_c ⁷⁷. The two-sided power spectral density describes phase variations

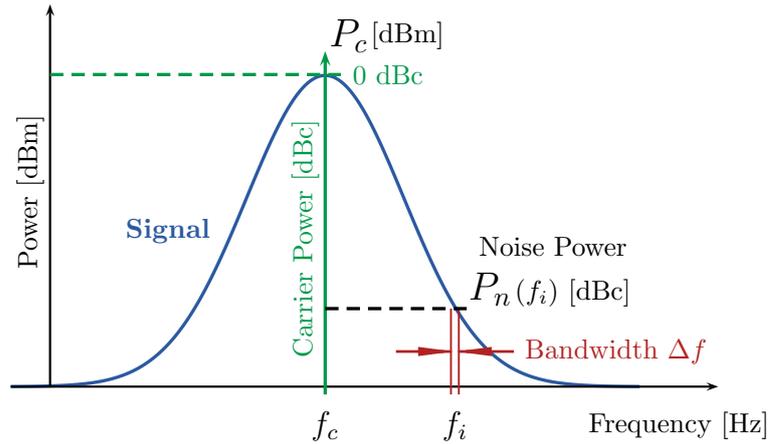


Figure 6.2.: Determination of the single sideband phase noise \mathcal{S}_Φ . f_i : Offset frequency, Δf : Bandwidth, f_c : Carrier frequency, P_c : Total carrier power, $P_n(f_i)$: Noise power at offset frequency f_i . Figure is redrawn and based on reference^{77,78}.

(rms) as a continuous function for a given bandwidth⁷⁸. Consequently the phase noise $\mathcal{L}_\Phi(f_i)$ is defined as the single sideband power $P_n(f_i)$ referenced to the total carrier power P_c per bandwidth Δf ⁷⁷ⁱ

$$\mathcal{L}_\Phi(f_i) = \frac{P_n(f_i)}{P_c \cdot \Delta f}, \quad (6.3)$$

where $f_i = f - f_c$ denotes the offset frequency from the carrier. The determined phase noise is commonly expressed in decibel relative to the carrier power per Herz [dBc/Hz]^{77,78}.

6.2.1. Measurement of Phase Noise with Signal Source Analyzers

Phase noise measurements can be performed with a so-called *signal source analyzer* (SSA). The operation principle and signal course is shown in Fig. 6.3.

First of all, the signal is band-pass filtered in order to define the carrier frequency f_c . Inside the analyzer the carrier frequency f_c is automatically detected and then synthesized by an internal low noise and temperature stabilized oscillator. Both signals are subsequently mixed and low-pass filtered. The resulting signal is amplified and then Fourier transformed to determine the phase noise data as described in Eq. (6.3).

Typically the measurement bandwidth used is larger than 1 Hz, due to technical reasons as it would require a very narrow band-pass filter⁷⁸. Therefore, a wider band-pass window is chosen and the data sets are later on mathematically extrapolated to 1 Hz measurement bandwidth⁷⁸.

Phase noise measurements are typically limited by thermal noise, which is at room-temperature -174 dBm/Hz⁷⁷.

ⁱThe relationship between power density and phase noise is given by⁷⁷ $\mathcal{L}_\Phi(f_i) = \frac{1}{2} \mathcal{S}_\Phi(f_i)$.

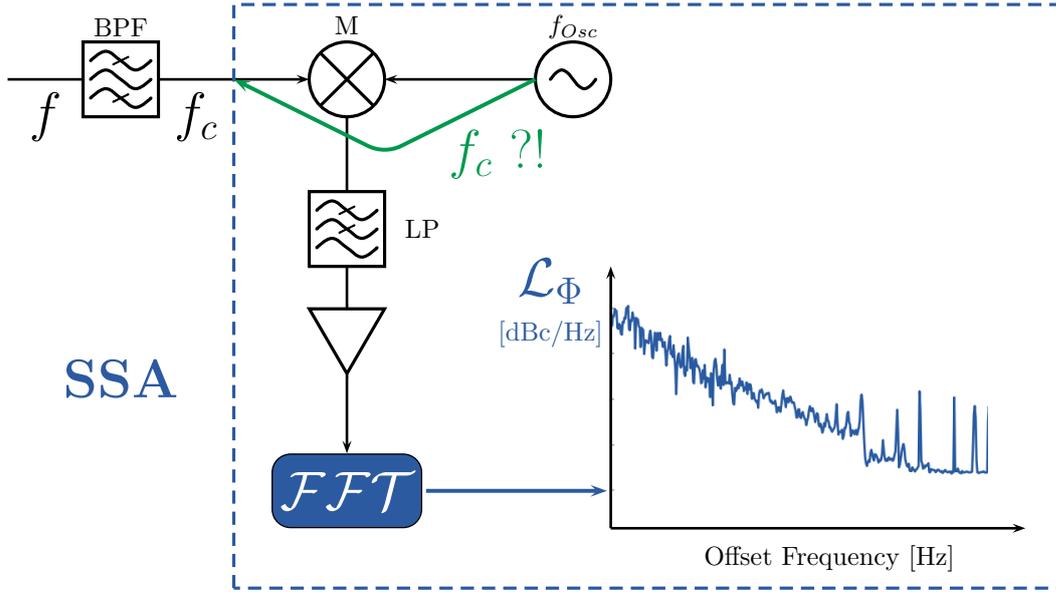


Figure 6.3.: Principle of operation of a signal source analyzer (SSA). f_c : Carrier frequency, f : Frequency, f_{Osc} : Oscillator frequency, $\mathcal{F}\mathcal{F}\mathcal{T}$: Fast Fourier Transform, \mathcal{L}_Φ : Single sideband phase noise, M: RF Mixer, BPF: RF Band-pass filter. Figure is based on reference⁷⁹.

6.2.2. Relationship between Phase Noise and Timing Jitter

According to the literature⁸¹, the timing error Δt of a pulse is defined as the deviation of the related temporal position from a reference. Here a necessary criterion lies in the assumption that the pulses can be separated from each other⁸¹. Treating the reference as the related pulse position of a theoretical source without any noise contributions, the actual temporal pulse position can be linked to a phase error⁸¹ⁱⁱ

$$\Delta\phi = 2\pi f_c \Delta t, \quad (6.4)$$

where f_c denotes for example the carrier frequency. The single sideband phase noise $\mathcal{L}_\phi(f_i)$ can also be expressed as⁸⁰ⁱⁱⁱ

$$\mathcal{L}_\phi(f_i) = \frac{\Delta\phi_{\text{rms}}^2}{\Delta f} \quad \text{with} \quad f_i = f - f_c, \quad (6.5)$$

where $\Delta\phi_{\text{rms}}$ is the rms phase variation of the carrier frequency, f_i the offset frequency and Δf is the measurement bandwidth (see Fig. 6.2).

In case of pulsed laser sources the carrier frequency f_c is typically selected out of the (electronic) Fourier comb of the oscillator pulse train with a band-pass filter after detection with a fast photodiode⁸⁰. By using the relationship between the spectral power density \mathcal{S}_Φ and the timing jitter density $\mathcal{S}_{\Delta t}$ ^{81,82}

$$\mathcal{S}_\Phi(f_i) = (2\pi f_c)^2 \mathcal{S}_{\Delta t}(f_i) \quad \text{with} \quad \mathcal{L}_\Phi(f_i) = \frac{1}{2} \mathcal{S}_\Phi(f_i),$$

ⁱⁱCan also be compared to reference⁸⁰.

ⁱⁱⁱThe ongoing description follows reference⁸⁰ which is based on the literature^{81,82}.

the latter can be directly derived as⁸⁰

$$\mathcal{S}_{\Delta t}(f_i) = \frac{2}{(2\pi f_c)^2} \mathcal{L}_{\phi}(f_i). \quad (6.6)$$

The integral of the spectral timing jitter density provides the square of the timing jitter in a defined offset frequency interval $f_i = [f_1, f_2]$ ⁸⁰:

$$\Delta t_{\text{rms}}(f_1, f_2) = \sqrt{\int_{f_1}^{f_2} \mathcal{S}_{\Delta t}(f_i) df_i}, \quad (6.7)$$

which is similar to the expression that power density spectra describe rms phase variations. This relationship is utilized in this framework to calculate the timing jitter from the measured phase noise of a spectrum analyzer.

6.3. Synchronization in Time-Resolved Pump and Probe Experiments

As described in Sec. 4.1.1, the synchrotron PETRA III is operated with a 500 MHz reference radio frequency. For time-resolved pump and probe experiments at beamline P11 the installed laser system (see Sec. 5.2) has to be synchronized to this reference at a small timing jitter to achieve a temporal resolution equal to the X-ray bunch length of PETRA III. Therefore, this section presents the characterization of the PETRA III master reference and the determination of timing jitter contributions from the pump laser system at beamline P11.

6.3.1. Characterization of the RF Signal

The 500 MHz RF signal is distributed electrically through the PETRA III hall to the different beamlines. A device called *bunchclock* can be connected to the 500 MHz distributor to extract both the revolution frequency and sub-harmonics of the RF signal. Various experimental devices which require a timing input can be synchronized to these signals.

In order to characterize the reference quality, the phase noise was measured with a signal source analyzer to determine the timing jitter according to Eq. (6.7). The outcome is shown in Fig. 6.4, where the green curve represents the measured phase noise and the red curve the integrated timing jitter.

Following the phase noise curve from low to high offset frequencies, two nearly linear sections can be identified, which are most likely the result of a phase-locked reference to low noise oscillators. Most of the timing jitter originates from low frequencies towards 100 Hz, especially at the offset frequency of $f_i = 100$ Hz an important spike caused by an harmonic of alternating current (AC) noise can be identified.

However, the integrated timing jitter of $\Delta t_{\text{rms}} = 452.2$ fs in the frequency interval of $f_i = [10 \text{ Hz}, 10 \text{ MHz}]$ is sufficient for the experiments described in this thesis.

6. Synchronization and Stability

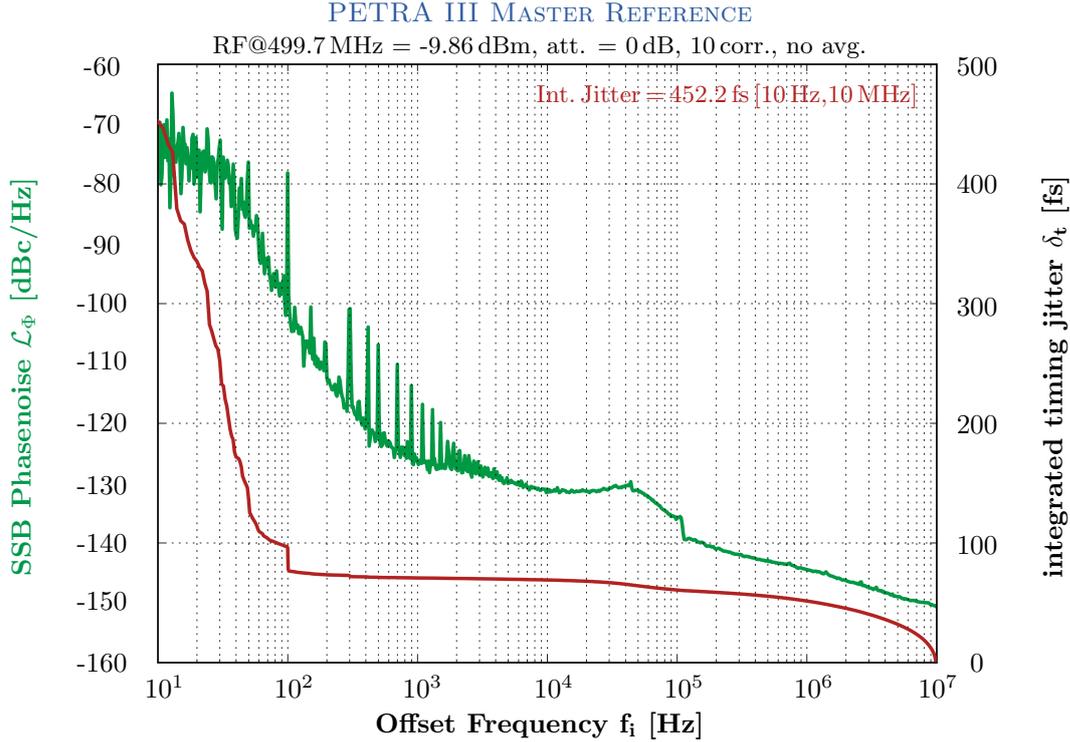


Figure 6.4.: Measured single sideband phase noise (dark blue) of the PETRA III reference and calculated timing jitter (red).

6.3.2. Laser Oscillator Synchronization

In order to perform time-resolved pump and probe experiments, the laser oscillator pulse train is synchronized to the PETRA III synchrotron by a so-called *phase-lock*⁸⁴, which is related to a constant phase offset between the cavity frequency and the PETRA III master reference (500 MHz). For this purpose, a custom oscillator with a repetition rate of about 83.3 MHz has been designed by the manufacturer *Light Conversion* in order to be consistent with the 6th sub-harmonic of the inherent RF at PETRA III. In addition, the oscillator houses two different piezoelectric actuators, which are connected to folding mirrors⁸³. One actuator features a high resonance frequency, while the other actuator controls a mirror at a low resonance frequency⁸³. The fast actuator exhibits a small stroke and retains the phase-lock at a small timing jitter, while the other one exhibits a huge stroke to maintain long-term stability^{83,84}. In addition, the fast piezoelectric actuator covers one beam reflection per round-trip, while the slow piezoelectric actuator features two beam reflections per round-trip to increase the total covered beam path⁸³.

The diagram of the implemented *phase-locked loop* (PLL) at beamline P11 is shown in Fig. 6.5. Key element of the phase-locked loop in Fig. 6.5 is the phase detector, which is explained in a simplified way in the following. The description is based on reference^{84,85}.

On the one hand, the 500 MHz PETRA III master reference is mixed with a low noise

Table 6.3.: Properties of the piezoelectric actuators inside the laser oscillator. (a): Measured with a spectrum analyzer (not shown here). (b): These parameters are factory values, in practice the distance covered by the low resonance piezo is around 3300 Hz. Magnitudes are taken from reference⁸³.

Type	High Resonance	Low Resonance
Resonance Frequency	~ 500 kHz	5 kHz
Loaded Resonance	~ 100 kHz ^a	Unknown
Stroke	$2 \mu m$	$12 \mu m$
Mirror Reflections	1	2
Distance covered	100 Hz	2200 Hz ^b

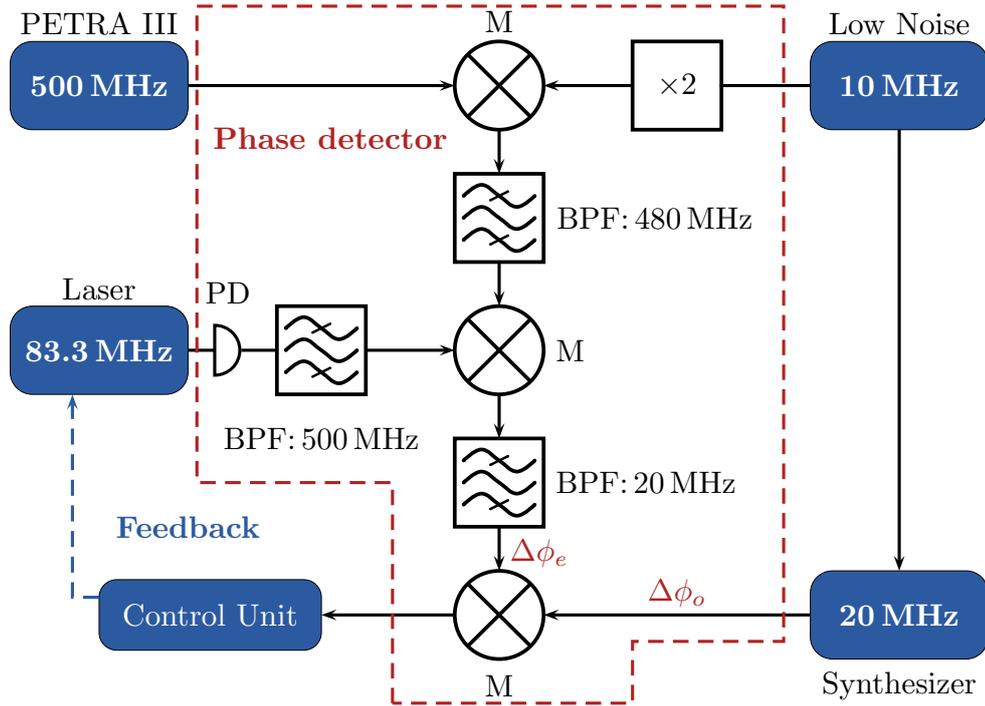


Figure 6.5.: Diagram of the realized phase-locked loop. M: RF mixer; PD: Fast photodiode; BPF: RF Band-pass filter. Figure is based on reference⁸⁴.

20 MHz reference directly followed by a band-pass filter passing only the 480 MHz. On the other hand, a small fraction of the laser beam oscillating at 83.3 MHz inside the cavity is guided onto a fast InGaAs photodiode, which is subsequently followed by a band-pass filter screening the 6th harmonic out of the electronic Fourier comb of the oscillator pulse train^{iv}. The photodiode is saturated in order to prevent amplitude-to-phase conversions^v. Afterwards, this 500 MHz signal and the 480 MHz signal originating from the master reference are mixed and band-pass filtered again, thus leaving a 20 MHz signal with the imprinted phase error $\Delta\phi_e$. The imprinted phase error repre-

^{iv}Compare to Sec. 6.2.2 for the definition of the carrier frequency f_c in case of phase noise measurements

^vThe reader is referred to reference⁸⁶, where a linear behavior of amplitude-to-phase conversion is illustrated.

6. Synchronization and Stability

sents the cavity distance from the master reference (see Eq. (6.4)).

Furthermore, a synthesizer provides a low noise 20 MHz signal with an adjustable phase offset $\Delta\phi_o$.

Mixing both 20 MHz signals leads to a new signal containing an overall phase error $\Delta\phi = \Delta\phi_e - \Delta\phi_o$, which is further utilized by the control unit of the PLL. Hence, by adjusting the phase offset of the synthesizer the laser pulses can be phase-shifted with respect to the master reference.

In order to adjust the cavity length to correct for the phase error $\Delta\phi$, the control unit translates the latter into a high voltage to control the piezoelectric actuators. By performing the phase correction many thousand times per second this ensures a constant phase offset between the PETRA III reference and the laser cavity.

Retaining a constant phase offset between laser oscillator and synchrotron is preserved by an interplay of both piezoelectric actuators. The fast actuator can rapidly balance small errors up to $\pm 50 \text{ Hz}^{\text{vi}}$, while in case of long-term drifts - hence exceeding its stroke - the other actuator compensates in a way that the former can center back between its limits. Moreover, the control unit has been programmed and can be externally controlled by the TANGO System at PETRA III.

Active Phase-Lock - Measurements

In the following the PLL performance is characterized on the basis of phase noise measurements with a signal source analyzer. For this purpose, the laser oscillator signal, provided by the fast photodiode inside the synchronization unit and containing the phase error $\Delta\phi_e$, was divided by an RF splitter into two signals. One signal was required to maintain the PLL operation. The other signal was firstly screened by a 500 MHz band-pass filter in order to define the carrier frequency f_c and afterwards fed into the signal source analyzer.

The measurements were performed together with Moritz Schlie who simultaneously characterized a similar laser system as part of his work⁷. The measurements and line of argumentation^{79,80} can therefore be fully compared. The author appreciates the strong support by Sebastian Schulz during measurements.

First of all, the phase noise of the free-running oscillator was characterized, which is shown in Fig. 6.6. The curve shows a typical course with an integrated timing jitter of $\Delta t_{\text{rms}} = 785.4 \text{ fs}$ in the frequency interval of $f_i = [10 \text{ Hz}, 10 \text{ MHz}]$. In addition, it can be identified that the interception point of laser oscillator and master reference is around the offset frequency of $f_i = 10 \text{ kHz}$. Afterwards, the oscillator has a slightly better phase noise progression which motivates to aim for a high locking bandwidth.

The phase-locked oscillator shows an integrated timing jitter reduced by approximately 260 fs to $\Delta t_{\text{rms}} = 526.6 \text{ fs}$ in the same frequency interval (see Fig. 6.7). Noticeable is the phase noise progression towards the offset frequency of $f_i = 100 \text{ Hz}$, at this point the phase-locked oscillator curve leaves the reference providing evidence that the PLL locking bandwidth is most likely close to 100 Hz. In addition, a large increase of timing jitter caused by AC noise at the same offset frequency is appearing, which could not be

^{vi}This magnitude is with respect to 83.3 MHz. The full stroke is typically not utilized during phase-lock for stability reasons as will be shown later.

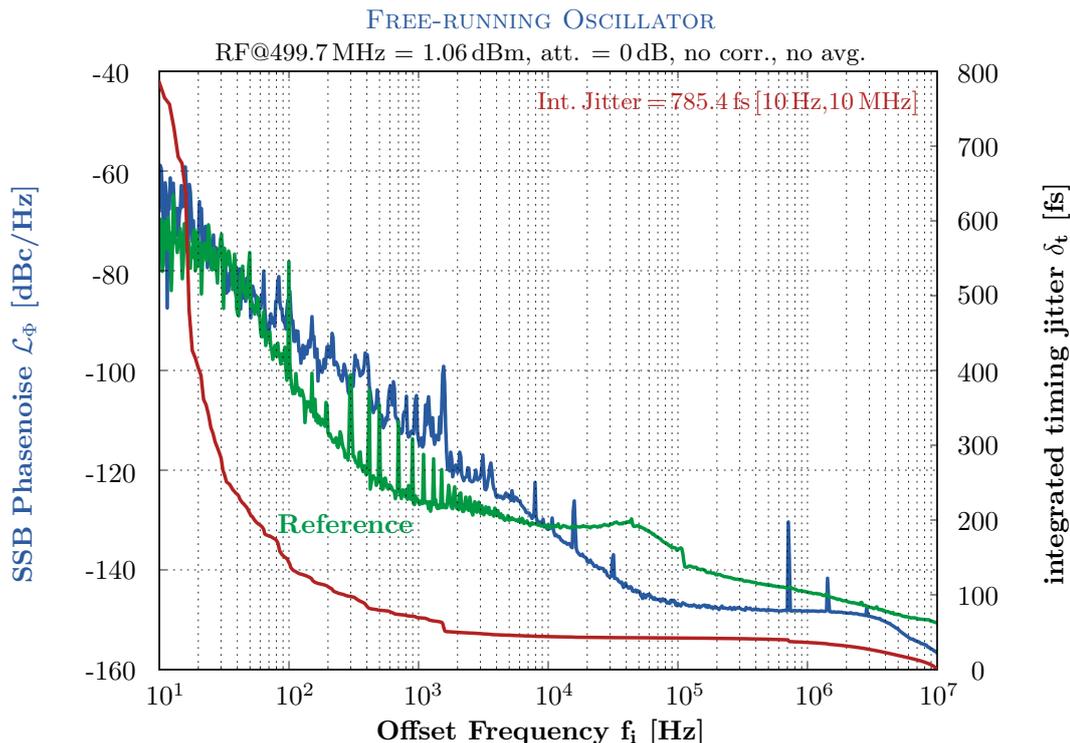


Figure 6.6.: Measured single sideband phase noise (blue) of the free-running oscillator and reference (green) with calculated timing jitter (red).

observed in the timing jitter of the free-running oscillator. For the present piezoelectric actuator setup, the resonance frequency of the fast actuator is around 100 kHz, one would commonly expect a considerably larger locking bandwidth (\sim kHz).

A similar laser system with a single piezoelectric actuator for phase-locking was investigated in a previous work⁷. This laser system shows a similar phase noise progression and locking bandwidth while the actuator exhibits a resonance frequency of only < 1 kHz⁷. This leads to the assumption that the quality of the PETRA III master reference could be a limiting factor for phase-locking. However, further investigated phase-locked loop performances of different laser oscillators are required to sustain this assumption.

The increase of phase noise occurring in the phase-locked oscillator measurement after the offset frequency of $f_i = 100$ Hz is related to the phase-locked loop control parameters and increases by increasing the actuator gains in the feedback control mechanism^{vii}. Typically, it is beneficial to avoid control settings, which produce these features. However, for the present installation it turned out that higher actuator gains driving the fast piezoelectric actuator close to its resonance frequency led to a decrease of timing jitter by simultaneously increasing the spectral actuator feature.

Subsequently the behavior of the phase-locked oscillator with an activated regenerative

^{vii}This was shown during measurements and is also noticeable by comparing the phase noise measurements between the free-running and the phase-locked oscillator. This spectral feature is completely missing in the phase noise of the free-running oscillator. Compare to previous work⁷.

6. Synchronization and Stability

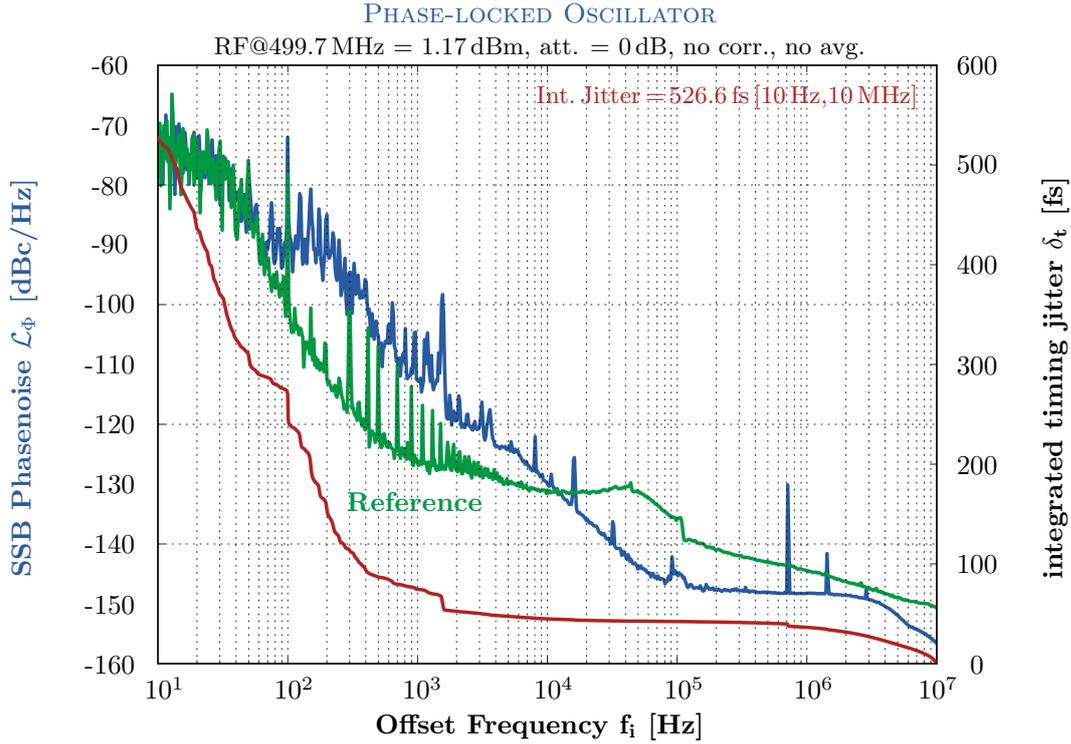


Figure 6.7.: Measured single sideband phase noise (blue) of the phase-locked oscillator and reference (green) with calculated timing jitter (red).

amplifier at a repetition rate of $f_{\text{rep}} = 130$ kHz was studied. Thereby, the timing jitter is considerably increased by ≈ 520 fs to $\Delta t_{\text{rms}} = 1060.2$ fs in the frequency interval of $f_i = [10 \text{ Hz}, 10 \text{ MHz}]$, resulting from back reflections of the regenerative amplifier towards the oscillator. This can be identified since spikes are appearing in the phase noise at the fundamental repetition rate as well as its related higher harmonics. However, the synchronization and thus the experiment is not affected for frequencies below the repetition rate as shown by a timing jitter calculation (pale blue) in the offset frequency interval of $f_i = [10 \text{ Hz}, 100 \text{ kHz}]$. The overall PLL contribution is sufficient and negligible as the PETRA III bunch length is assumed to be around 44 ps rms.

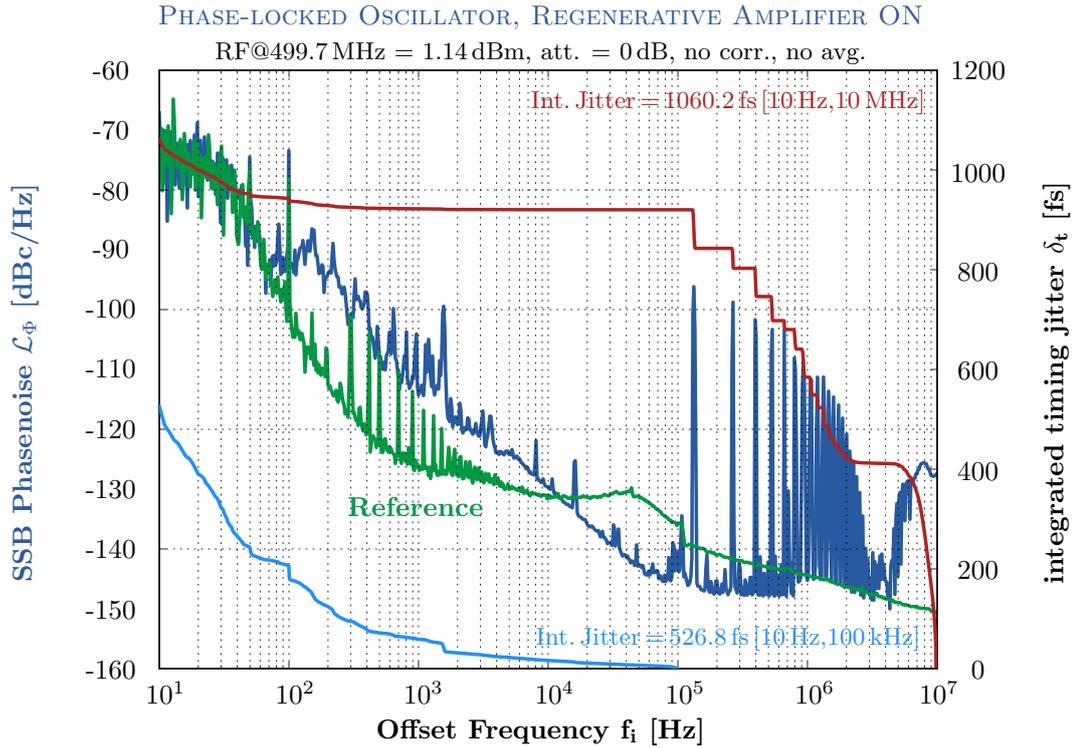


Figure 6.8.: Measured single sideband phase noise (blue) of the phase-locked oscillator with activated regenerative amplifier and reference (green) with calculated timing jitter (red and pale blue).

Measured Piezoelectric Actuator Interplay and Long-Term Stability

As mentioned in Sec. 6.3.2, both piezoelectric actuators conduct an interplay between each other in order to achieve a combination of long-term stability and a small timing jitter during phase-lock. In more detail, the fast actuator is driven by high voltages originating from a translated control unit signal between 0 and 10 V.

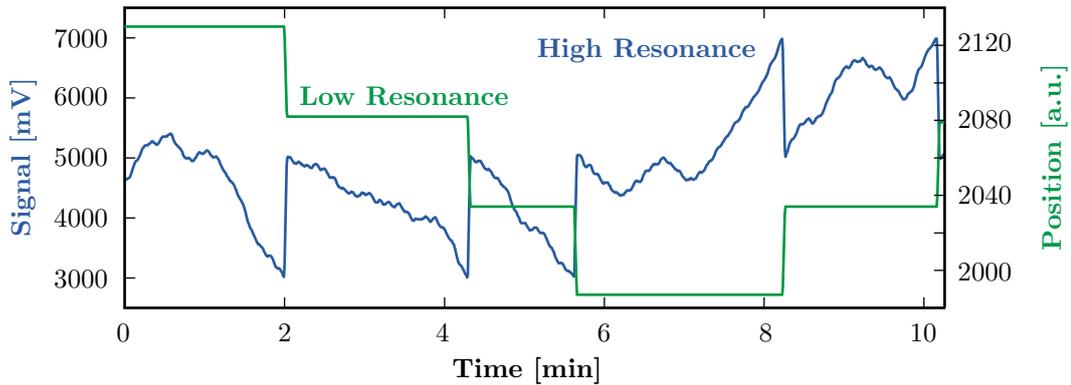


Figure 6.9.: Measured interplay between both piezo actuators inside laser oscillator.

6. Synchronization and Stability

Every time the control signal reaches a preset upper or lower threshold, the slow piezoelectric actuator is consulted for phase-locking and moves in a way that the fast actuator can center back between its limits⁸⁴. This interplay is shown in Fig. 6.9, where the lower and upper threshold is set to 3000 mV and 7000 mV, respectively. More specifically, when the fast actuator (blue curve) reaches a preset threshold, either 3000 mV or 7000 mV, the slow actuator (green curve) supports the phase-lock operation so that the control signal of the fast actuator can be centered back to 5000 mV. This measurement can be utilized in the following. The total drift between the PETRA III master reference and the PHAROS oscillator can be derived by transforming the position of the slow piezoelectric actuator to frequency values, leaving only a small uncertainty caused by the position of the fast actuator. The measured drift is shown

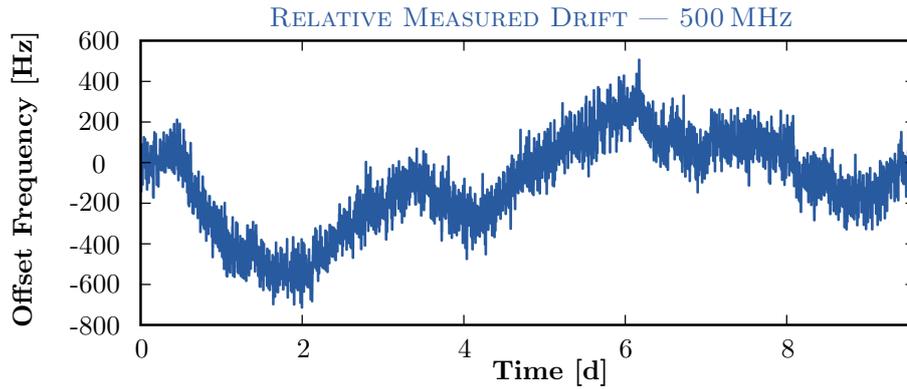


Figure 6.10.: Measured drift between the PETRA III master reference and the PHAROS oscillator utilizing the piezoelectric actuators inside the laser cavity.

in Fig. 6.10 and reveals an absolute maximum difference of approximately 1 kHz over ten days. Since the slow actuator covers an overall frequency range of $6 \cdot 3.3 \text{ kHz} \approx 20 \text{ kHz}$ with respect to the master frequency, the long-term stability of the phase-lock is guaranteed.

6.3.3. Laser Amplifier Synchronization

The synchronization of the regenerative amplifier is independent from the oscillator phase-locking and will be explained in the following on the basis of reference⁶⁴. As mentioned earlier, the existing bunchclock device provides sub-harmonic reference signals which can be selected as the desired laser repetition rate. In addition, each signal originating from the bunchclock can be temporally shifted in nanosecond steps. Fig. 6.11 shows a diagram of the internal timing electronics of the pump laser. The user-input signal directly initiates the internal *sync signal* and triggers the Pockels cell from the regenerative amplifier, combining both the *RA On* and *RA Off* signal for the amplification of the oscillator pulses. Afterwards, the second Pockels cell, acting as *pulse picker*, is automatically triggered to release the amplified laser pulse.

For a better practical understanding and with regard to the temporal overlap of X-ray

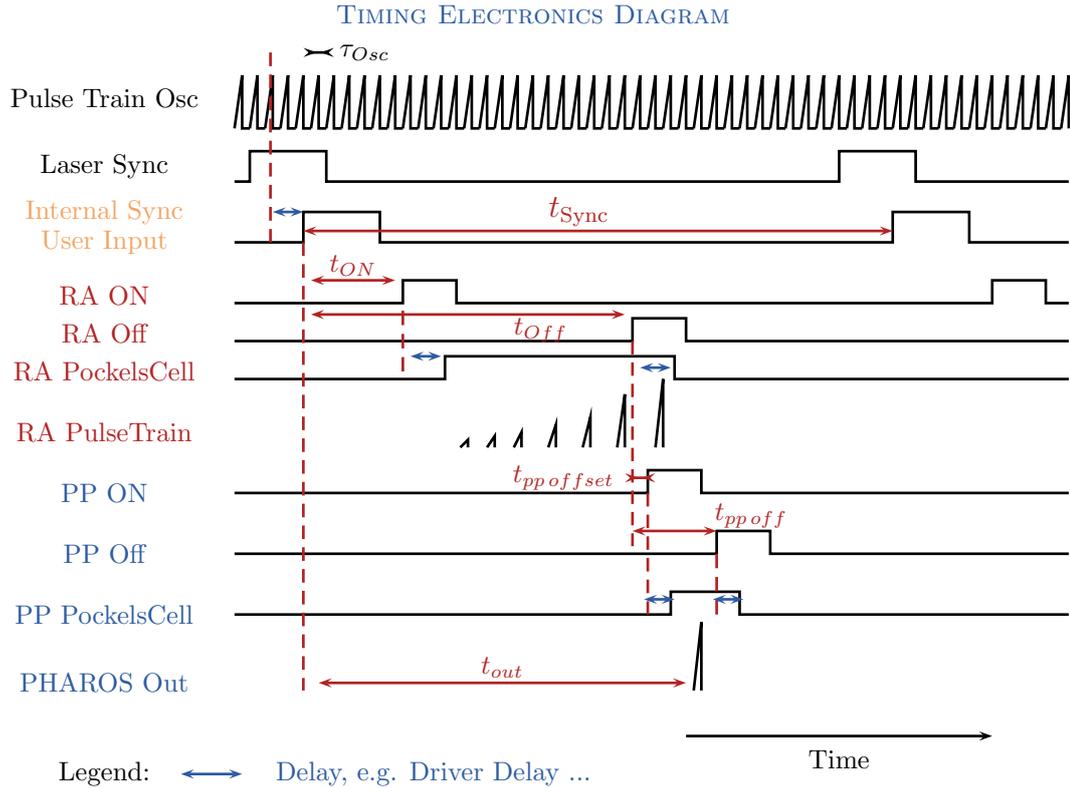


Figure 6.11.: Diagram of the user input signal passing through the timing electronics of the pump laser. τ_{Osc} : Oscillator period, RA: Regenerative amplifier, t_{ON} : RA on delay, PP: Pulse picker; t_{Off} : RA Off delay, t_{pp_offset} : Pulse picker offset, t_{pp_off} : PP Off delay to PP ON. Figure is based on reference⁶⁴.

and laser pulses, a simplified picture is shown in Fig. 6.12. Thereby, the oscillator pulse train and the so-called *Pockels cell window* are shown. The window has a length related to the oscillator frequency of roughly 12 ns and its repetition rate is directly referred to the user input. Shifting this window, e.g. with a delay generator, does not have an effect on the pulse position itself. Instead, one can choose a desired pulse out of the pulse train to be amplified and passed out. In order to shift the pulse position inside the Pockels cell window it is necessary to utilize the synthesizer as described in Sec. 6.3.2.

6. Synchronization and Stability

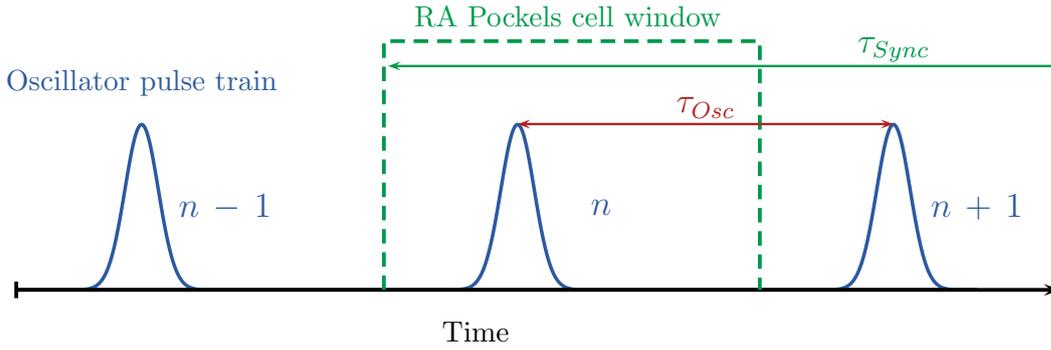


Figure 6.12.: Simplified picture of the Pockels cell window (green).

6.4. Laser Feedback

Within this thesis, an optical feedback system, compatible to the inherent TANGO system at PETRA III, was constructed and programmed with the motivation for time-resolved micro-crystallography where the illuminated sample area is given by a few microns. Nevertheless, this control setup can also be utilized for the XAFS experiments.

Firstly equipped with two quadrant sensors for beam position detection, the feedback control mechanism can also work with fast CCD cameras combined with scintillators as detectors. Therefore, the on-axis microscope, described in Sec. 5.4, can be straightforwardly utilized while the sample solution itself during the experiment is used as a scintillator to observe the beam position.

Table 6.4.: Properties of the piezoelectric ceramics utilized for the optical feedback.

Parameter	Magnitude
Stroke	23 μm
Loaded Resonance	several kHz
Control Bias	-10 V ... +10 V

In order to provide a user-friendly beamline operation a Python⁸⁸ based software as well as a user-friendly interface based on the PyQt package has been written. The software frequently transforms the UV/VIS beam exposure on the CCD camera into virtual beam positions and subsequently calculates the control errors, which are further utilized by a control algorithm as described in Sec. 6.1. For adjustment control, a mirror system driven by piezoelectric ceramics, is installed. These ceramics are operated by high voltages originating from a controller unit, which is in turn controlled by analog-to-digital converters. The piezoceramics feature a maximum stroke of 23 μm in both horizontal and vertical direction (see Tab. 6.4), which leads to feasible compensated deviations up to 100 μm for the existing XAFS setup. The bandwidth is limited by the used CCD camera, however, for mainly thermal drift compensation only a feedback control of a few Hz is required. The working principle of the control mechanism is illustrated in Fig. 6.13, showing an active lock-run of the laser beam to the preset

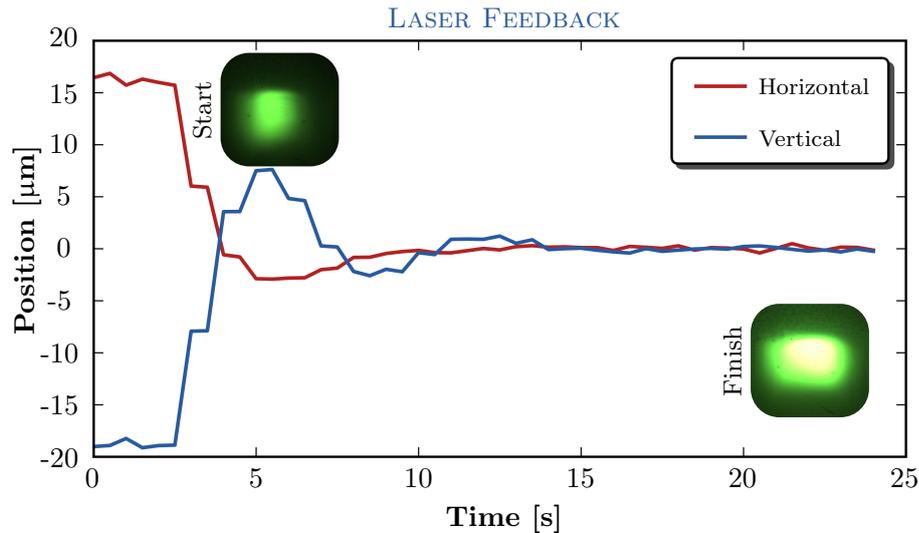


Figure 6.13.: Illustration of the working principle of the optical feedback loop. The laser beam excites the sample molecules inside the liquid jet. The visible luminescence is used to lock the beam position in the on-axis microscope used in the XAFS setup.

position utilizing the outgoing luminescence from the sample for position detection. The laser feedback control mechanism was commissioned for different moderate actuator (PID) gain settings. Limiting factors in the control algorithm were not necessary and the only concern was the laser safety and a stable long-term operation. Therefore, the developed software automatically pauses the control action if a Pockels cell, e.g. the pulse picker, inside the laser system shuts the beam. Afterwards, the software automatically resumes the feedback operation if the Pockels cell is turned active again. This procedure is mandatory since the XAFS measurements are typically performed in a step scan operation, in which the UV/VIS beam is closed while the X-ray monochromator is approaching for a new energy, to avoid unnecessary sample degradations. For general safety concerns the feedback control algorithm is automatically stopped (no resume) if the safety interlock of the experimental hutch is broken. In general, the laser system at beamline P11 proved to be absolutely long-term stable due to the fact that it is mounted on the same solid granite support as the XAFS setup. Drifts only occurred with a maximum deviation of a few microns at the sample position in case of the XAFS setup. These small deviations are negligible in cases of sample and laser beam sizes around 100-200 μm . Nevertheless, this setup is a powerful tool to align the UV/VIS beam from the outside of the experimental hutch and to fine tune the spatial overlap between X-ray and laser beam.

6. Synchronization and Stability

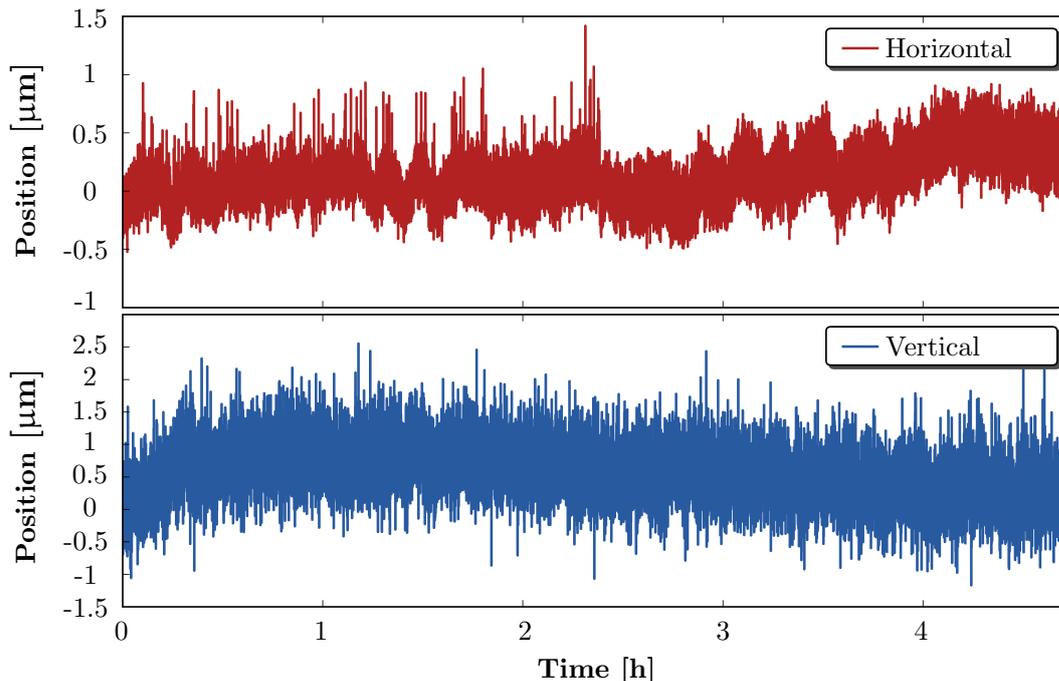


Figure 6.14.: Typically measured laser beam position variations during an experiment showing the spatial drift of the laser beam measured over roughly 5 hours. **Top:** Horizontal beam position; **Bottom:** Vertical beam position.

6.5. X-ray Feedback

During the last years many efforts were put into the development of new ways to stabilize X-ray beams. For example fluorescent foils can be utilized to optically visualize the X-ray beam position while monitoring the foils with fast cameras providing information for feedback control. However, this method lacks information about the incident photon flux and, due to the nature of the scintillator, a precise position detection down to a few micrometer.

Another way to monitor the beam position is to place small slits or blades within the beam propagation while monitoring the outgoing photon flux with diamond foils or ion chambers working in transmission mode. Whenever the flux drops, an optical element can be moved until the flux reaches its maximum back again. On the one hand, this method exhibits the advantage of a precise photon flux determination. On the other hand, it lacks a two dimensional position information, causing the control mechanism to revise the feedback direction in a trial and error sequence.

Within this thesis and for the first time at DESY, a newly in-house developed diamond foil *X-ray Beam Position Monitor* (XBPM) has been characterized, installed and programmed for user operation. Photographs of both the XBPM front- and backside are shown in Fig. 6.15. The concept and working principle derives from the well-known quadrant detectors commonly used in laser optics. The core element of this detector is a CVD (*Chemical Vapor Deposition*) diamond foil, which exhibits the feature to be

X-RAY BEAM POSITION MONITOR



Figure 6.15.: Photographs of the X-ray Beam Position Monitor (XBPM). **Left:** Frontside, **Right:** Backside. [By Courtesy of B. Steffen].

Table 6.5.: Detailed parameters of the installed XBPM at Beamline P11. **(a)**: This resolution was characterized during this thesis (not shown here). Magnitudes are taken from reference⁸⁷.

Type	Value
Foil	CVD Diamond
Thickness (Foil)	10 μm
Coating	Aluminum/Titan
Thickness (Coating)	200 nm/10 nm
Active radius	5 mm
Horizontal gap	50 μm
Vertical gap	20 μm
Resolution ^a	$\approx 1.75 \mu\text{m}$

highly transparent for X-rays. For this purpose, a foil of only 10 μm thickness is used to preserve the high photon flux while operating in transmission mode (see Fig. 6.17). Finally, to construct electrical contacts, the foil is primarily coated with 10 nm titan serving as a bonding agent for the later on coated 200 nm aluminum (see Tab. 6.5), thus designing four quadrants at where the current can be measured. The XBPM has to be operated in vacuum, therefore, one is placed inside the intermediate focus chamber (see Sec. 4.2.4) as first element for feedback control and another BPM is directly placed before the KB system to visualize the outgoing X-ray beam from the monochromator. The placement of the XBPM in the chamber as first element is of strategic interest. This leads to the possibility to measure the full photon flux before any significant beam manipulation by pinholes or slit systems occurs. An overview about the XBPM parameters is shown in Tab. 6.5 and the working principle is illustrated in Fig. 6.16. Each quadrant current is amplified and converted to a voltage signal by a low noise current amplifier and then digitized by a gated analog-to-digital converter (ADC) to average the signal over the preset gating time.

6. Synchronization and Stability

The normalized beam position can then be calculated by

$$X = \frac{(I_B + I_D) - (I_A + I_C)}{\sum I}, \quad (6.8)$$

$$Y = \frac{(I_A + I_B) - (I_C + I_D)}{\sum I}. \quad (6.9)$$

For an active beamline operation a Python⁸⁸ based software as well as a user-friendly interface based on the PyQt package has been written. The calculated normalized X-ray beam positions are further utilized by a control algorithm as described in Sec. 6.1 to calculate the error signal and the respective actions. Deviations in the horizontal direction are balanced by the rotation angle of the second horizontal mirror (see Sec. 4.2.3), while the pitch 2 angle of the monochromator (see Sec. 4.2.2) is utilized to regulate the vertical position.

At first a resolution limit of $R \approx 1.75 \mu\text{m}$ was characterized. Special care has to be taken to account for the backlash of the stepper motor, which is used to set the pitch 2 angle. This motor is located in vacuum and a constant feedback control would induce too much heat, thus increasing the risk of damaging the motor. Therefore, an integral limit is set within the respective part of the control algorithm, decreasing the possibility of integral windups and overshooting. Furthermore, a different *deadband threshold* for each beam operation, defined by the bending of the X-ray mirrors (see Chap. 4.2.3), is chosen to address the changing sensitivity of the XBPM to different X-ray beam sizes. The varying sensitivity to different X-ray beam sizes is the direct consequence of the gap sizes of the quadrant detector. Thereby, a stronger focused X-ray beam will less over-illuminate the gaps than a non-focused X-ray beam, especially in the vertical direction, which leads to an increased sensitivity to intensity variations.

The deadband supports avoiding a reverse of the feedback direction as well. An additional photon flux threshold guarantees the safety to prevent any feedback operation

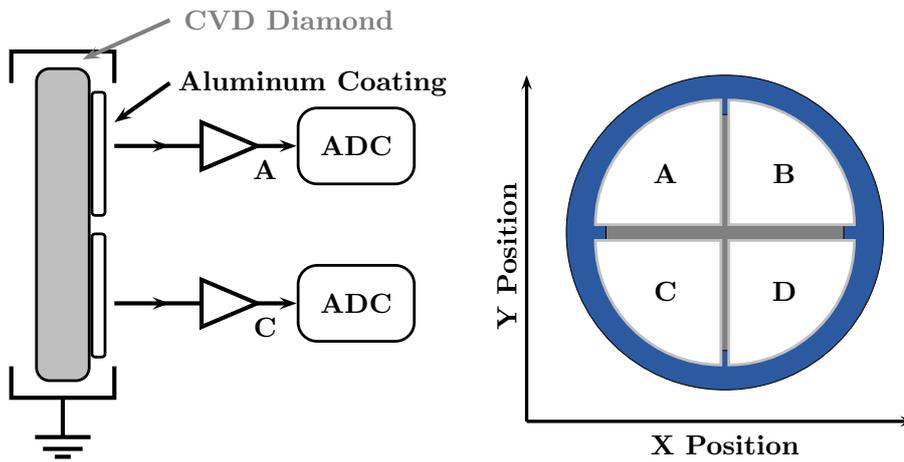


Figure 6.16.: Working principle (side view) and geometry (front view) of a quadrant detector with labeled areas. To determine the beam position, the current of each quadrant has to be measured. For a CVD diamond foil current amplifiers sensitive to a few nA have to be used. Figure is based on reference⁸⁷.

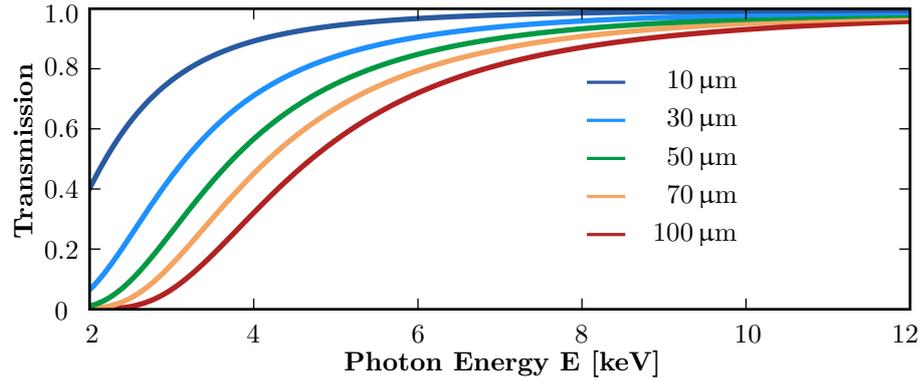


Figure 6.17.: Calculated X-ray transmission as a function of energy for different diamond foil thicknesses. For any experiment operating at energies below an X-ray energy of 8 keV it is recommended to use thin diamond foils as active layer for XBPMs. The transmission was calculated using the software XOP³⁵.

and thus a movement of an optical element if the measured photon flux is below the threshold.

In the following section a detailed investigation of the X-ray beam stability at beamline P11 is presented.

6.5.1. Spatial X-ray Beam Stability at Beamline P11

The beamline P11 is operated with bending mirrors to focus the X-ray beam. The mirrors are continuously bendable and allow beam sizes from $(635 \times 425) \mu\text{m}$ rms down to $(16 \times 96) \mu\text{m}$ rms ($v \times h$)^{58,60}. However, the bender operation can be classified into three different regimes for the experiments: the relaxed beam, the semi-focused beam and the focused beam.

In order to characterize the frequency of noise contributions, both X-ray monitors were sampled by 3.25 kHz at 8 keV to measure the current and to classify noise contributions. First of all, the XBPM directly behind the monochromator in the optic hutch is subject for investigation. The calculated currents for the horizontal and vertical position and the related amplitude spectra are shown in Fig. 6.18. By comparing the amplitude spectrum with the spectrum from the measured current, both vertical and horizontal, it can be identified that only minor (relative) noise contributions are present.

In case of the horizontal direction the largest contribution originates from a spike at 33 Hz followed by slightly less features at 46 Hz and 48 Hz. Regarding the vertical position the same frequencies can be also identified as noise contributions at small amplitudes in the amplitude spectrum. The same measurement was repeated for the XBPM utilized for feedback control in the experimental hutch. The outcome is shown in Fig. 6.19. By comparing these spectra with the measured spectra from the XBPM directly after the monochromator, quantitative and also qualitative conclusions can be drawn. The relative amount of noise appearing in the horizontal direction is basically constant, while in the vertical direction a significant increase of amplitude can be

6. Synchronization and Stability

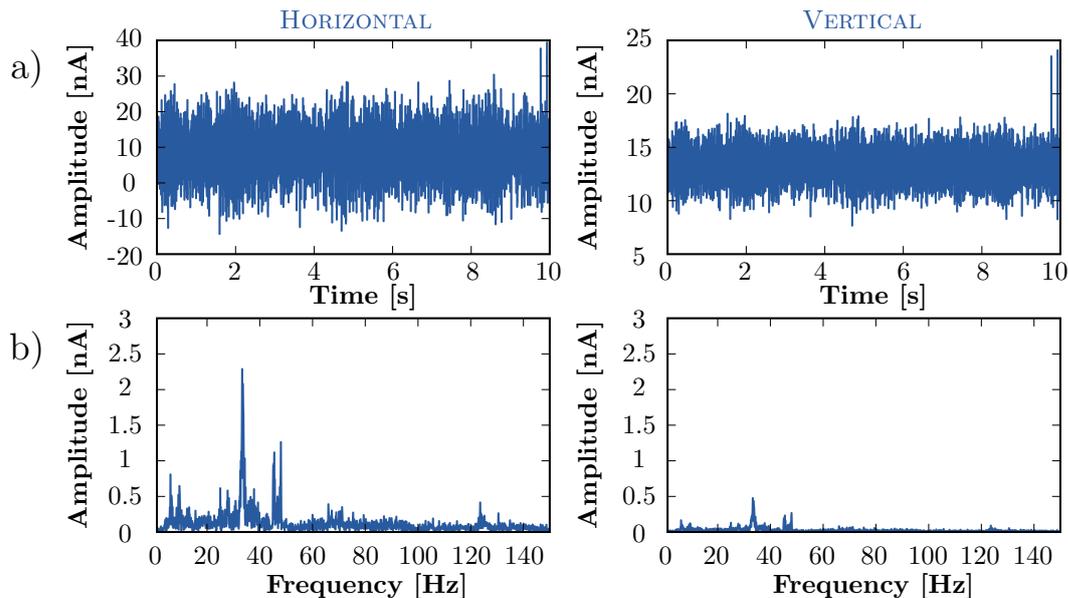


Figure 6.18.: **a)**: Measured current of the XBPM behind the monochromator sampled by 3.25 kHz at an X-ray energy of 8 keV for the respective direction. **b)**: Calculated amplitude spectrum showing noise at frequencies of 33 Hz, 46 Hz and 48 Hz.

identified, leading to a strong evidence that noise contributions have their origin in angular vibrations of the two crystals inside the monochromator chamber. The noise feature at 46 Hz exhibits now a relative amount of amplitude of roughly thirty to fifty percent. In addition, an harmonic vibration at 92 Hz appears, indicating that the noise contribution at 46 Hz is of main interest.

The monochromator stability is still subject of investigation, however, for now the noise contributions in the X-ray beam position are most likely related to the crystal vibrations inside the monochromator chamber, which in turn are excited by the flowing nitrogen inside the rotary feed-through due to the liquid nitrogen pump.

In conclusion, it is shown that large noise contributions occur at rather high frequencies. This has a great impact for experiments, which strongly rely on stability, e.g. any experiment where small or dilute samples are used. To complete the first series of measurements, the spectrogram showing the power spectral density over time is shown in Fig. 6.20. It can be seen that the described noise contributions are constant over time and not linked to any event.

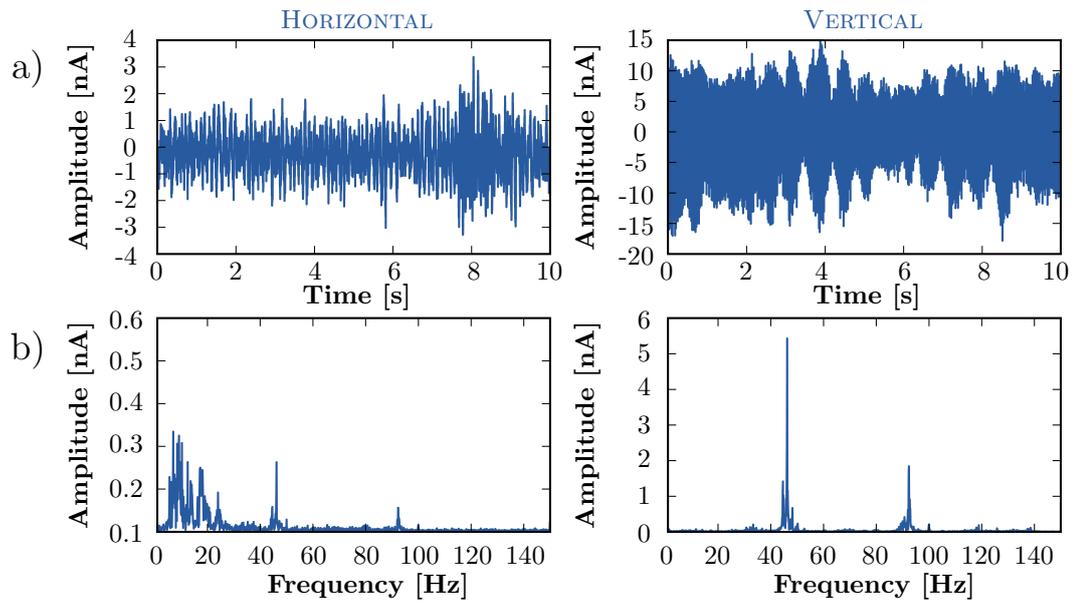


Figure 6.19.: **a)**: Measured current of the XBPM inside the intermediate focus chamber sampled with 3.25 kHz at an X-ray energy of 8 keV for the respective direction. **b)**: Calculated amplitude spectrum showing noise contributions at frequencies of 33 Hz, 46 Hz and 48 Hz.

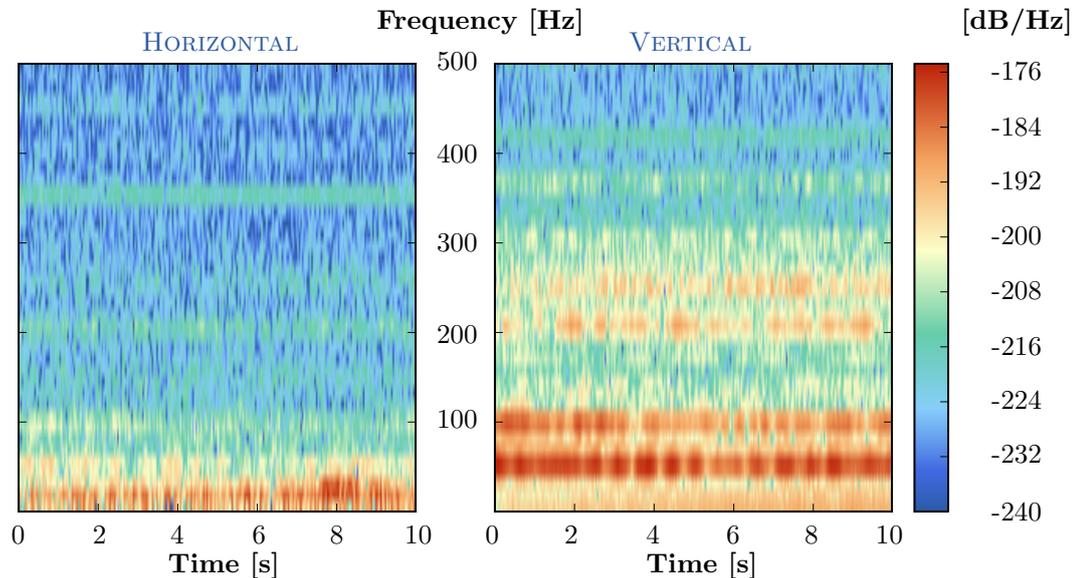


Figure 6.20.: Calculated spectrogram from the measurement of the XBPM inside intermediate focus chamber sampled with 3.25 kHz at an X-ray energy of 8 keV.

Stability during injection - Top-Up Mode

As described in Sec.4.1.1, the PETRA III synchrotron is operated in top-up mode to maintain a constant ring current ($\sim 1\%$). For this purpose electrons are periodically injected to the weakest bunches. These injections are occurring roughly every minute⁵³ and have an influence on the X-ray beam stability. Therefore, an injection was visualized with an XBPM, which is shown in Fig.6.21 and Fig.6.22.

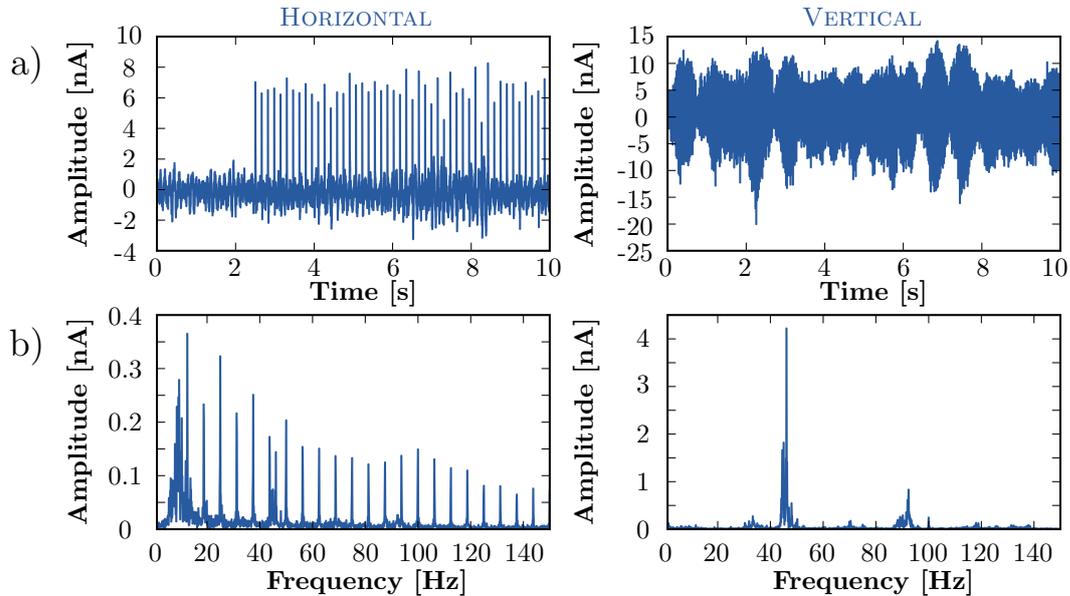


Figure 6.21.: **a)**: Measured current of the XBPM inside the intermediate focus chamber sampled with 3.25 kHz at an X-ray energy of 8 keV during top-up injection for the respective direction. Noticeable are spikes appearing in the horizontal direction. **b)**: Calculated amplitude spectrum in which the top-up injection is visualized by a broad series of frequencies in the horizontal amplitude spectrum.

The injection can be fairly seen in the spectrogram of the horizontal X-ray beam position, where after two seconds of measurement time oscillations occur. These oscillations govern a broad spectrum of frequencies and originate from the orbit adjustment inside the storage ring. Hence, this strongly affects measurement noise and is one reason for a deadband setting within feedback control.

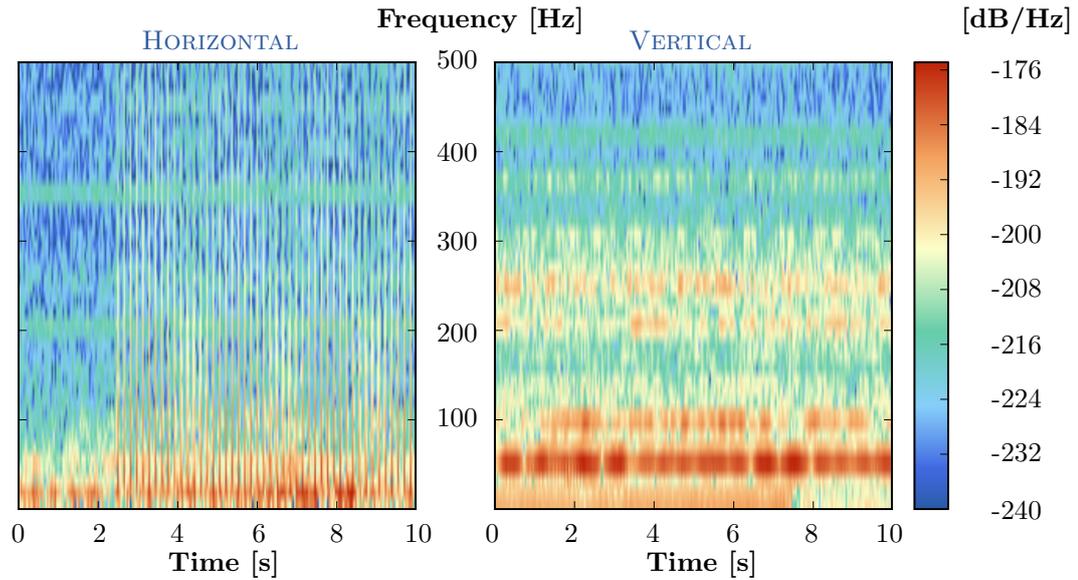


Figure 6.22.: Spectrogram showing a top-up injection, which is noticeable as lines in the horizontal direction after two seconds measurement time. Measurement was performed at an X-ray energy of 8 keV with a sample rate of 3.25 kHz.

Relaxed Beam

The sensitivity of the XBPM varies with different beam sizes and only accounts relative changes in the X-ray beam position. The absolute spatial deviation is roughly $1\ \mu\text{rad}$ rms, which will be shown during the following sections. With a view to energy scanning experiments, this section presents and analyzes the major operations, in which the beam stability has been measured for at least several hours with 2 Hz bandwidth.

At first, the completely relaxed bender setting with no focusing is introduced. For a general view about the beam stability, the beam position during an energy step scan of the monochromator and a subsequent fixed-energy operation was measured. Within this bender setting, the deadband threshold of the control algorithm can be comfortably set to $\approx 5.25\ \mu\text{m}$. The control algorithm was configured with high proportional gains and moderate integral and derivative gains tracking a feedback policy to shift the beam into the deadband region at short rise times.

The measurement is illustrated in Fig. 6.23, in which the different operation modes of the monochromator, step scan and fixed energy, can be fairly easy distinguished by eye. Approaching for a new X-ray energy most likely leads to a forth- and back flap of the second crystal at the beginning of the crystal movement, which can be identified as spikes in the measured X-ray beam position, especially in the vertical direction. In most cases the original vertical X-ray beam position cannot be recovered and has to be corrected by the pitch 2 angle slightly shifting the X-ray beam position back inside the preset deadband region, while the horizontal position remains relatively stable.

In strong contrast to the step scan operation is the monochromator behavior at a fixed X-ray energy. The X-ray beam most likely drifts towards the upper deadband threshold and once it starts leaving the deadband region, it gets constantly pushed

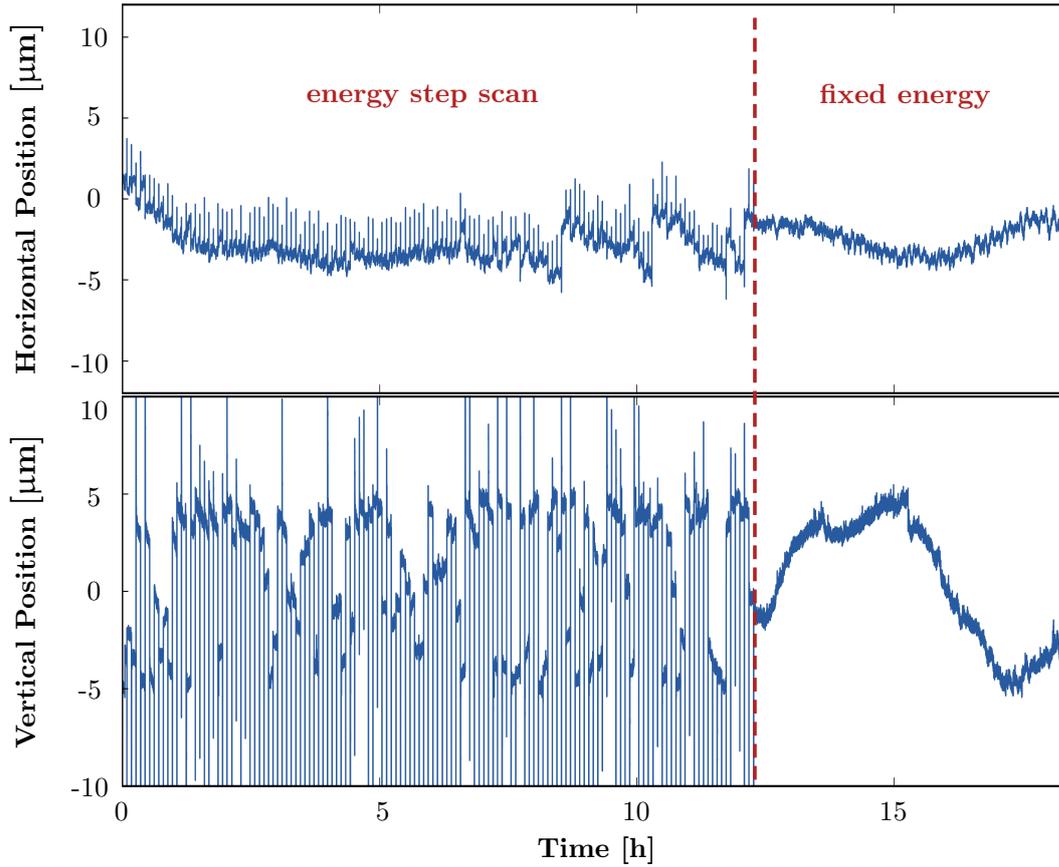


Figure 6.23.: X-ray beam position measured with relaxed mirror bender settings during an energy step scan and subsequent fixed energy operation with a deadband threshold around $5.25 \mu\text{m}$. **Top:** Horizontal beam position; **Bottom:** Vertical beam position.

towards the opposite direction resulting in a reversed drift. Therefore, the natural drift of the X-ray beam is towards upper direction resulting from a slightly tilting of the second crystal. A 2D histogram of the X-ray beam position is shown in Fig. 6.24, where the main X-ray beam position is directly beneath the upper deadband threshold. Moreover, a vertical drift of ~ 200 nrad per hour during an active feedback control can be determined after several hours of beam exposure on the crystals.

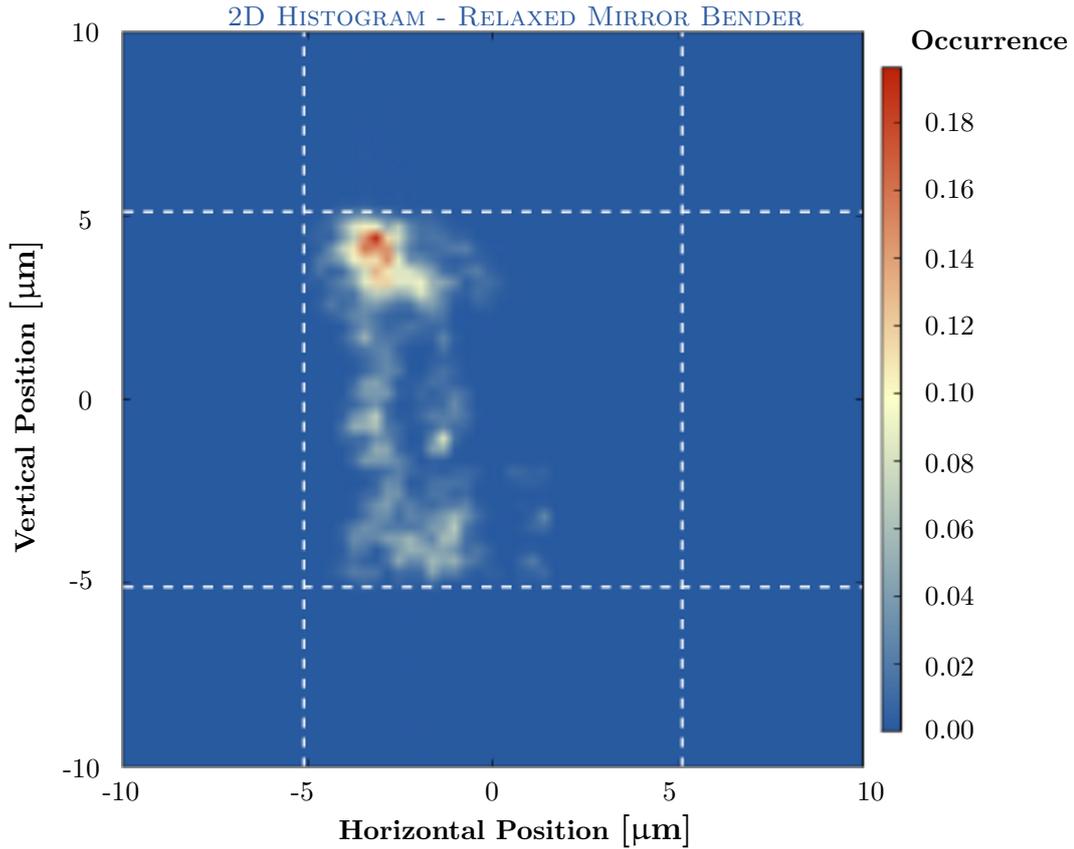


Figure 6.24.: X-ray beam stability measured with relaxed mirror benders. Dashed white lines: Deadband threshold of $\approx 5.25 \mu\text{m}$.

Semi-Focused Beam

Setting the mirror benders to an average value between the maximum adjustable curvature and no curvature leads to the next regime, the semi-focused beam.

Similar to the measurement in the relaxed mirror setting, the X-ray beam position was measured during an energy step scan of the monochromator as well as a subsequent fixed energy operation (see Fig. 6.25).

The main difference is a different feedback policy and a wider deadband threshold of $\approx 8.75 \mu\text{m}$, which was set to account for the increased measurement noise. In contrast to the relaxed bender setting policy, in which the X-ray beam position is slightly shifted back into the preset deadband region, thus maintaining a quasi-stable position beneath the threshold, it is attempted to push the X-ray beam position back to the center of the deadband region. The motivation is based on the negligence of frequently detected small X-ray beam position deviations to avoid a constant feedback control. This is achieved by either an interplay of proportional and integral actions or as lately applied, a control algorithm utilizing a proportional action at high gains supported by an average derivative contribution.

The feedback policy can also be identified in the 2D histogram shown in Fig. 6.25, in which one main X-ray beam position is basically centered inside the deadband region.

6. Synchronization and Stability

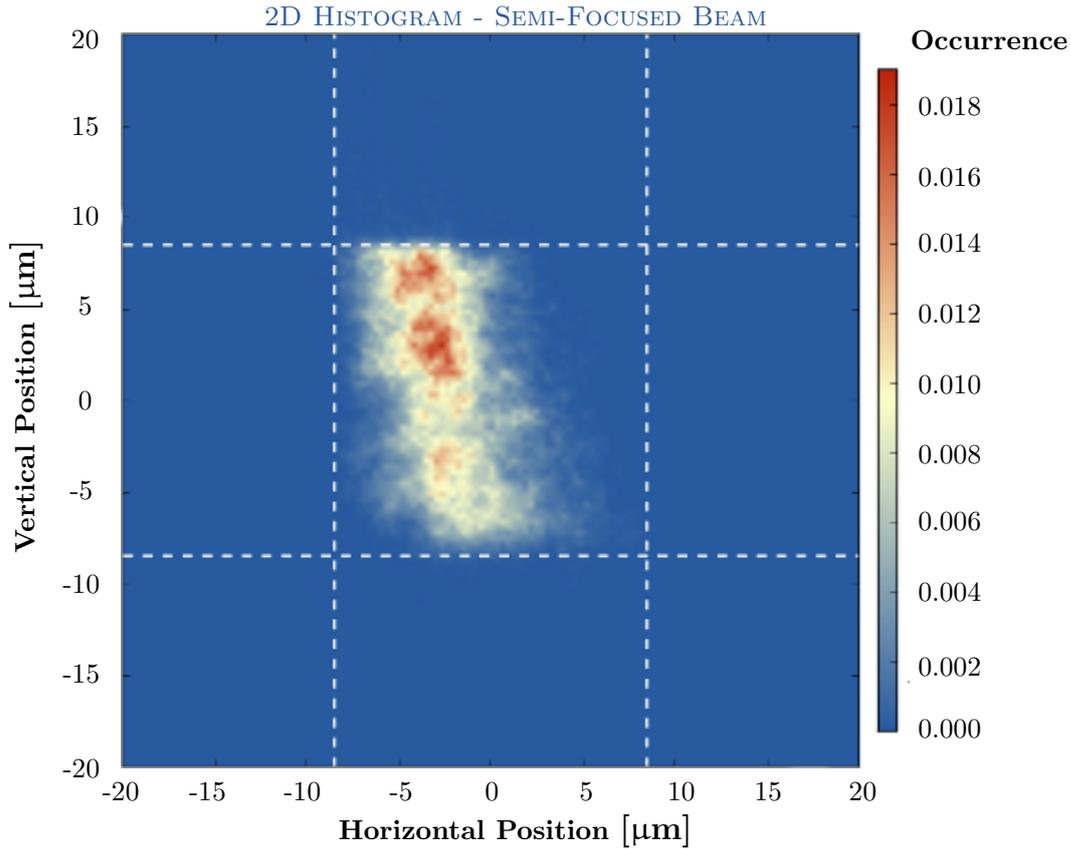


Figure 6.25.: X-ray beam stability measured with semi-bended mirrors. Dashed white lines: Deadband threshold of $\approx 8.75 \mu\text{m}$.

In addition, the natural drift direction towards the positive vertical direction can be sustained by a frequent occurrence of X-ray beam positions appearing beneath the positive deadband threshold.

Focused Beam

Setting the mirror benders in a region near the maximum adjustable curvature defines the last regime, the focused beam. To determine the spatial X-ray beam stability, the X-ray beam position was only measured during a fixed-energy operation of the monochromator. Similar to the semi-focus regime, the deadband threshold was set to $\approx 8.75 \mu\text{m}$ following the same feedback policy as previously described. The X-ray beam position histogram is shown in Fig. 6.26 and clearly illustrates a devastating spatial X-ray beam stability. No defined occurrence of the X-ray beam position can be identified, instead the X-ray beam position is widely spread throughout the deadband region. Regarding the vertical direction, even without moving the crystals inside the monochromator, a not negligible amount of X-ray beam positions can be identified out of the preset thresholds. Thereby, amplitudes of X-ray beam deviations up to and above (not shown here) $20 \mu\text{m}$ ($\approx 1 \mu\text{rad}$ rms) are visible. It is important to mention

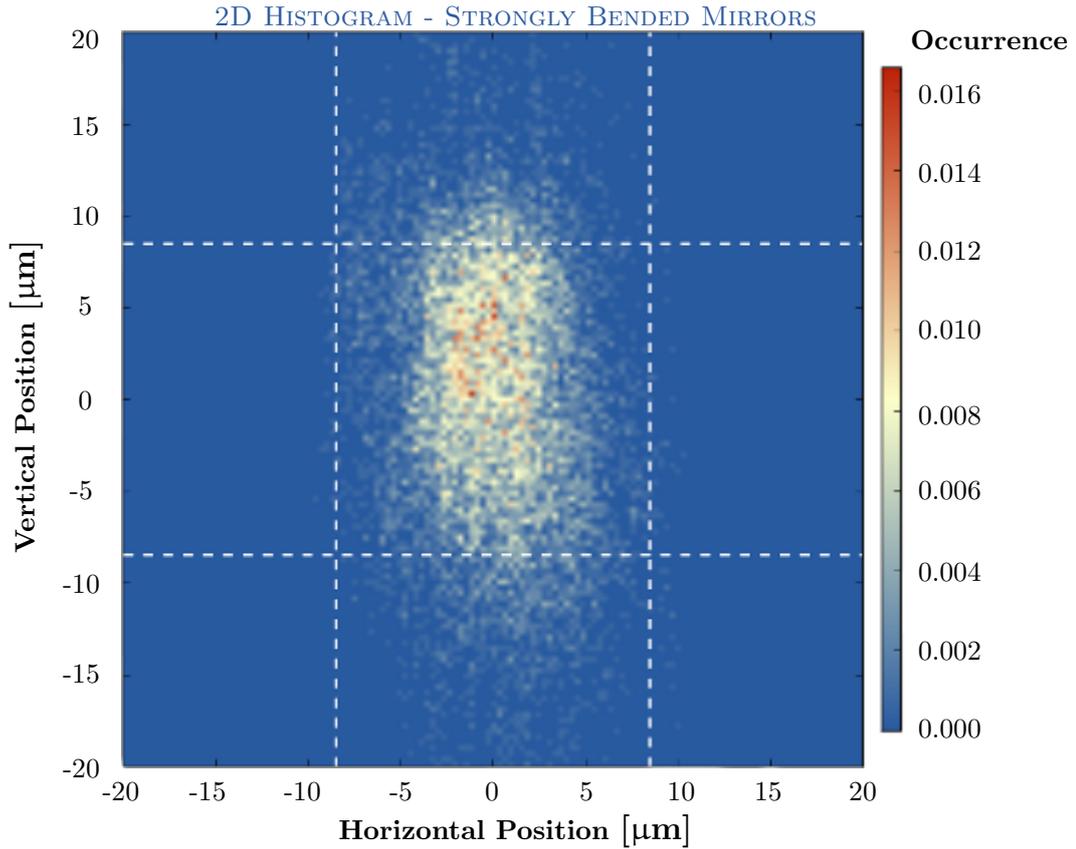


Figure 6.26.: X-ray beam stability measured with strongly bended mirrors. Dashed white lines: Deadband threshold of $\approx 8.75 \mu\text{m}$.

that these deviations were measured with a sample rate of 2 Hz only. The outcome of this spatial analysis is mainly that high focusing regimes of the X-ray beam are not suitable for experiments in which small differences between similar measurements have to be detected. The whole concept of creating a secondary source of the X-ray beam with bending mirrors inside the intermediate focus chamber, as described in Sec. 4.2.4, has to be reconsidered and will not work under the present circumstances.

6. *Synchronization and Stability*

7. Time-Resolved Pump and Probe X-ray Absorption Fine Structure Spectroscopy Experiments

7.1. Ground State XAFS	83
7.2. Excited State XAFS	85
7.2.1. Spectral Resonance Fitting and Analysis	88
7.3. Time-Resolved XAFS	94
7.3.1. Temporal Resolution - X-ray Bunch Length	95
7.3.2. Excited State Lifetime - Second-Order Decay Kinetics	97
7.4. Influence of Laser Fluence - Excitation Threshold	100

This chapter presents the - to our knowledge - first static and time-resolved XAFS studies of the green phosphorescence emitter complex Ir(ppy)₃.

In particular static and time-resolved L₃- and L₂-edge absorption spectra of iridium were measured to investigate the structural and electronic changes after photoexcitation of the metal-to-ligand charge transfer band. For this purpose, the sample was photoexcited with femtosecond laser pulses at a wavelength of 343 nm and afterwards probed with X-ray pulses at a time delay of 100 ps to obtain the transient spectrum. The excited ³MLCT state could be determined from the obtained XAFS spectra utilizing an ionic approximation. The results present a direct visualization of the metal-to-ligand charge transfer by an investigation of the ionization potential shift. The octahedral crystal field splitting 10Dq could be determined from the XAFS spectra (see Sec. 7.2.1) and used to calculate the first experimental estimate of the bond length change upon photoexcitation using an octahedral approximation. Additional time scans, in which the laser pulse is temporally shifted with respect to the X-ray pulse, were performed to characterize the temporal resolution of the experiment and to provide information on the second-order decay kinetics of the triplet state.

The measurements presented in the following were mainly obtained during a beamtime in August 2013. The author appreciates the strong support by Philip Roedig, Alexander Britz and Tadesse Assefa during measurements.

7.1. Ground State XAFS

For the present XAFS studies the sample was dissolved in dimethyl sulfoxide at a 2 mM concentration and the monochromator crystal pair was selected as Si(111), thus

7. Time-Resolved Pump and Probe X-ray Absorption Fine Structure Spectroscopy Experiments

providing an energy resolution of $\Delta E/E = 1.3 \cdot 10^{-4}$ at 12 keV. The X-ray beam size was defined by a platinum pinhole of 150 μm and the jet diameter was chosen to be 200 μm . The jet velocity was measured with 7 ± 1 m/s.

The L_3 and L_2 -edge absorption spectra of $\text{Ir}(\text{ppy})_3$ were then measured in the X-ray fluorescence yield mode at room-temperature accumulating the fluorescence yield in the single photon counting regime for $3 \cdot 10^6$ shots for each energy step. The incident number of X-ray photons per shot was estimated with $\sim 4.1 \cdot 10^5$, which results in $\sim 1.2 \cdot 10^{12}$ incident X-ray photons per data point. In each energy scan the region around the absorption edges was typically probed with fine step sizes of 0.5 eV. After the absorption edges the step size was gradually increased up to 5 eV after the first fine-structure modulation in order to obtain a sufficient energy range for edge-jump normalization. Furthermore, the sample solution was completely exchanged in order to avoid spectral changes induced by sample degradation due to radiation damage after each scanⁱ.

The ground state spectra were normalized to the absorption edge-jump $\Delta\mu_0$ with a set of spline functionsⁱ and several glitches in the spectra were removed (see App. A). The resulting spectra are shown in Fig. 7.1.

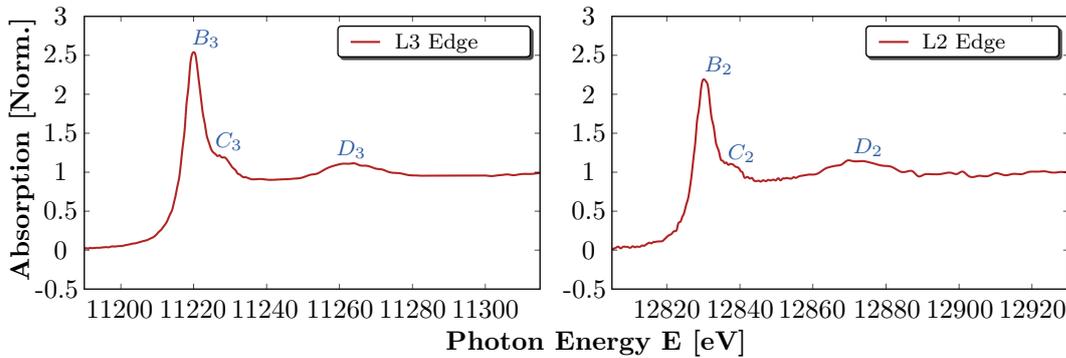


Figure 7.1.: Normalized ground state XAFS spectra of the $\text{Ir}(\text{ppy})_3$ molecule dissolved in dimethyl sulfoxide with a concentration of 2 mM.

Left: L_3 -edge spectrum in which the spectral resonances are denoted as B_3 , C_3 and D_3 .

Right: L_2 -edge spectrum. The features denoted as B_2 , C_2 and D_2 .

As described in great detail in Sec. 2.1.1, the spectral resonances in the near-edge structure region of the absorption spectra primarily arise in consequence of dipole allowed transitions of photoelectrons to empty bound states ($\Delta l = \pm 1$ and $\Delta j = \pm 1, 0$)³⁷ⁱⁱ. For the present L-edge spectroscopy the features can therefore be qualitatively assigned to transitions of excited core electrons from $2p_{3/2}$ (L_3) and $2p_{1/2}$ (L_2) orbitals to empty or partially filled s and d orbitals. In both spectra the spectral resonances are denoted

ⁱStandard experiment description. Compare to reference⁶.

ⁱThe software used for normalization of XAFS spectra is the demeter package^{95,96}.

ⁱⁱThe following description including the qualitative assignment of the photoelectron transitions and spectral resonances follows and is based on the literature^{9,37}. Several other publications, which characterize ruthenium^{93,102} or rhemium⁹⁴ complexes in L-edge experiments are available. The classified photoelectron transitions are also in reference to the literature²⁵, which describes L-edge measurements of a platinum sample.

by B, C, and D, while the subscript 3 and 2 indicates the L₃- and L₂-edge features, respectively.

The electronic structure of Ir(ppy)₃ in the ground state is characterized as a low-spin 5d⁶ configuration in which the *t*_{2g} set is completely filled with electrons while the *e*_g set is left empty (see Sec. 3.2). Therefore, the resonance B can be assigned to the absorption of excited 2p_{3/2} core electrons in 5d_{3/2} and 5d_{5/2} orbitals (*e*_g) at the L₃-edge. Furthermore, the B feature at the L₂-edge can be classified as the absorption of excited 2p_{1/2} core electrons in 5d_{3/2} (*e*_g) orbitals.

The C features, which accompany the B resonances and fairly seem to overlap with them, can be probably assigned to either the absorption of photoelectrons in higher lying 6s_{1/2} orbitals³⁷ or multiple-scattering resonances⁹. The D features, which are at sufficiently high energies above the first inflection point on the edge resonances (~45 eV), mark the first fine-structure modulations⁹.

7.2. Excited State XAFS

The L-edge spectroscopy of Ir(ppy)₃ was extended into the pump-probe configuration as described in Sec. 2.3. The liquid jet is exposed to short laser pulses at a wavelength of 343 nm to trigger the photocycle of the metal-to-ligand charge transfer described in Sec. 3.4. The photoinduced electronic and structural changes of the sample are subsequently detected by the following X-ray pulses yielding the so-called pump-probe spectrum.

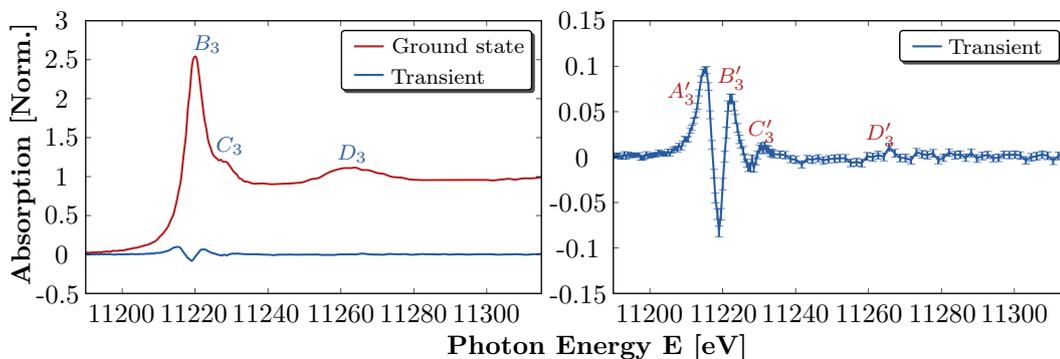


Figure 7.2.: **Left:** L₃-edge ground state XAFS spectrum of the Ir(ppy)₃ molecule (2 mM) dissolved in dimethyl sulfoxide (red curve) with the measured normalized transient difference spectrum $\Delta T(E, t)$ (blue curve). **Right:** Magnified transient difference spectrum $\Delta T(E, t)$ with denoted main features where a new transition A'_3 appears.

The transient difference spectrum $\Delta T(E, t)$ is created as the difference between the measured pump-probe spectrum and the ground state spectrum $A_{GS}(E)$. The obtained spectrum serves as a photoexcited fingerprint and can provide qualitative hints of the photoinduced changes. The transient difference spectra within this thesis were obtained by measuring the pumped and unpumped signals at time delays of 100 ps and 7.69 μ s between laser pump and X-ray probe pulse, respectively. The applied gating

scheme is described in Sec. 5.7.1. The transient spectra obtained at the L₃ and L₂-edge are shown in Fig. 7.2 and Fig. 7.3, respectively.

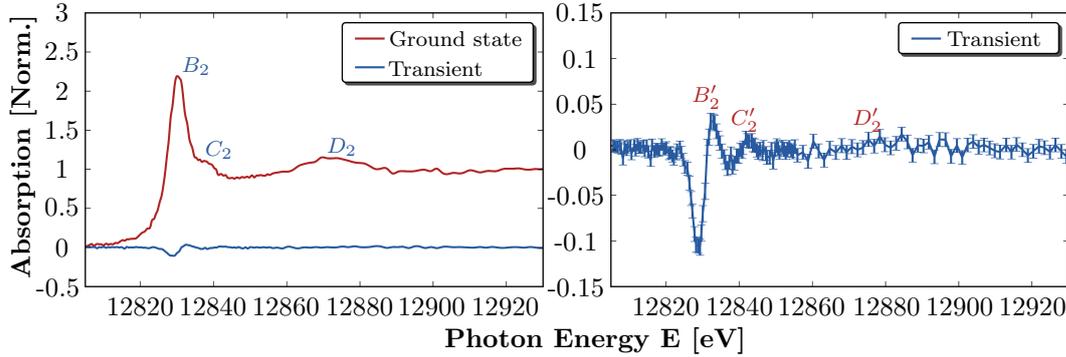


Figure 7.3.: **Left:** L₂-edge ground state XAFS spectrum of the Ir(ppy)₃ molecule (2 mM) dissolved in dimethyl sulfoxide (red curve) with the measured transient difference spectrum (blue curve). **Right:** Magnified transient difference spectrum $\Delta T(E, t)$.

The first prominent observation between the transient spectra is the appearance of an additional absorption peak at the left flank of the edge resonance in the L₃ spectrum, which is not observed in the L₂ spectrum. This additional absorption is further denoted as A' feature and reflects the absorption of photoelectrons in the photoinduced vacancy of the t_{2g} set^{9,37}.

Moreover, in both spectra the spectral resonances B and C qualitatively lose intensity around their maxima and gain intensity at their high-energy side, revealing that these spectral features experience a blue shift in energy, caused by the photoinduced temporal oxidation of the iridium atomⁱⁱⁱ. Feature D most likely experiences also a blue shift in both spectra. As described in Sec. 2.3, the measured intensities in an X-ray pump and probe configuration depend on the dynamic fraction of the excited state species. Therefore, the measured transient difference spectrum $\Delta T(E, t)$ is defined as^{9,10,33}

$$\Delta T(E, t) = f(t) \cdot (A_{\text{ES}}(E, t) - A_{\text{GS}}(E)), \quad (7.1)$$

where $f(t)$ is the photoexcitation yield characterizing the excited state fraction while $A_{\text{ES}}(E, t)$ and $A_{\text{GS}}(E)$ are the excited state spectrum and the ground state spectrum, respectively. The excited state spectrum can then be derived by

$$A_{\text{ES}}(E, t) = \frac{\Delta T(E, t)}{f(t)} + A_{\text{GS}}(E). \quad (7.2)$$

In order to obtain the excitation yield, the complex is treated in an ionic approximation at the L₃-edge. The following method was also applied in a previous work³³. Thereby, the ground state and the excited state are treated according to their - ionically approximated - electronic configuration of the metal valence orbitals (5d). In

ⁱⁱⁱCommon line of argumentation of a blue shift. Compare to reference³³. The ongoing description and determination of the excited state spectrum utilizing an ionic approximation follows now and is based on reference³³.

more detail, the photoinduced vacancy in the t_{2g} set defines the electronic structure of the excited state as a $5d^5$ configuration while the ground state is represented by a $5d^6$ configuration (see Sec. 3.4)^{iv}.

As described, the edge resonance at the L_3 -edge originates from the absorption of excited 2p core electrons in the metal valence orbitals (5d). Therefore, the integrated ground state absorption $A_{\text{GS}}^{\text{edge}}$ obtained at the edge resonance corresponds to 4/10 of the hypothetical integrated edge absorption $A_{\text{d-empty}}^{\text{edge}}$, which would arise from completely empty metal valence orbitals. In turn, the integrated edge absorption in the excited state $A_{\text{ES}}^{\text{edge}}$ is related to 5/10 of the integrated edge absorption with empty metal valence orbitals:

$$A_{\text{GS}}^{\text{edge}} = \frac{4}{10} A_{\text{d-empty}}^{\text{edge}}, \quad (7.3)$$

$$A_{\text{ES}}^{\text{edge}} = \frac{5}{10} A_{\text{d-empty}}^{\text{edge}}. \quad (7.4)$$

Inserting Eq. (7.3) in Eq. (7.4) further yields the condition of the ionic approximation³³

$$A_{\text{ES}}^{\text{edge}} = \frac{5}{4} A_{\text{GS}}^{\text{edge}}. \quad (7.5)$$

According to Eq. (7.2), the photoexcitation yield is assumed to be 13%. The reader is referred to App. E for a detailed calculation.

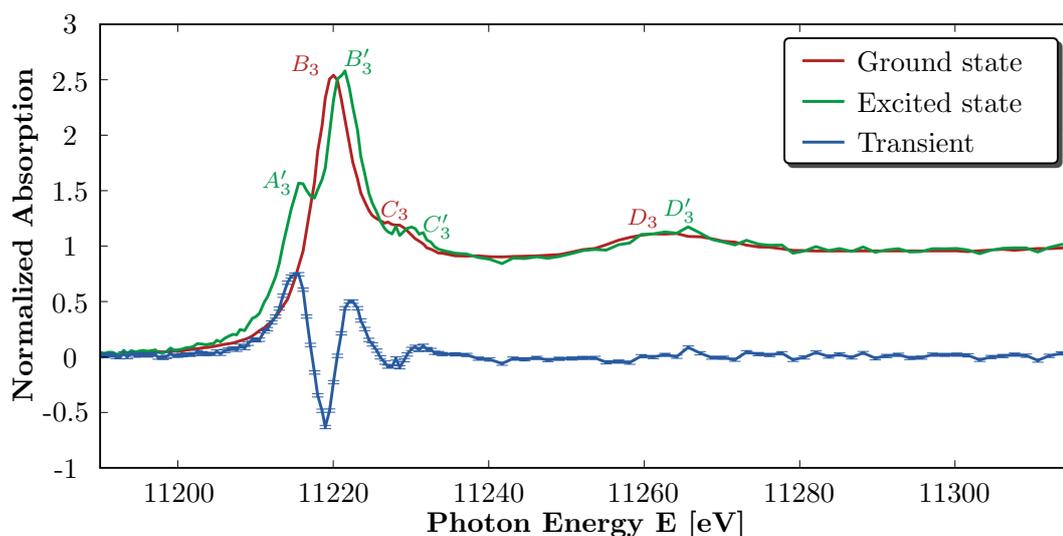


Figure 7.4.: Plotted L_3 -edge XAFS spectrum of $\text{Ir}(\text{ppy})_3$ dissolved in dimethyl sulfoxide in the ground state (red curve) and the excited state (green curve). The difference spectrum is illustrated in blue.

The obtained excited spectrum together with its corresponding ground state spectrum at the L_3 -edge is shown Fig. 7.4. The features of the excited state are further indicated with a prime. The edge resonance clearly consists of at least two spectral resonances

^{iv}Compare also to the reference⁹ where the $\text{Ru}(\text{bpy})_3$ complex is described which exhibits a similar photocycle.

and experiences a chemical shift.

The L_2 absorption spectra for the ground state and the excited state are shown in Fig. 7.5. The excited state features are again denoted with a prime. As expected, the L_2 -edge spectroscopy reveals a chemical shift as previously shown at the L_3 -edge.

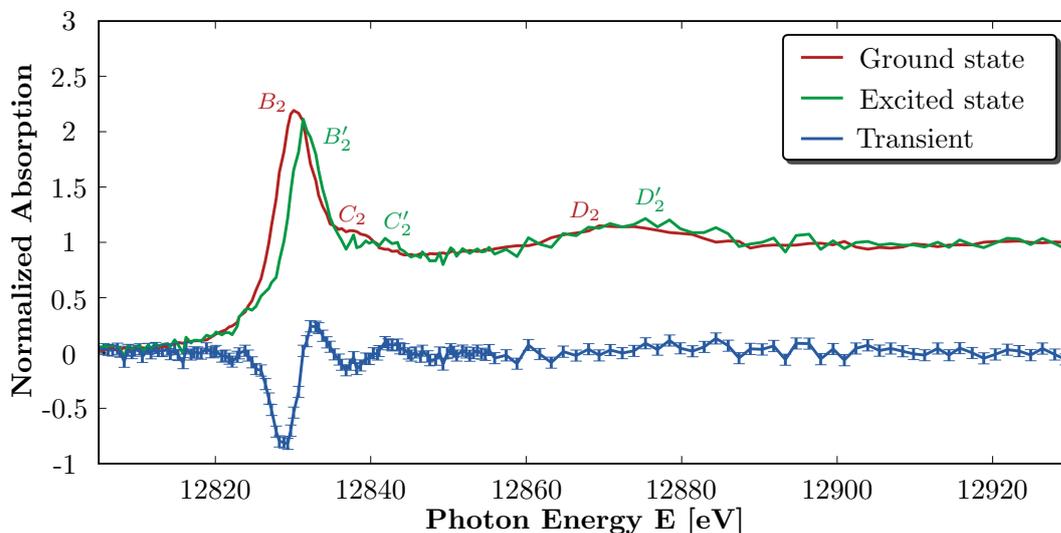


Figure 7.5.: Plotted L_2 -edge XAFS spectrum of $\text{Ir}(\text{ppy})_3$ dissolved in dimethyl sulfoxide in the ground state (red curve) and the excited state (green curve). The difference spectrum is illustrated in blue.

7.2.1. Spectral Resonance Fitting and Analysis

The transitions of photoelectrons are sensitive to spin-orbit effects and can therefore provide information on the molecular symmetry³⁷. Considering the absorption spectra of the excited triplet state at the L_3 and L_2 -edge shown in Fig. 7.4 and Fig. 7.5, respectively, it is the most prominent observation that an additional transition occurs at the L_3 -edge, which is not observed at the L_2 -edge. Although the site symmetry of the $\text{Ir}(\text{ppy})_3$ complex is primary given as a slightly distorted octahedron (C_3)²¹ and the excited triplet state further experiences an axial distortion (C_1)²¹, the additional transition, which is only occurring at the L_3 -edge in the excited state, can be explained with an octahedral symmetry.

The transition of excited core electrons from $2p_{3/2}$ and $2p_{1/2}$ orbitals to orbitals of d symmetry in an octahedral complex are shown in Fig. 7.6. Additionally, spin-orbit effects are included, which further split the t_{2g} set. In an octahedral symmetry the photoinduced vacancy in the t_{2g} set can only be probed by excitations of core electrons from $2p_{3/2}$ orbitals³⁷, which leads us to assume that the imposed distortions on the octahedral symmetry are of minor relevance. In fact, the magnitudes of the crystal field splittings are rather large, as will be shown in the analysis. Therefore, $\text{Ir}(\text{ppy})_3$ is treated as a *pseudo-octahedral*^v complex in the following.

^vThe reference¹⁰² uses the notation of a pseudo-octahedral environment.

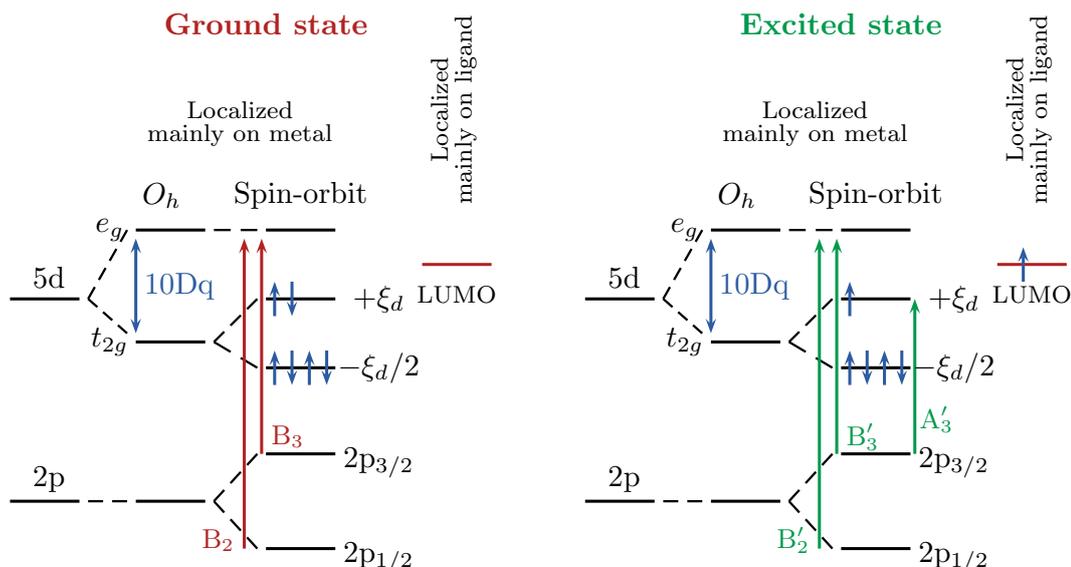


Figure 7.6.: Illustrated transitions of photoelectrons between 2p and 5d orbitals in an octahedral symmetry. The spin-orbit interaction ξ_d is included and further splits the t_{2g} set. Figure is redrawn and based on reference⁵¹.

In order to perform a quantitative analysis the energy positions of the spectral resonances are determined in the following. A quantitative analysis is for example also illustrated in reference⁹ or in a previous work³³, where the spectral resonances are characterized by so-called Voigt profiles which describe the convolution of a Gaussian and a Lorentzian function^{90,91}. The Lorentzian profiles consider the lifetime broadening while a Gaussian shaped energy resolution is assumed to account for the monochromator broadening.

In the following analysis both the core-hole lifetime and Gaussian broadening are most likely fixed to their expected magnitudes. The expected Gaussian widths (FWHM) are ≈ 1.45 eV and 1.65 eV for the L_3 and L_2 -edge, respectively. Furthermore, the core-hole lifetime of iridium for the L_3 -edge is 5.25 eV and for the L_2 -edge 5.7 eV⁹².

The ionization steps (IP) are further described by a cumulative distribution function as step function whose width is fixed to the convoluted magnitude of the core-hole lifetime and the Gaussian broadening.

The spectra including fitted resonances and absorption edges are shown in Fig. 7.8 (L_3) and Fig. 7.10 (L_2). Furthermore, the fit results of the L_3 -edge and L_2 -edge spectroscopy are summarized in Tab. 7.1.

Firstly, the L_3 -edge spectra are examined in more detail. Apparently, for both the ground and excited state the B resonances can not be described with a single Voigt profile. The Lorentzian of the B_3 resonance in the ground state is slightly larger than the literature value, indicating that there might be additional transitions involved^{vi}. The transition A'_3 occurring in the excited state spectrum at the L_3 -edge reflects the

^{vi}This is for example described and visualized in reference⁹ in case of the Ru(bpy) complex on the basis of multiplet^{104,105} calculations to simulate XAFS spectra.

Table 7.1.: Determined energy positions and Lorentzian widths (FWHM) of the spectral resonances. The Gaussian broadening by the monochromator is fixed to the theoretical bandwidth of ≈ 1.45 eV and 1.65 eV (FWHM) for the L_3 and L_2 -edge, respectively. The uncertainties are estimated to 0.1 eV for each resonance or step function position at the L_3 -edge. The uncertainties at the L_2 -edge are 0.2 eV due to the decreased S/N ratio caused by the relative smaller X-ray fluorescence yield. Table structure is adapted from reference³³.

	Ground state			Excited state			Shift [eV]
	F	Position [eV]	Width [eV]	F	Position [eV]	Width [eV]	
L_3	A_3	11214.36	-	A'_3	11215.54	5.25	1.18
	B_{3m}	11219.93	5.70	B'_{3m}	11221.42	5.25	1.49
	B_3	11223.72	5.25	B'_3	11225.40	5.25	1.68
	S_3	11226.65	5.25	S'_3	11228.55	5.25	1.91
	C_3	11228.71	5.25	C'_3	11230.68	5.25	1.97
L_2	B_{2m}	12830.26	5.70	B'_{2m}	12831.67	5.70	1.41
	B_2	12833.67	5.70	B'_2	12835.29	5.70	1.62
	S_2	12837.05	5.70	S'_2	12838.91	5.70	1.86
	C_2	12838.90	5.70	C'_2	12840.87	5.70	1.97

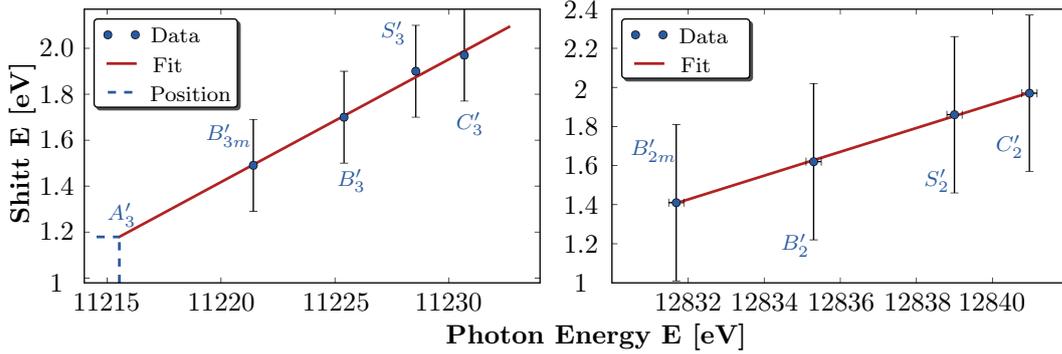


Figure 7.7.: Plotted excited state resonances together with their experienced shift upon photoexcitation. The linear regression line at the L_3 -edge is used to extrapolate the shift of resonance A'_3 in the excited state.

absorption of photoelectrons in the vacancy of the t_{2g} set and is therefore directly linked to the t_{2g} and e_g manifold (see Fig. 7.6)^{9,37,102}. Hence, the energy difference ΔE between the feature A'_3 and the main position of the B'_3 resonance provides information on the crystal field splitting $10Dq$ ^{3,9,37,102}. Regarding Fig. 7.6 and assuming a mainly octahedral environment the relationship³⁷

$$\Delta E = 10Dq - \xi_d, \quad (7.6)$$

where ξ_d denotes the spin-orbit interaction, is given. The spin-orbit coupling interaction was reported as 0.55 eV in reference²¹. The fitted ΔE of 5.88 ± 0.2 eV and the spin-orbit coupling constant provide a crystal field splitting $10Dq$ of 6.43 ± 0.20 eV in the excited state with Eq. (7.6). Since the A feature is not appearing in the ground

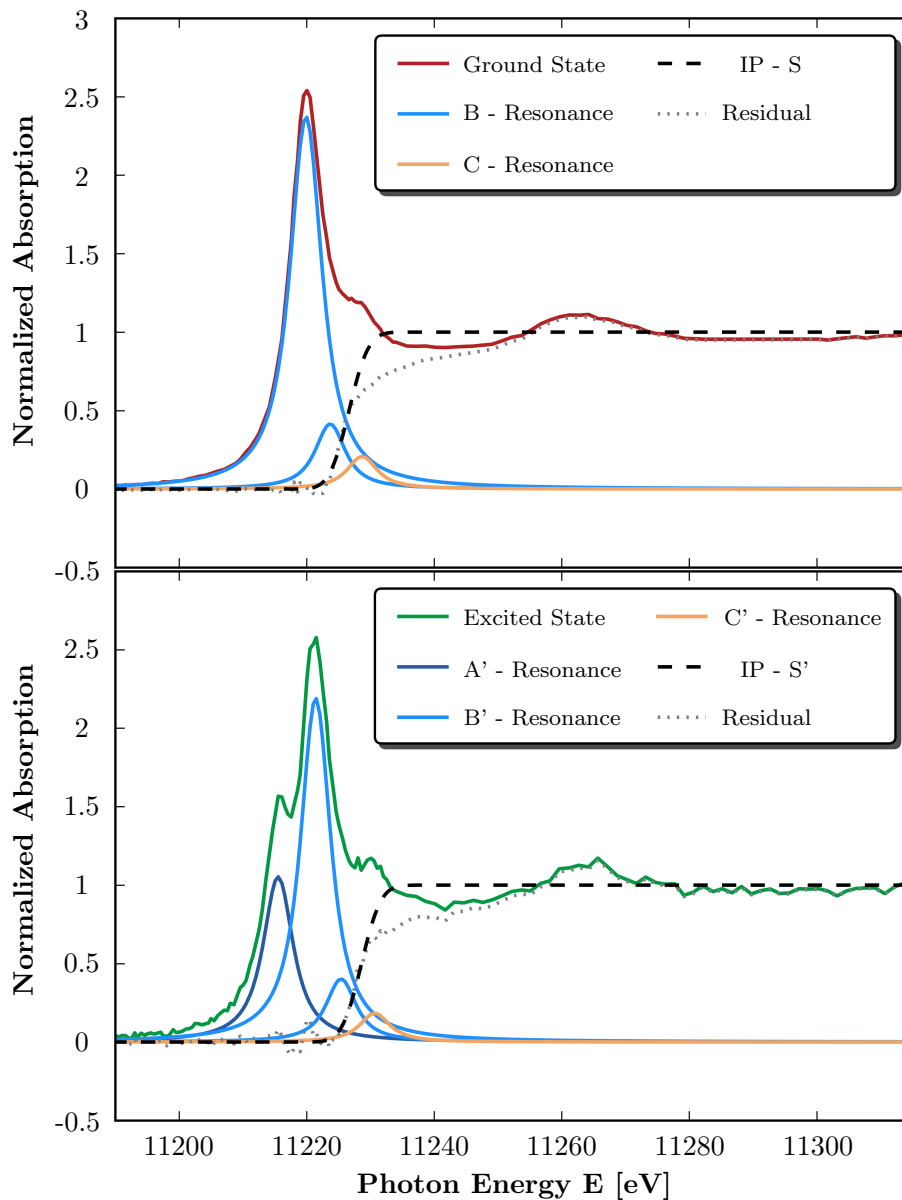


Figure 7.8.: L_3 -edge spectra of $\text{Ir}(\text{ppy})_3$ with fitted resonances. **Top:** Ground state spectrum. **Bottom:** Excited state spectrum.

state, the position can be extrapolated. Therefore, the positions of the excited state features are plotted together with their experienced shift upon photoexcitation. The outcome is shown in Fig. 7.7 and illustrates a graduate shift of the resonance positions to higher energies. A least-squares method is used to fit a linear regression and determines a shift of 1.18 ± 0.27 eV for the A'_3 feature in the excited state. Considering now the virtual A_3 resonance position yields an energy difference ΔE of 5.57 ± 0.37 eV in the ground state, which translates to a crystal field splitting $10Dq$ of 6.12 ± 0.37 eV with Eq. (7.6).

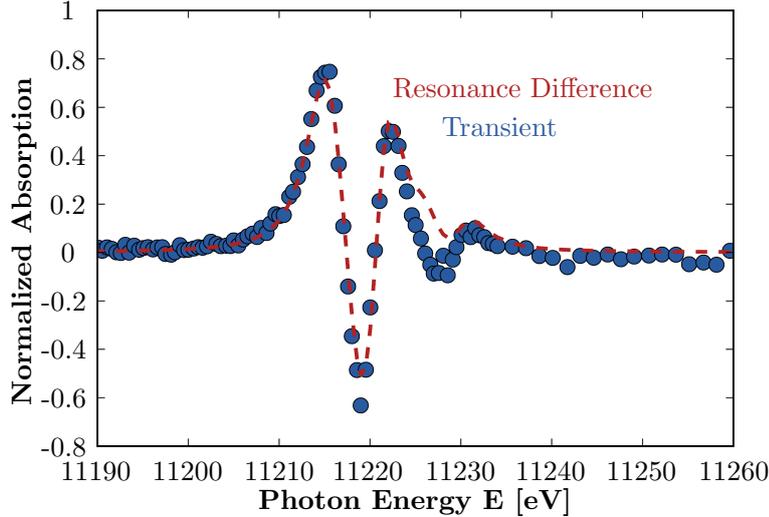


Figure 7.9.: L_3 -edge transient difference spectrum (blue) together with the difference of the composed fitted spectral resonances of excited state and ground state (red).

The quality of the spectral resonance fitting procedure is shown in Fig. 7.9^{vii}. The difference of the composed spectral resonances between excited state and ground state reflects the main features of the transient difference spectrum very nicely. The chemical shift of the edge resonance is fairly well reproduced, which sustains the characterization of the crystal field splitting in the excited state. However, the blue shift of the resonance C was very difficult to reconstruct, indicating a more complex spectral background than single Voigt profile fitting. Furthermore, a kind of experimental feature in the transient, occurring as sharp needles in the blue shift of the C resonance, disturbs the fitting. These modulations are considerably smaller than the core-hole lifetime and have been measured and reproduced several times. The origin remains unclear. As mentioned in Sec. 3.2, the crystal field splitting $10Dq$ in an octahedral complex is inversely proportional to the fifth power of the bond length. Therefore, the change in the octahedral crystal field splitting $10Dq$ can be utilized to derive a bond length change of the first coordination shell^{9,103}:

$$\frac{10Dq^{\text{ES}}}{10Dq^{\text{GS}}} = \left(\frac{R_{1S}^{\text{GS}}}{R_{1S}^{\text{ES}}} \right)^5, \quad (7.7)$$

where R_{1S}^{GS} and R_{1S}^{ES} represent the average bond length of the nearest neighbors for the ground and excited state, respectively. The structural change after 100 ps of photoexcitation can thus be calculated by⁹

$$\Delta R_{1S} = R_{1S}^{\text{GS}} \left[\left(\frac{10Dq^{\text{GS}}}{10Dq^{\text{ES}}} \right)^{1/5} - 1 \right]. \quad (7.8)$$

Inserting the average Ir-N and Ir-C bond length of $R_{1S}^{\text{GS}} = 2.063 \text{ \AA}$ ¹⁸ yields a structural change of $\Delta R_{1S} = -0.020 \pm 0.027 \text{ \AA}$. In conclusion, the bond length of the first

^{vii}Inspired by the literature^{3,9}.

coordination shell decreases by $\approx 1\%$, which can be identified by the slightly larger octahedral crystal field splitting $10Dq$ in the excited triplet state (see Sec. 3.2). The bond length uncertainty is the direct consequence of the determined conservative error of the Voigt-profile fitting. Considering only the half of the estimated error of 0.1 eV for the L_3 -edge resonances, the uncertainty of the bond length will further decrease to 0.013 Å. Hence, the determined bond length change can be considered as an indicator of a decreasing bond length of the first coordination shell in the excited state.

Theoretical investigations of the lowest triplet state reported an average Ir-N and Ir-C bond length contraction by $\approx 0.43\%$ ¹⁷. Since neither the complex is purely octahedral nor are theoretical calculations typically matching precisely the ground state structures, the now determined bond length change of the first coordination shell in the triplet state represents a fairly nice agreement.

The measured crystal field splittings of ~ 6.1 eV and 6.4 eV are rather large. Comparing these field splittings to the ones of the Ru(bpy) complex, which are most likely around ≈ 3.8 eV³⁷, the imposed splitting for the iridium complex should be increased by 30-40% (see Sec. 3.2) while treating the ligands equal. Hence, the expected magnitude of the field splittings $10Dq$ would be around 5.2 eV. Considering further the higher oxidation state of the iridium complex and the spectrochemical series shown in App. F, which characterizes the $(ppy)^-$ anion as a stronger ligand than bpy, the now determined crystal field splittings of Ir(ppy)₃ seem fairly reasonable.

The determined position of the ionization potential blue-shifts by 1.9 ± 0.1 eV in the excited state and reflects the metal-to-ligand charge transfer character since the removal of electron density from the metal valence orbitals leads to stronger bound core electrons⁹. This ionization potential shift agrees well with the shift reported⁹ for the Ru(bpy)₃ complex upon photoexcitation (1.8 eV).

Feature C lies at ≈ 2.1 eV above the ionization potential in both ground and excited state. Hence, in comparison to the literature^{9,102}, the C features are most likely classified as multiple-scattering resonances.

Unfortunately, the signal-to-noise decreases dramatically after the C features, therefore no scientific sustainable energy position could be obtained for the D features in the excited state. Nevertheless, these resonances most likely blue shift with respect to the determined ionization potential (IP), which sustains the decrease of bond length of the first coordination shell in the triplet state^{viii}.

A detailed analysis of the L_2 -edge spectroscopy reveals identical qualitative and quantitative results. Both the ground and excited state B resonances cannot not be described with a single Voigt profile. The resonances are shifted gradually and the ionization potential shift is similar to the one obtained at the L_3 -edge.

^{viii}This line of argumentation is illustrated in the literature⁹ on the basis of reference⁹⁷.

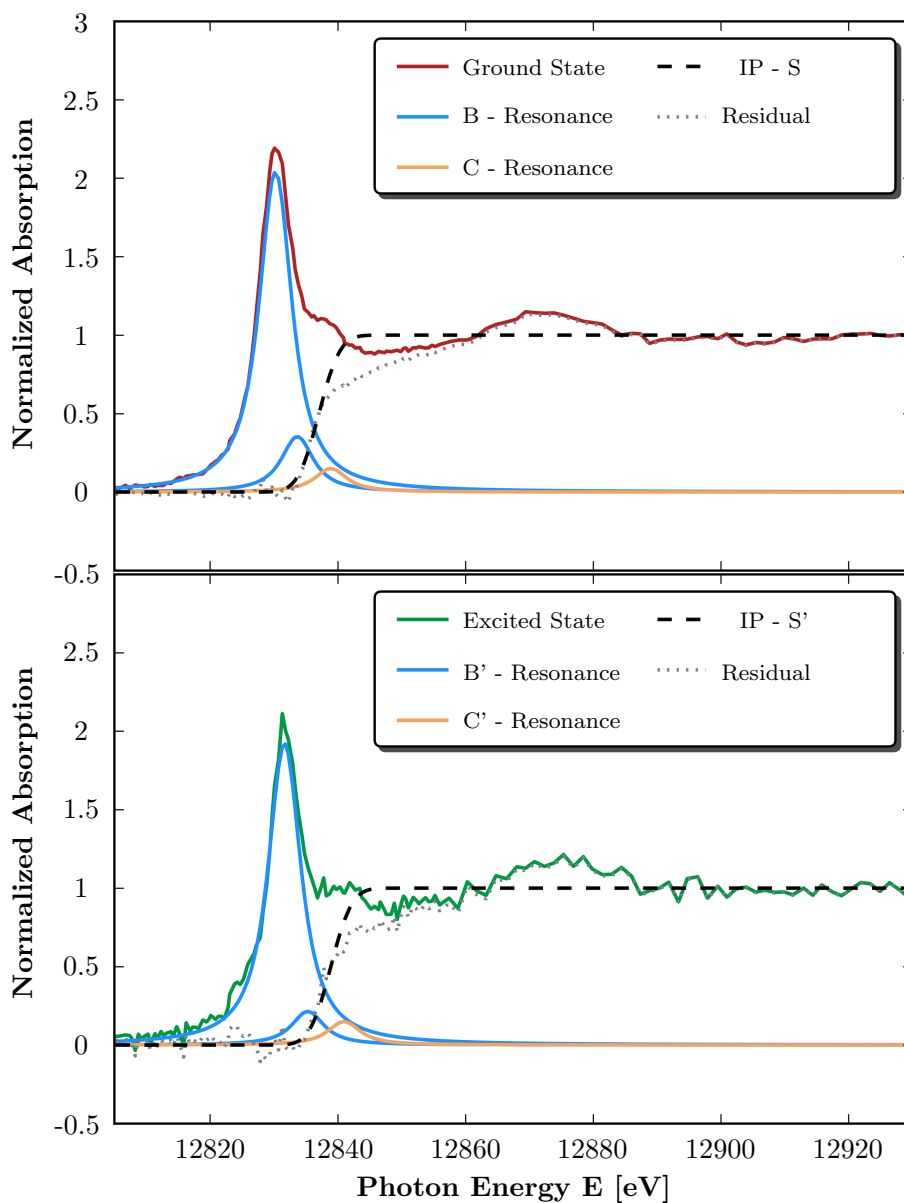


Figure 7.10.: L_2 -edge spectra of $\text{Ir}(\text{ppy})_3$ with fitted resonances. **Top**: Ground state spectrum. **Bottom**: Excited state spectrum.

7.3. Time-Resolved XAFS

This section describes *time scans* where the laser pump pulse is temporally shifted with respect to the X-ray pulse. Time scans were performed to characterize the X-ray bunch length in 40 bunch mode and to investigate the excited state decay kinetics of $\text{Ir}(\text{ppy})_3$ dissolved in dimethyl sulfoxide.

7.3.1. Temporal Resolution - X-ray Bunch Length

Time-resolved X-ray absorption spectroscopy can be utilized to characterize the X-ray bunch length by measuring the temporal evolution of the transient signal for a fixed X-ray energy. This is for example described in reference⁴⁵ in case of a setup at the ALS^{ix} or in a previous work⁷ where the temporal shape of the X-ray was measured together with Moritz Schlie for the first time at PETRA III utilizing a pump-probe signal. Within this thesis, the temporal resolution was measured during two beamtimes in May 2013 and August 2013 from a Ir(ppy)₃ sample to provide further information on the X-ray bunch length and to sustain the previously determined magnitude of 38.22 ± 2.98 ps (rms) at PETRA III.

The temporal resolution of the experiment was characterized by measuring the evolution of the transient signal ΔT as a function of the time delay t between laser and X-ray pulse at 11215 eV near feature A₃' (L₃-edge), as it governs the energy region with the highest signal-to-noise ratio due to the maximum relative change in absorption. Each data point (pumped and unpumped signal) was taken consecutively four times for $1.3 \cdot 10^6$ shots to obtain an estimate of the standard deviation.

For this measurements the synchronized laser pulse was shifted temporally with picosecond steps by the embedded synthesizer in the phase-locked loop. This measurement could be done from a Ir(ppy)₃ sample since the formation of the excited triplet state takes place in the femtosecond time region and is therefore considerably faster than the X-ray bunch length.

The analysis and description follow now quite similar reference⁷ and are further based on reference⁴⁵. The measurement results and analysis from the two beamtimes are shown in Fig. 7.11. It can be identified that the transient signal ΔT is equal to zero for X-ray pulses which arrive at the sample before the laser pulses. The transient signal then starts to evolve during the temporal convolution of laser and X-ray beam. More specific, the time delay at which both pulses are ideally overlapping yields half of the maximum signal and marks the zero time delay, while the optimum signal in turn depends on the temporal resolution of the experiment^x.

Assuming Gaussian shaped pulses and a Gaussian shaped synchronization contribution, the convolution is given by⁷

$$f_{\text{Total}}(t) = f_{\text{X-ray}}(t) * f_{\text{laser}}(t) * f_{\text{sync}}(t), \quad (7.9)$$

where $f_{\text{X-ray}}(t)$ is the temporal shape of the X-ray, $f_{\text{laser}}(t)$ the temporal shape of the laser and $f_{\text{sync}}(t)$ is the contribution of the synchronization unit. The convolution of independent Gaussians also yields a Gaussian, thus the standard deviation and temporal resolution can be obtained by⁷:

$$\sigma_{\text{Total}} = \sqrt{\sigma_{\text{X-ray}}^2 + \sigma_{\text{laser}}^2 + \sigma_{\text{sync}}^2}. \quad (7.10)$$

Therefore, each curve is fitted with a cumulative distribution function, whose standard deviation represents σ_{Total} . The temporal resolutions obtained from the two beamtimes

^{ix}ALS stands for the Advanced Light Source at Lawrence Berkeley National Laboratories, California.

^xCompare also to reference⁴⁵.

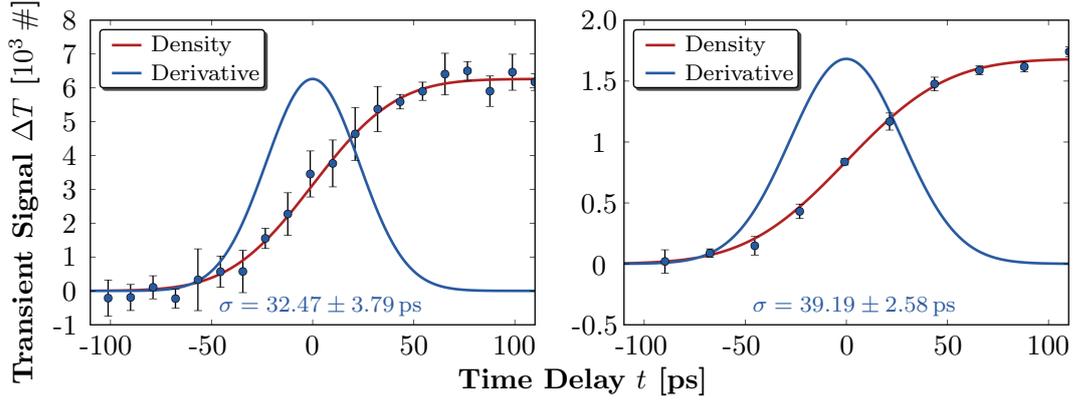


Figure 7.11.: Measured temporal evolution of the transient XAFS signal of $\text{Ir}(\text{ppy})_3$ dissolved in dimethyl sulfoxide (2 mM) at 11215 eV near feature A'_3 (L_3 -edge). The solid curves represent the fit curves, in particular a cumulative distribution function for the convolution of X-ray and laser pulse (red) and the corresponding derivative (blue), which represents the temporal shape of the X-ray (Gaussian).

Left: X-ray bunch length measured in May 2013 providing an overall resolution of ~ 33 ps (rms).

Right: X-ray bunch length of the beamtime in August 2013 was characterized as ~ 39 ps (rms).

are:

$$\begin{aligned}\sigma_{\text{May}} &= 32.47 \pm 3.79 \text{ ps}, \\ \sigma_{\text{August}} &= 39.19 \pm 2.58 \text{ ps}.\end{aligned}$$

In Sec. 6.3 the synchronization contribution (jitter) has been estimated to be around $\Delta t_{\text{rms}} \leq 1$ ps, while the laser pulse duration is a few hundred femtoseconds only. Therefore, the measured temporal resolutions correspond to the X-ray bunch length of PE-TRA III. Nevertheless, both resolutions denote a better temporal resolution than the usual design value of 44 ps (rms)^{xi}.

^{xi}Compare to previous work⁷.

7.3.2. Excited State Lifetime - Second-Order Decay Kinetics

The excited state dynamics were investigated by measuring the temporal decay of the transient signal ΔT near feature A'_3 at the L_3 -edge (11215 eV). Due to the expected long lifetime of the excited ${}^3\text{MLCT}$ triplet state, the laser pulses were shifted with respect to the X-ray pulses in 12 ns steps. The first data point now marks the temporal position at where the maximum signal was obtained (≈ 100 ps). Each data point (pumped and unpumped signal) was taken four times consecutively for $1.3 \cdot 10^6$ shots to obtain an estimate of the standard deviation. The unpumped signals were always taken with the gating scheme described in Sec. 5.7.1.

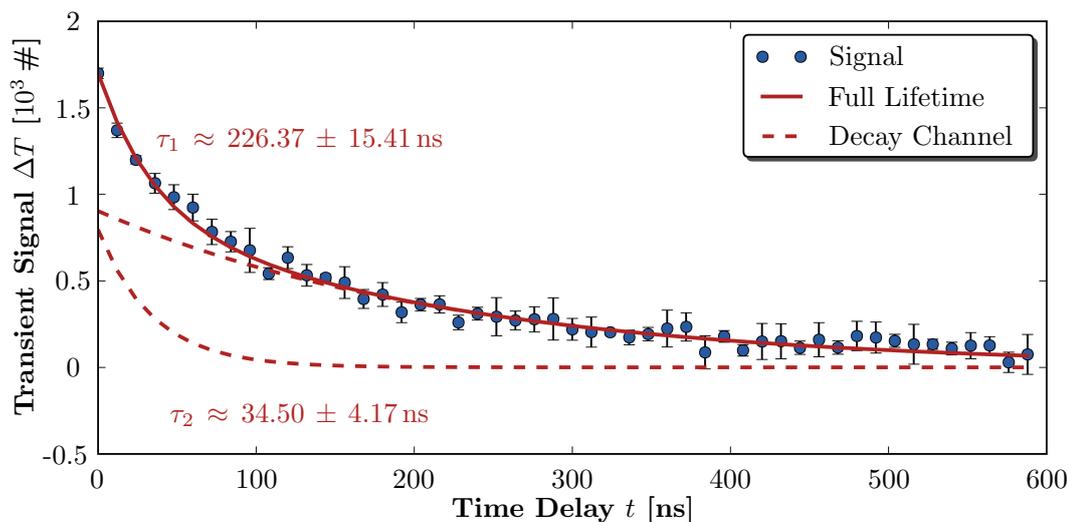


Figure 7.12.: Decay of the transient XAFS signal of $\text{Ir}(\text{ppy})_3$ dissolved in dimethyl sulfoxide measured at 11215 eV near feature A'_3 (L_3 -edge). The solid curve represents the fit curve, while the dashed curves correspond to the two decay channels. A long-living decay channel with $\tau_1 \approx 226$ ns and a fast channel with $\tau_2 \approx 34$ ns was extracted from the data.

The measured transient decay of the triplet state is shown in Fig. 7.12. The temporal decay cannot be described with a single exponential decay function, thus the transient signal is fitted with a bi-exponential decay function:

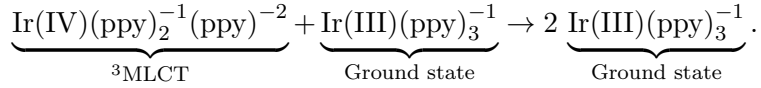
$$\Delta T(t) = A_1 \cdot e^{-t/\tau_1} + A_2 \cdot e^{-t/\tau_2}. \quad (7.11)$$

A least-squares fitting yields two nearly identical strong decay channel in amplitude with lifetimes of $\tau_1 \approx 226$ ns and $\tau_2 \approx 34$ ns. The determined lifetime of 226 ns is considerably shorter than the one reported in the literature ($\sim \mu\text{s}$)^{13,19,20}.

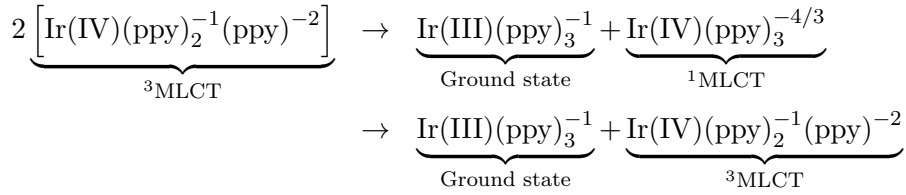
However, the experiment was carried out with a concentration of 2 mM of $\text{Ir}(\text{ppy})_3$ dissolved in dimethyl sulfoxide, leading to several mechanism which could affect the lifetime. The analysis follows now quite similar reference³³, which is based on the literature¹⁰¹.

For example quenching effects where collisions between excited triplet state molecules

and ground state molecules reduce the lifetime at higher concentrations^{98xii}:



In addition, since intense ultrashort-pulse laser excitations were used in these experiments, triplet-triplet annihilation can further shorten the excited state lifetime^{99xiii}. In this process an interaction of two nearby triplet state molecules (³MLCT) leads to the transition of one molecule to the higher excited singlet state (¹MLCT) while the other molecule is transferred to the singlet ground state⁹⁹. The formed ¹MLCT state further relaxes back non-radiatively to the initial triplet state resulting in an overall annihilation of one excited triplet state⁹⁹.



In order to mathematically describe and combine the different decay pathways, the literature^{33,101} introduced the rate equation of mixed first- and second-order decays as:

$$-\frac{dA(t)}{dt} = k_1 \cdot A(t) + k_2 \cdot A(t) \cdot B(t) + k_3 \cdot A^2(t), \quad (7.12)$$

where $A(t)$ and $B(t)$ are the concentrations of the excited ³MLCT state and ground state, respectively. Furthermore, k_1 is the rate constant representing the inverse of the lifetime τ_0 , k_2 is the rate constant accounting for the ground state quenching and k_3 is the second-order rate constant of the triplet-triplet annihilation process. The model was already applied in the following form to fit signals $\Delta T(t)$ with³³

$$\Delta T(t) = \alpha \cdot A(t) = \alpha \cdot \frac{(k_1 + k_2 B_0) A_0}{(k_1 + k_2 B_0 + (k_3 - k_2) A_0) \cdot e^{(k_1 + k_2 B_0)t} - A_0 (k_3 - k_2)}, \quad (7.13)$$

where α represents a scaling factor to link the excited state concentration $A(t)$ to the transient amplitude, B_0 denotes the ground state concentration before laser excitation and A_0 is the initial concentration of the excited state directly after photoexcitation.

The quenching rate constant k_2 and the lifetime τ_0 of Ir(ppy)_3 dissolved in dimethyl sulfoxide were determined in an independent laser spectroscopy experiment (see App. C) to $\tau_0 \approx 1.184 \mu\text{s}$ and $k_2 \approx 2.25 \cdot 10^8 (\text{M} \cdot \text{s})^{-1}$. Furthermore, the initial excited ³MLCT fraction was determined to be 13 % in a 2 mM solution as described in App. E, meaning that 87 % of the Ir(ppy)_3 molecules are in the ground state.

Inserting these values into Eq. (7.13) and by utilizing the least-squares method yields a successful curve fitting with $k_3 \approx 6.20 \cdot 10^{10} (\text{M} \cdot \text{s})^{-1}$, which is shown in Fig. 7.13. The determined rate constant k_2 agrees well with the rate constants reported for other solvents, e.g. the polar solvent acetonitrile with $k_2 \approx 5.75 \cdot 10^{10} (\text{M} \cdot \text{s})^{-1}$ and the

^{xii} Compare to the transition of the Ru(bpy)_3 complex shown in reference^{33,101}.

^{xiii} Also described in reference¹⁰⁰.

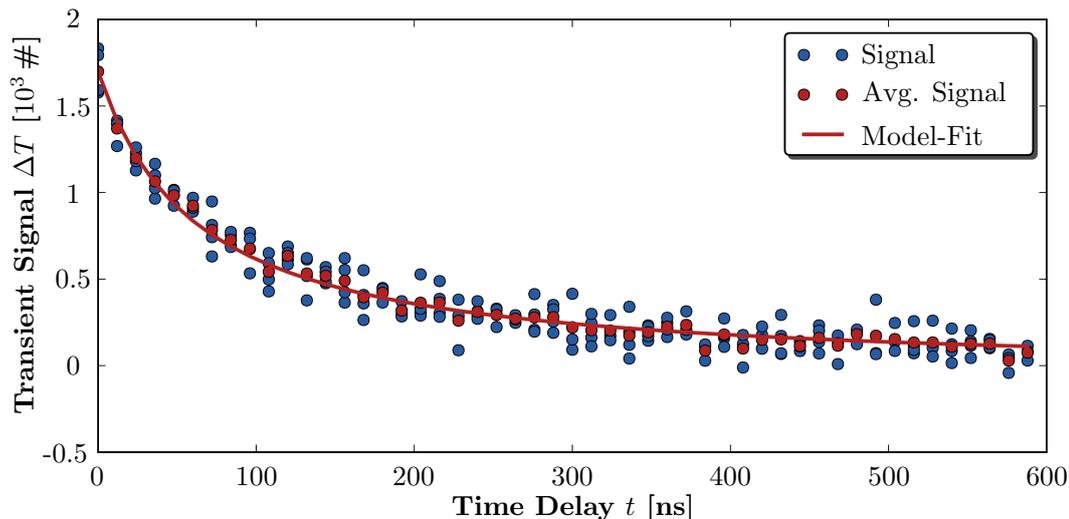


Figure 7.13.: Decay of the transient XAFS signal of Ir(ppy)₃ dissolved in dimethyl sulfoxide measured at 11215 eV near feature A₃' (L₃-edge). The solid curve represents the fitting curve using the model from Eq. (7.13).

nonpolar solvent toluene with $k_2 \approx 1.05 \cdot 10^6 \text{ (M} \cdot \text{s)}^{-1}$ ⁹⁸. Additionally, the now determined rate constant k_3 for triplet-triplet annihilation is comparable but slightly lower than those reported for other solvents⁹⁹. Hence, the triplet-triplet annihilation process is most probably the main reason of the shorter lifetime observed in the X-ray experiments compared to classical nanosecond laser spectroscopy.

The excited state lifetime was also measured at 12830 eV near feature B₂' with the same scan settings as used for the L₃-edge measurements. The results are shown in Fig. 7.14 and show a successfully fitted curve with a triplet-triplet annihilation rate constant of $k_3 \approx 4.34 \cdot 10^6 \text{ (M} \cdot \text{s)}^{-1}$. Conclusively, both determined triplet-triplet annihilation constants for the L₃ and L₂-edge are similar and the deviations can be explained by the relatively high noise level occurring in the L₂-edge measurement, which is noticeable in the wider spread of the data points in Fig. 7.14 compared to Fig. 7.13.

In conclusion, it is shown that the detected photoinduced electronic changes, which are related to the features A and B, are most likely similar and referenced to the ³MLCT triplet state.

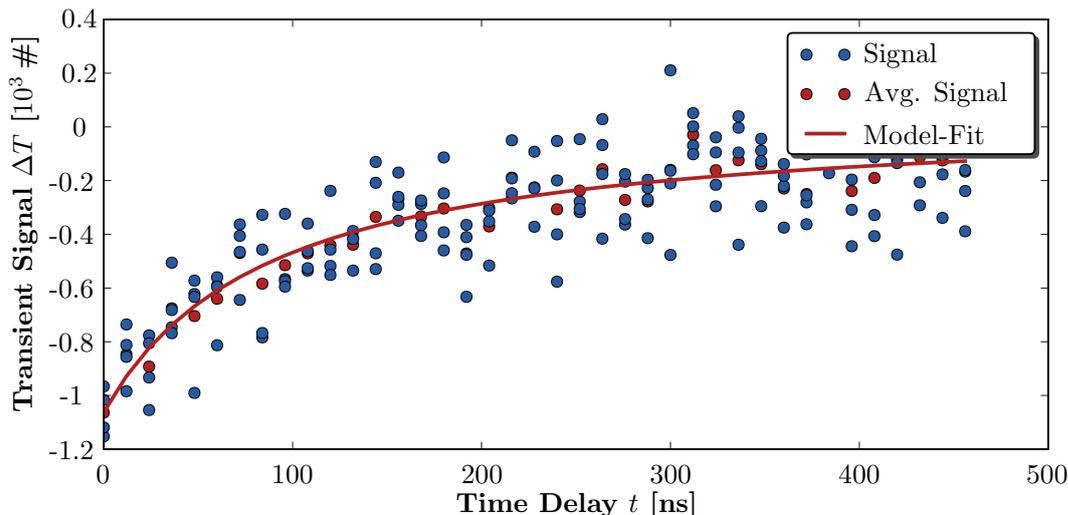


Figure 7.14.: Decay of the transient XAFS signal of $\text{Ir}(\text{ppy})_3$ dissolved in dimethyl sulfoxide measured at 12830 eV near feature B'_2 (L_2 -edge). The solid curve represents the fit curve using the model from Eq. (7.13).

7.4. Influence of Laser Fluence - Excitation Threshold

In order to get an estimate about possible nonlinear effects upon ultrashort pulse laser excitation and to obtain an excitation threshold, the transient difference signal ΔT was measured as a function of the laser pump fluence [J/cm^2] at a fixed X-ray energy E and a fixed time delay t .

The transient signal of $\text{Ir}(\text{ppy})_3$ dissolved in dimethyl sulfoxide (2 mM) was measured near feature A'_3 at the L_3 -edge spectrum (11215 eV) at a time delay of 100 ps in order to link the previous measurements to the fluence scan. Similar to the scans before, each data point (pumped and unpumped signal) was taken consecutively four times for $1.3 \cdot 10^6$ shots to obtain an estimate of the standard deviation. To prevent regenerative amplifier drifts upon different diode current settings and beam profile distortions, the laser output power was fixed to the maximum achievable output power. The pulse energy was further changed with a diffractive variable beam attenuator after the harmonic generator. The laser beam profile, which was used during all experiments, is shown in App. D and was characterized with the on-axis microscope described in Sec. 5.4. The laser spot size was determined to be 217 μm (FWHM).

The outcome of the fluence scan is shown in Fig. 7.15. Up to a fluence of about $7.5 \text{ mJ}/\text{cm}^2$ the transient signal increases in a more or less linear fashion. After a fluence level of $11.5 \text{ mJ}/\text{cm}^2$ the signal starts to saturate. The fluence used in the previous experiments is marked with a dashed red line at $9.9 \text{ mJ}/\text{cm}^2$. With a laser pulse duration of ca. 170 fs the fluence corresponds to a power density of $< 52 \text{ GW}/\text{cm}^2$. At these low power densities we expect the solvent effects to be negligible. Moreover, the increase of the transient signal up to the experimental region suggests that the desired ${}^3\text{MLCT}$ state is the dominant photoproduct inside sample solution, thus we expect the

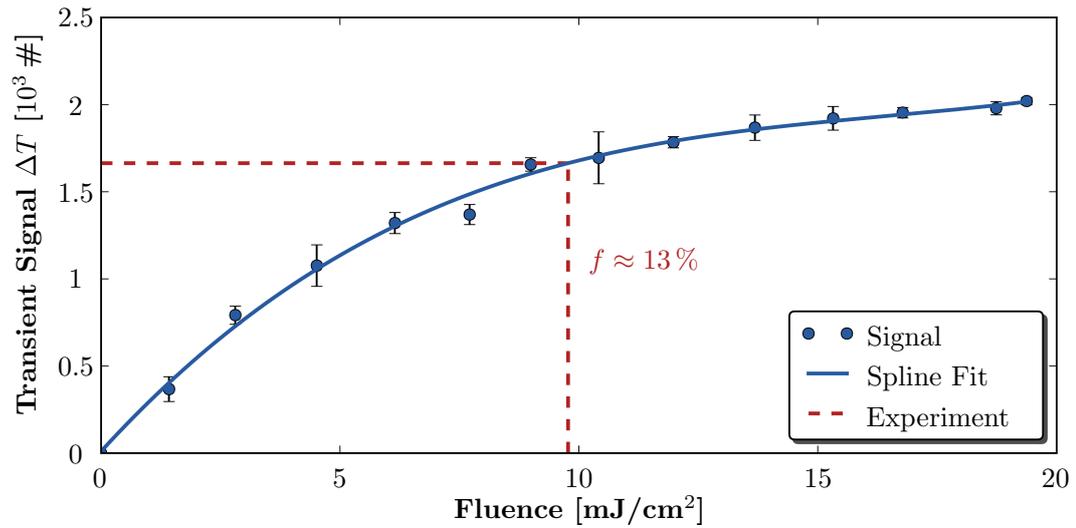


Figure 7.15.: Measured transient XAFS signal of Ir(ppy)₃ dissolved in dimethyl sulfoxide (2 mM) measured near feature A₃' at 11215 eV (L₃-edge) as a function of the incident fluence. The fluence used in the XAFS experiments is indicated with a dashed red line.

generation of other photoproducts to be low. Extrapolating the polynomial function will result in an excitation threshold around $16 \pm 1\%$.

7. *Time-Resolved Pump and Probe X-ray Absorption Fine Structure Spectroscopy Experiments*

8. Summary and Outlook

This thesis presents the development and establishment of a pump and probe X-ray absorption spectroscopy experiment with picosecond time resolution at beamline P11 (PETRA III) in Hamburg. For this reason, the user-friendly software development and hardware commissioning/development depicted an elemental part of this work. Above sixty thousand lines of python code had to be written for experiment and beamline operation.

Moreover, an ultrashort pulse laser system including laser safety concept was selected, installed, optimized and commissioned at beamline P11 for user operation. The PETRA III master reference was characterized with a timing jitter of $\Delta t_{rms} \approx 452$ fs. The synchronization of the laser system to the master reference was determined to be long-term stable with a timing jitter of $\Delta t_{rms} \leq 1$ ps.

An optical feedback system for the UV/VIS beam was implemented at beamline P11 and can be used either with quadrant detectors or ethernet based CCD cameras. This powerful tool can be further used to fine-tune spatial overlaps between X-ray and laser beam during pump and probe experiments.

Additionally, the first feedback mechanism for X-ray beam position control by using an aluminium coated diamond foil as quadrant detector has been established at PETRA III. The spatial X-ray stability at beamline P11 was characterized in great detail. The outcome revealed serious stability problems of the X-ray beam position. The origin of the X-ray beam position deviations was linked to angular vibrations of the two crystals inside the monochromator chamber. As a consequence the data acquisition of the XAFS setup was basically limited to the single photon counting regime due to the fact that a beam defining pinhole had to be over-illuminated at the cost of photon flux to obtain a quasi-stable X-ray beam. Nevertheless, the X-ray beam basically oscillates at a frequency of 46 Hz around the defined position with variations of $\approx 1 \mu\text{rad}$ (rms) in the vertical direction as shown in the framework of this thesis. These intensity changes were still present in the quasi-stable X-ray beam and further reduced the repetition rate of the data acquisition from the originally planned 520 kHz to 130 kHz. In particular the repetition rate of the laser system had to be reduced to account for the revolution frequency of the synchrotron to measure both the static unpumped and the time-resolved pumped signals with the same X-ray bunch. This finally reduced the noise contributions in the XAFS spectra to a working standard. However, the step scan operation of the monochromator still led to constant beam position displacements, e.g. the position sometimes even jumps after the movement of the second crystal while approaching for a new energy. This problem could be solved by establishing an X-ray feedback system, which allows to keep the X-ray beam position stable on a reasonable level. Without closed loop control of the X-ray beam position reproducible time-resolved X-ray absorption spectroscopy measurements were not possible.

8. Summary and Outlook

Hence, many efforts went into adapting the present setup to the X-ray beam instabilities caused by the monochromator. From this point of view the monochromator is not suitable for any energy scanning experiment, e.g. X-ray absorption spectroscopy, and a replacement has to be considered in the future.

As an overall consequence, the obtained signal-to-noise ratios - even with a photoexcitation yield of $\approx 13\%$ - were rather small in the fine-structure region and the laser induced structural changes could not be fully sustained by an investigation of the fine-structure modulations.

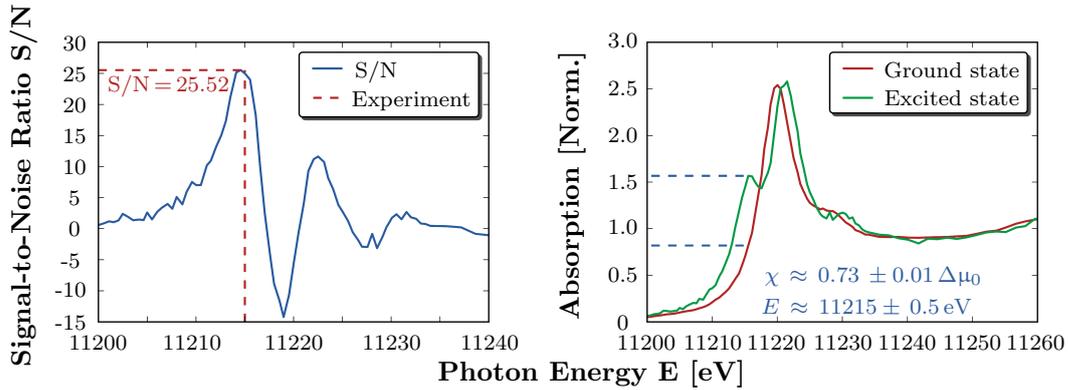


Figure 8.1.: **Left:** Measured S/N ratios as a function of the X-ray energy E assuming a shot-noise limited experiment. The dashed line indicates the S/N ratio around 11215 eV, which was estimated to $S/N \approx 25.52$. **Right:** Ground state and calculated excited state spectrum of $\text{Ir}(\text{ppy})_3$ at the L_3 -edge. The modulation in the absorption cross section relative to the absorption edge-jump is approximately 73% in the energy region around 11215 eV.

Assuming a shot-noise limited experiment, the related calculated S/N ratios of the L_3 -edge spectrum are shown in Fig. 8.1. The maximum S/N ratio was measured in the energy region around 11215 eV with approximately 25.5, which was formerly denoted as feature A. Thereby, the absorption coefficient modulation relative to the edge-jump is around 73%. The L-edge experiments in this thesis had to be performed at roughly 5-7% of the available photon flux due to the spatial X-ray beam instabilities as previously described. The second KB mirror system was successfully commissioned at beamline P11 in January 2014 and can further improve the experiment by providing the full photon flux with beam sizes of a few micron only. The X-ray absorption spectroscopy setup was flexibly designed on a six-axle kinematic positioning system (hexapod), which allows to transport the experiment fairly easy behind the second KB mirror system. Considering now the full photon flux of approximately $2.0 \cdot 10^{13}$ photons per second and an increase of the repetition rate of the data acquisition to 520 kHz, future S/N ratios can be considerably improved by a factor of ~ 9 .

Such photon flux densities require the application of a data acquisition scheme, which is able to distinguish between single and multi-photon events. The corresponding electronics, a so-called gated integrator, can be provided by the "Joint Electronics Team" (European XFEL) and was successfully tested on several occasions in a huge collaboration at beamline P11. These devices integrate the analog signal of the avalanche photodiode (fluorescence signal) over a preset time gate and thus deliver a magnitude

that is proportional to the detected fluorescence photons⁴⁵ⁱ.

The instrumental part led to the first successful external user experiments in time-resolved X-ray absorption spectroscopy in October 2013 and January 2014.

The utilizability of the developed time-resolved X-ray absorption experiment to detect charge transfers in transition metal complexes has been successfully shown in the framework of this thesis.

The first static and time-resolved X-ray absorption spectroscopy experiments of the green phosphorescence emitter complex Ir(ppy)₃ dissolved in dimethyl sulfoxide were conducted. In particular static and time-resolved L₃- and L₂-edge absorption spectra of iridium were measured to investigate the structural and electronic changes upon photoexcitation. Thereby, the metal-to-ligand charge transfer band of Ir(ppy)₃ was photoexcited with femtosecond laser pulses at a wavelength of 343 nm and afterwards probed with X-ray pulses at a time delay of 100 ps. The excited ³MLCT state was derived with an ionic approximation from the measured transient difference spectrum. The results obtained confirm and present a direct visualization of the metal-to-ligand charge transfer with a measured ionization potential shift of 1.9 ± 0.1 eV, caused by the temporal oxidation of the central iridium atom. The octahedral crystal field splittings 10Dq were determined from the XAFS spectra as:

$$\begin{aligned} 10Dq^{\text{GS}} &= 6.12 \pm 0.37 \text{ eV}, \\ 10Dq^{\text{ES}} &= 6.43 \pm 0.20 \text{ eV}, \end{aligned}$$

for the ground and excited state, respectively. The octahedral crystal field splittings were further used to calculate the, to our knowledge, first experimental estimate of the bond length change upon photoexcitation in an octahedral approximation. It was revealed that the bond length of the first coordination shell of the iridium atom *decreases* in the triplet state by roughly 1%. The site symmetry of this transition metal complex was found to be pseudo-octahedral.

Additional time scans, in which the laser pulse is temporally shifted with respect to the X-ray pulse, were performed to determine the X-ray bunch length in 40 bunch mode and revealed a temporal resolution between 33 ps and 39 ps rms. Both measured values actually denote a shorter bunch length than the usually designed value of 44 ps rms and sustain the magnitude that has been measured in a previous work⁷.

Furthermore, the first and second-order decay kinetics of the triplet state were investigated in a combination of X-ray and laser based experiments and revealed rate constants in case of dimethyl sulfoxide as solvent, to be $k_q = 2.25 \cdot 10^8 \text{ (M} \cdot \text{s)}^{-1}$ and $k_{\text{T TA}} = 6.20 \cdot 10^{10} \text{ (M} \cdot \text{s)}^{-1}$ for the ground state quenching and the annihilation process, respectively.

From a scientific point of view it is highly desirable to investigate other phosphorescent iridium complexes such as Ir(piq)₃ or FIrpic. The determination of the crystal field splittings and their comparison to Ir(ppy)₃ can provide further information to our understanding of the metal-ligand interaction. In addition, the obtained XAFS spectra of Ir(ppy)₃ can be theoretically investigated utilizing the multiplet model presented in reference^{104,105}. This could further allow to refine and sustain the obtained crystal field splittings.

ⁱA detailed description of the data analysis is provided in reference⁴⁵.

8. *Summary and Outlook*

A. Example of a Deglitching Process

During X-ray absorption measurements so-called *glitches* can occur. They are identified as spikes in the absorption data and occur in consequence of incident beam and sample inhomogeneities¹⁰⁶. Glitches crucially disturb a data analysis, for example the resonance fitting with Voigt profiles⁹¹, and have to be deglitched properly. For a detailed description of the shape of those glitches the reader is referred to the literature¹⁰⁶.

A typical deglitching process is shown in Fig. A.1. As an example the L_3 -edge spectrum of $\text{Ir}(\text{ppy})_3$ is shown, where several monochromator glitches can be identified (red curve). All glitches occurring in the data sets within this thesis have been removed

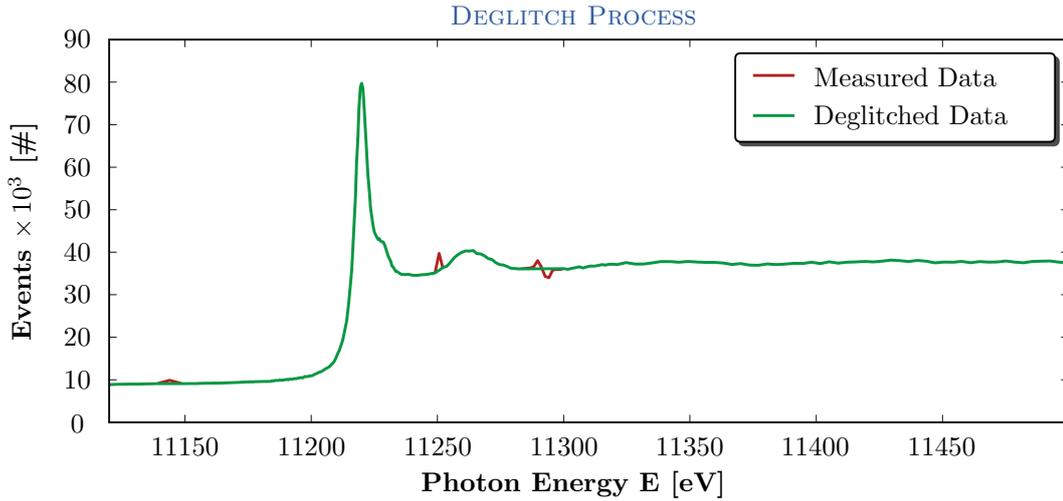


Figure A.1.: Measured X-ray fluorescence at the L_3 -edge of iridium. The data has been properly deglitched using a linear interpolation of the fluorescence events between adjacent data points. The relative change in the transient absorption spectrum was kept constant during deglitching.

with a linear interpolation of the fluorescence data between adjacent energies and the relative difference between the pumped and unpumped signals has been kept constant during the deglitching process. The outcome is shown in Fig. A.1.

A. *Example of a Deglitching Process*

B. Optical Spectroscopy - Molar Extinction Coefficients

The following description is completely taken from a previous work⁶. The analysis follows also reference⁶.

The working principle of a UV-VIS spectrometer is based on the illumination of a sample solution with a broadband light source. Typically, the sample solution is placed in a cuvette of a given thickness d . During experiment the magnitudes of the incident intensity I_0 and the transmitted intensity I_t are consecutively measured for each wavelength. For this reason, gratings are used in order to extract the different wavelengths out of the broadband light source. The absorption coefficient α can be determined via Lambert-Beer⁶

$$I_t(\lambda) = I_0(\lambda) \cdot e^{-\alpha(\lambda) \cdot d}, \quad (\text{B.1})$$

and is related to the absorbance A , which is defined as⁶:

$$\begin{aligned} A(\lambda) &= -\ln\left(\frac{I_t(\lambda)}{I_0(\lambda)}\right) \\ &= \alpha(\lambda) \cdot d. \end{aligned} \quad (\text{B.2})$$

The absorption coefficient $\alpha(\lambda)$ is further related to the molar extinction coefficient $\varepsilon(\lambda)$ via⁶

$$\alpha(\lambda) = \varepsilon(\lambda) \cdot c. \quad (\text{B.3})$$

Hence, the molar extinction coefficient is given in a proportional concentration dependence to the absorbance A . In order to calculate extinction coefficients ε of Ir(ppy)₃ in dimethyl sulfoxide, several absorption spectra at different sample concentrations have to be measured for a given sample thickness. Typically the extinction coefficient is expressed in terms of (M · cm)⁻¹.

Several UV-VIS absorption spectra of Ir(ppy)₃ at different concentrations were measured with a commercial UV-VIS spectrometer (Shimadzu UV 6700). The spectrometer is working with a cuvette system at a cuvette thickness of 1 cm⁶.

The measured spectra for 10 different concentrations and a blank measurement for baseline/solvent correction are shown in Fig. B.1. The linear dependence of the absorbance as a function of concentration is clearly visible and essential for a further data analysis. For a selected wavelength, e.g. 343 nm as used in the XAFS experiment for photoexcitation, the measured data can then be fitted with the linear regression $A = \varepsilon \cdot c \cdot d$ ⁶. The determined extinction coefficient for $\lambda_{ex} = 343$ nm is $\varepsilon \approx 15200 \text{ M}^{-1}\text{cm}^{-1}$ (see Fig. B.2).

B. Optical Spectroscopy - Molar Extinction Coefficients

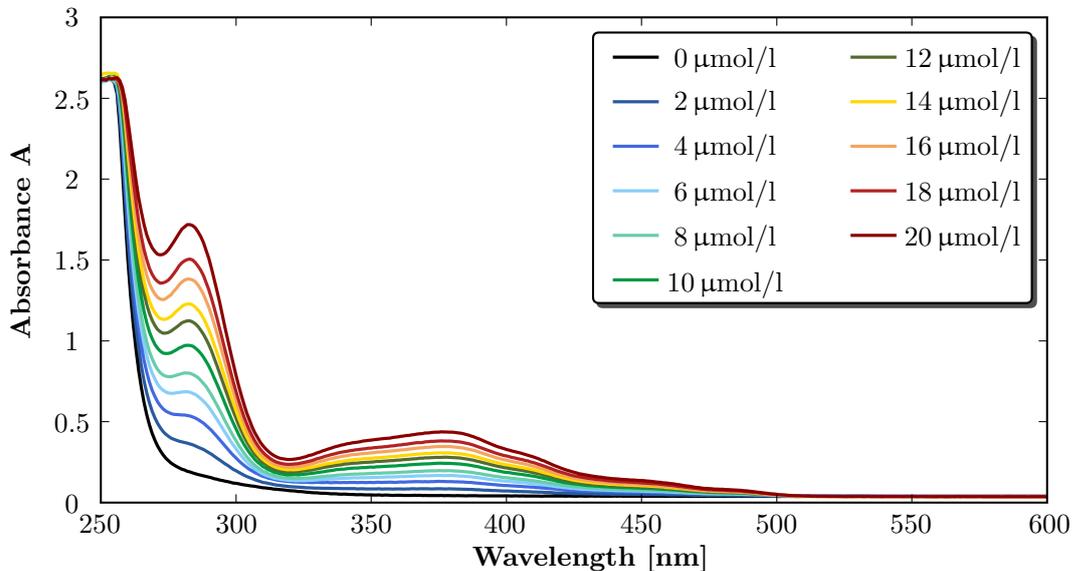


Figure B.1.: Steady-state UV-VIS measurements for 10 different concentrations of $\text{Ir}(\text{ppy})_3$ dissolved in dimethyl sulfoxide and an additional blank measurement with solvent only (black curve)¹⁰⁷. The linear dependence of the absorbance is clearly visible and essential for a further data analysis.

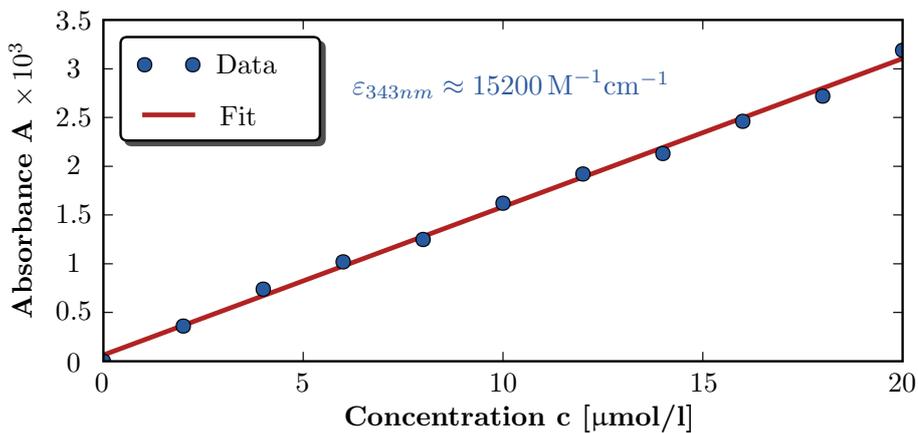
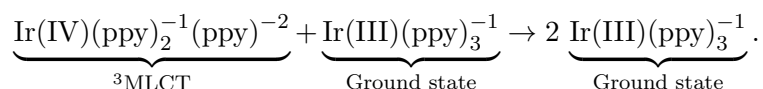


Figure B.2.: Plotted values of the absorbance A (blue) for a given wavelength of $\lambda_{ex} = 343 \text{ nm}$ as a function of sample concentration. A linear regression line $A = \epsilon \cdot c \cdot d$ (red) is fitted to determine the extinction coefficient.

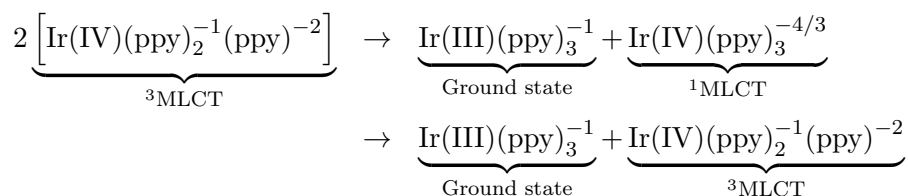
C. Optical Lifetime Measurements - First-Order Decay Kinetics

This appendix presents an investigation of the luminescence quenching mechanism of Ir(ppy)₃ dissolved in dimethyl sulfoxide at room-temperature. As described in Sec. 3.4, after photoexcitation the ¹MLCT state is formed which subsequently crosses (≈ 100 fs) to the ³MLCT triplet state²⁰. The excited state then decays to the ground state by emitting phosphorescence²⁰.

Commonly the phosphorescence lifetime is shortened at higher concentrations due to efficient self-quenching⁹⁸, which is also referred to as ground state quenching¹⁰¹. Thereby, collisions between excited triplet state molecules and ground state molecules reduce the lifetime at higher concentrations⁹⁸. In an ionic approximation the transition can be described by (see also Sec.3.4)ⁱ



Furthermore, triplet-triplet annihilation can be triggered upon intense short-pulse laser excitations and further shorten the excited state lifetime⁹⁹ⁱⁱ.



In this process an interaction of two nearby triplet state molecules (³MLCT) leads to the transition of one molecule to the higher excited singlet state (¹MLCT) while the other molecule is transferred to the singlet ground state⁹⁹. The formed ¹MLCT state further relaxes back non-radiatively to the initial triplet state resulting in an overall annihilation of one excited triplet state⁹⁹.

A schematic drawing of the optical setup is shown in Fig. C.1. In this experiment an actively Q-switched Nd:YAG based system featuring 1.5 ns long laser pulses at 355 nm wavelength is utilized to excite the sample, which is stored in a cuvette. The application of rather long laser pulses in these experiments is based on the motivation to retain the incident power density at rather low values to avoid triplet-triplet annihilation or

ⁱCompare to the transition of the Ru(bpy) complex shown in reference^{33,101}.

ⁱⁱAlso described in reference¹⁰⁰.

C. Optical Lifetime Measurements - First-Order Decay Kinetics

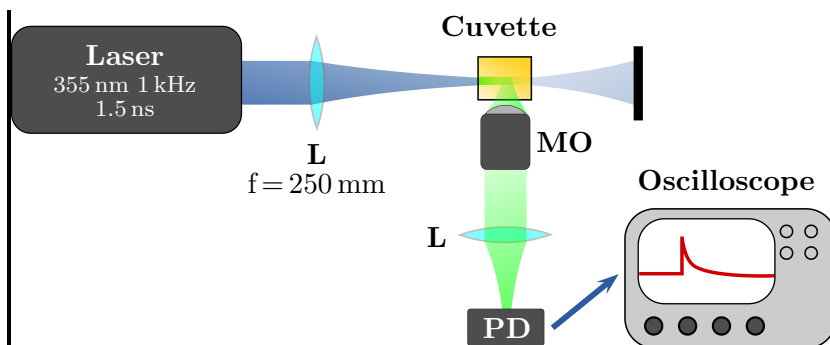


Figure C.1.: Simplified layout of the experimental setup utilized to characterize the quenching rate constant of $\text{Ir}(\text{ppy})_3$ in dimethylsulfoxide. L: Lens, MO: Microscope objective.

other nonlinear effects. The laser beam is focused by a lens ($f = 250$ mm) onto the sample at an outer edge of the cuvette to reduce self-absorption of the phosphorescence. The latter is collected by a microscope objective and guided onto a fast photodiode. The signal is later on amplified by a 40 dB amplifier at 200 MHz bandwidth and then fed into a fast digital oscilloscope to measure the lifetime (600 MHz).

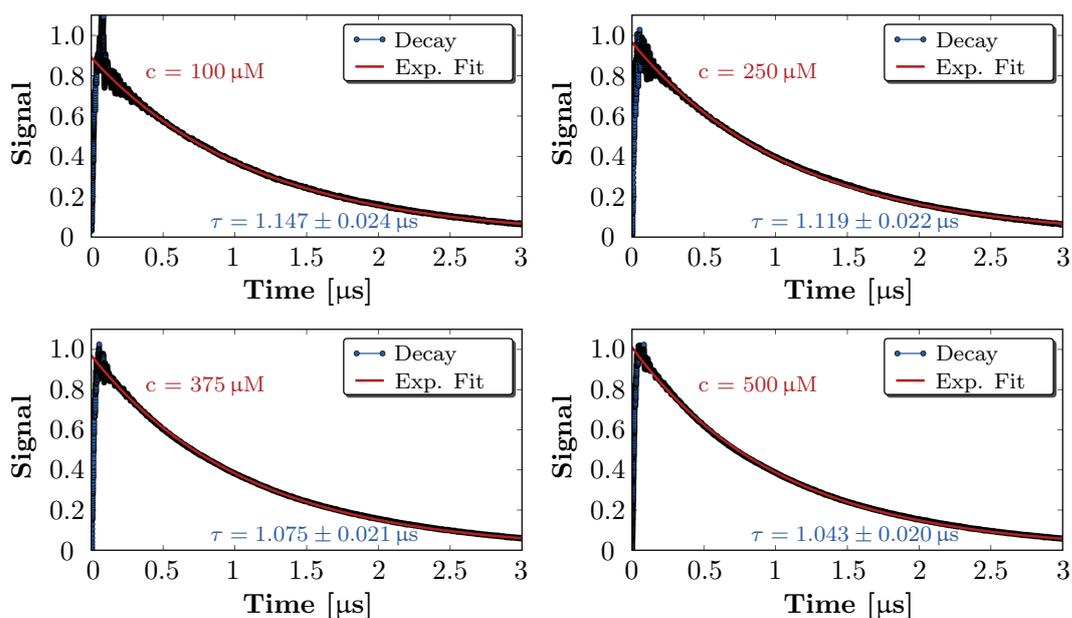


Figure C.2.: Measured luminescence decays for different concentrations of $\text{Ir}(\text{ppy})_3$ dissolved in dimethyl sulfoxide.

To characterize the ground state quenching rate, the phosphorescence lifetime was measured for different concentrations of $\text{Ir}(\text{ppy})_3$ dissolved in dimethyl sulfoxide. The analysis and line of argumentation is based on reference^{98,101}. The measured phosphorescence lifetimes for four different concentrations are shown in Fig. C.2. An incident fluence of $0.1 \text{ mJ}/\text{cm}^2$ was used for each measurement. Moreover, the fluence of interest is indeed lower since the phosphorescence was collected from excited sample molecules

located near the center of the cuvette with respect to the incident laser beam. Considering the pulse duration of roughly 1.5 ns, the incident fluence translates to a power density of $< 63 \text{ kW/cm}^2$.

Each phosphorescence signal was fitted successfully with a single exponential decay function utilizing the least-squares method. Although the fit quality is relatively poor due to the weak amplified signal, a quenching mechanism is clearly visible and illustrated in a *Stern-Volmer* plot in Fig. C.3. The Stern-Volmer series shows a linear behavior of the reciprocal phosphorescence lifetime as a function of the sample concentration, which strongly suggests that the underlying mechanism is indeed ground state quenching¹⁰¹.

According to the literature⁹⁸, the quenching mechanism can be expressed with the equation

$$\frac{1}{\tau} = \frac{1}{\tau_0} + k_q, \quad (\text{C.1})$$

where τ_0 denotes the lifetime at infinite dilution and k_q stands for the quenching rate constant. A least-squares fit yields a lifetime $\tau_0 = 1.184 \pm 0.029 \mu\text{s}$ and a quenching rate constant of $k_q = (2.25 \pm 0.62) \cdot 10^8 \text{ M}^{-1}\text{s}^{-1}$.

The depicted linear behavior of the reciprocal lifetime as a function of concentration as well as the magnitude of the quenching rate constant k_q are in agreement with the quenching rate reported for the polar solvent acetonitrile, which is reported as $k_q = 5.75 \cdot 10^{10} \text{ M}^{-1}\text{s}^{-1}$ ⁹⁸. Furthermore, the magnitude of the quenching rate implies a diffusion-controlled process⁹⁸.

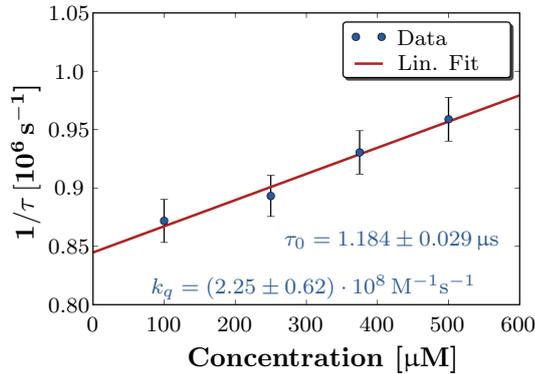


Figure C.3.: The determined decays rates are summarized in a Stern-Volmer plot to determine the self-quenching rate k_q as well as the lifetime τ_0 .

C. Optical Lifetime Measurements - First-Order Decay Kinetics

D. Calculation of the Excitation Yield Maximum

This section presents a simple approach to derive the theoretical excitation yield maximum within a time-resolved pump and probe experiment. Similar calculations can be also found in great detail in a previous work⁶.

For this purpose the laser focus was monitored in the plain of the liquid jet by the on-axis microscope (see Sec. 5.4) and a cerium doped YAG crystal as scintillator. The visualized laser focus within the experiments can be seen in Fig. D.1.

$$\text{FWHM}_h^{yag} = 284 \mu m$$

$$\text{FWHM}_v = 217 \mu m$$

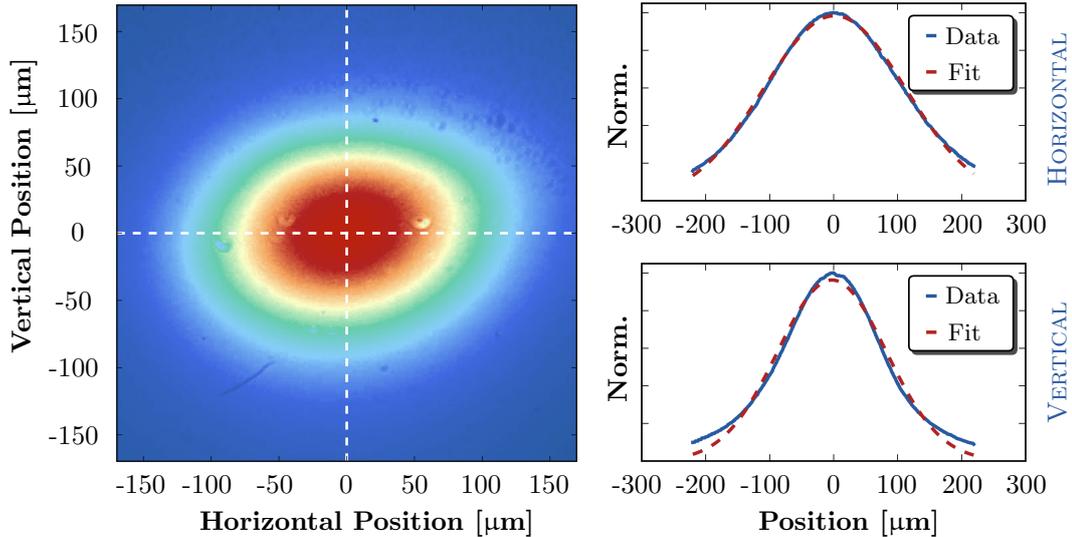


Figure D.1.: **Left:** Monitored laser focus in the plain of the liquid jet visualized by the on-axis microscope and a cerium doped YAG crystal as scintillator. **Right:** Plotted profiles for the horizontal (top) and vertical direction (bottom) with fitted Gaussians.

The laser beam is broadened in the horizontal direction on the YAG crystal (see Fig. D.2), which can be utilized to estimate the angle of incidence

$$\alpha = \arcsin\left(\frac{\text{FWHM}_h^{yag}}{\text{FWHM}}\right), \quad (\text{D.1})$$

D. Calculation of the Excitation Yield Maximum

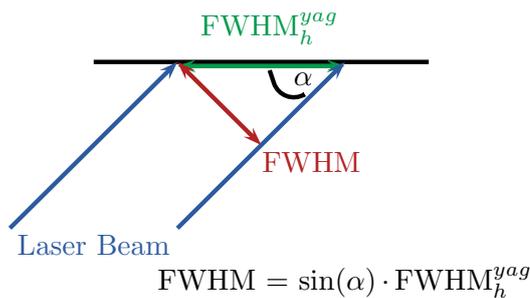


Figure D.2.: Illustration of the present laser beam geometry with respect to the YAG crystal. The laser beam profile is broadened in the horizontal direction while the vertical profile remains unaffected.

delivering an angle of incidence of $\alpha \approx 50^\circ$. In the following the time-dependence of the excited state relaxation is not considered due to the long-living triplet state of the iridium complex. With the recapitulated expression Eq. (2.32)

$$f(0) = \frac{q \cdot N_0^{\text{ph}}}{c N_A V_{\text{ex}}} \left(1 - e^{-c N_A (1-f(0)) \sigma_{\text{opt}} d} \right). \quad (\text{D.2})$$

and the following expressionsⁱ

$$\begin{aligned} \sigma_{\text{opt}} &= \frac{2303 \cdot \varepsilon}{N_A}, & \text{Cross Section}^{108} \\ E_{\text{ph}} &= \frac{h \cdot c_l}{\lambda}, & \text{Photon Energy} \\ N_0^{\text{ph}} &= \frac{E_{\text{Pulse}}}{E_{\text{ph}}}, & \text{Number of Photons} \end{aligned}$$

where N_A is the Avogadro constant, c is the sample concentration, c_l is the speed of light and ε the extinction coefficient for the pump wavelength λ , the excitation yield curve can be calculated with the parameters listed in Tab. D.1. The numerical out-

Table D.1.: Listed parameters for the numerical calculation of the maximum excitation yield according to Eq. (D.2).

Parameter	Magnitude
λ	343 nm
ε	$15200 \text{ M}^{-1} \text{ cm}^{-1}$
r_{jet}	100 μm
FWHM	217 μm
c	2 mmol/l
q	1

come is shown in Fig. D.3 and shows a quasi-linear progression of the excitation yield as a function of the incident laser fluence. The fluence used during the experiments

ⁱCompare to reference⁶

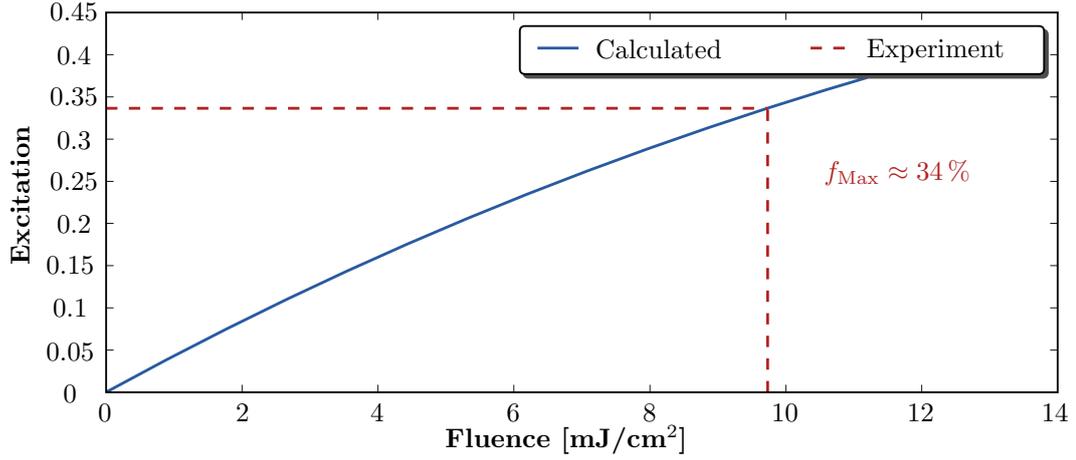


Figure D.3.: Calculated numerical excitation yield for the experiment using Eq. D.2.

is marked with a dashed red line. At this fluence level multi-photon absorption can be neglected. With a pulse duration of about $\tau \approx 170$ fs, the fluence translates to a power density of < 58 GW/cm².

Nevertheless, in this calculation solvent absorption or the generation of other photo-products than the desired one ($q = 1$), are not considered. Furthermore, the small Fresnel reflection from the liquid jet upon laser illumination as well as stimulated emission are not taken into account. Therefore, the calculated excitation yield of $f(0) \approx 34\%$ represents an upper threshold for the photoexcitation yield for the experiments performed within this thesisⁱⁱ:

$$f_{\text{Max}} \geq f_{\text{exp}}. \quad (\text{D.3})$$

ⁱⁱCompare also to reference³⁴.

D. Calculation of the Excitation Yield Maximum

E. Calculation of the Excitation Yield

In order to obtain the excitation yield, the $\text{Ir}(\text{ppy})_3$ complex is treated in an ionic approximation at the L_3 -edge. The following method was also applied in a previous work³³. Thereby, the ground state and the excited state are treated according to their - ionically approximated - electronic configuration of the metal valence orbitals (5d). In more detail, the photoinduced vacancy in the t_{2g} set defines the electronic structure of the excited state as a $5d^5$ configuration while the ground state is represented by a $5d^6$ configuration (see Sec. 3.4)ⁱ. As characterized in Sec. 7.1, the edge resonance originates from the absorption of excited 2p core electrons in the metal valence orbitals (5d). Therefore, the integrated ground state absorption $A_{\text{GS}}^{\text{edge}}$ obtained at the edge resonance corresponds to 4/10 of the hypothetical integrated edge absorption $A_{\text{d-empty}}^{\text{edge}}$, which would arise from completely empty metal valence orbitals. In turn, the integrated edge absorption in the excited state $A_{\text{ES}}^{\text{edge}}$ is related to 5/10 of the integrated edge absorption with empty metal valence orbitals:

$$A_{\text{GS}}^{\text{edge}} = \frac{4}{10} A_{\text{d-empty}}^{\text{edge}}, \quad (\text{E.1})$$

$$A_{\text{ES}}^{\text{edge}} = \frac{5}{10} A_{\text{d-empty}}^{\text{edge}}. \quad (\text{E.2})$$

Inserting Eq. (E.1) in Eq. (E.2) further yields the condition of the ionic approximation³³

$$A_{\text{ES}}^{\text{edge}} = \frac{5}{4} A_{\text{GS}}^{\text{edge}}. \quad (\text{E.3})$$

The measured and normalized ground state spectrum $A_{\text{GS}}(E)$ of $\text{Ir}(\text{ppy})_3$ as well as the transient spectrum $\Delta T(E, t)$ at the L_3 -edge are shown in Fig. E.1. As described in Sec. 2.3, the measured intensities at time delay t in a laser pump and X-ray probe configuration depend on the fraction of the excited state species. Therefore, the measured transient difference spectrum $\Delta T(E, t)$ is defined as^{9,10,33}

$$\Delta T(E, t) = f(t) \cdot (A_{\text{ES}}(E, t) - A_{\text{GS}}(E)), \quad (\text{E.4})$$

where $f(t)$ denotes the photoexcitation yield and $A_{\text{ES}}(E, t)$ and $A_{\text{GS}}(E)$ are the excited state spectrum and the ground state spectrum, respectively. The excited state spectrum can then be derived by

$$A_{\text{ES}}(E, t) = \frac{\Delta T(E, t)}{f(t)} + A_{\text{GS}}(E). \quad (\text{E.5})$$

In the following, the spectral resonances A' and B, which characterize the absorption of photoelectrons in the metal valence orbitals (see Sec. 7.1 and Sec. 7.2), are considered

E. Calculation of the Excitation Yield

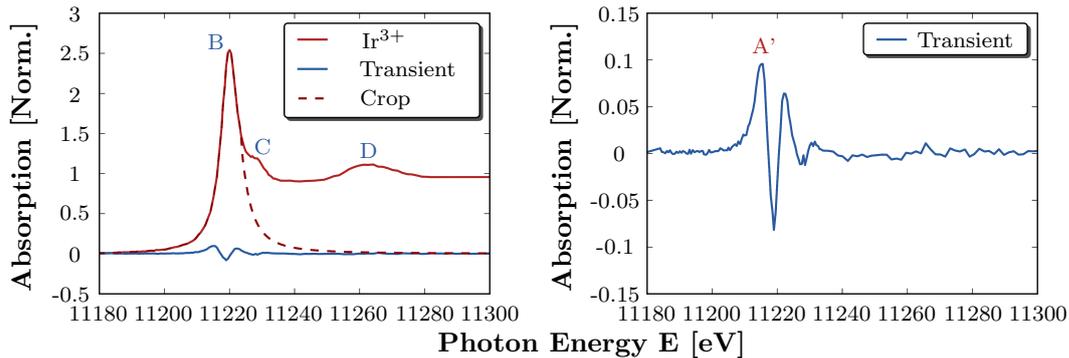


Figure E.1.: **Left:** Measured ground state spectrum A_{GS} (red) of $\text{Ir}(\text{ppy})_3$ together with the measured transient spectrum (blue) at the L_3 -edge. The cropped edge is shown as dashed lines and is further utilized for excited state calculation.

Right: Magnified transient spectrum ΔT measured after ≈ 100 ps of photoexcitation, also denoted as pump-probe spectrum. The maximum giving rise to the additional transition is denoted as A' .

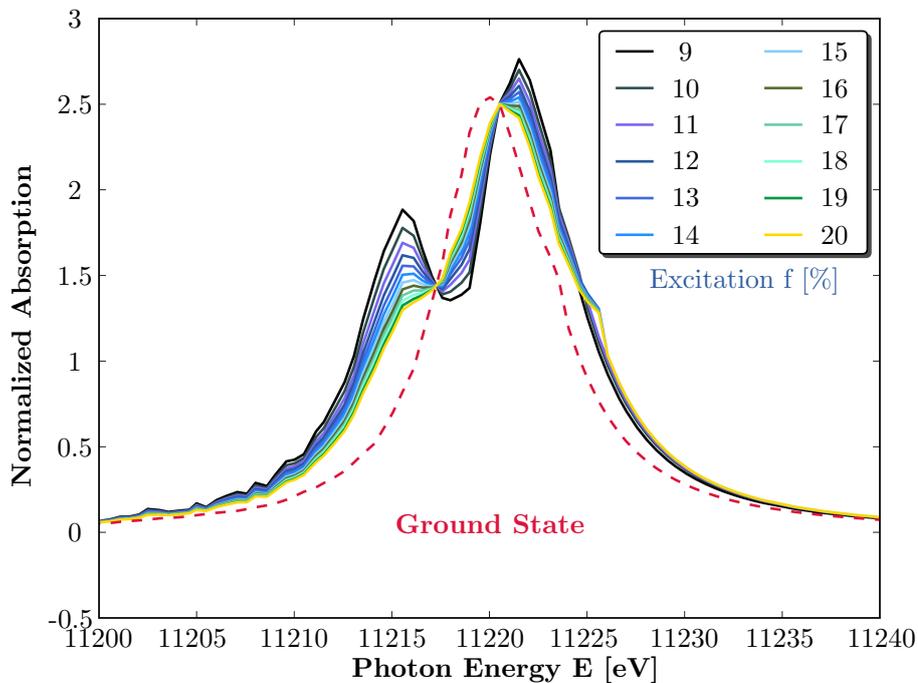


Figure E.2.: Calculated edge resonances according to Eq. (E.5) for different assumed excitation yields.

to calculate the excitation yield $f(t)$ and thus the excited state spectrum $A_{ES}(E, t)$. At first, the spectral resonance B of the ground state is extracted from the spectrum utilizing a Voigt profile^{90,91}, which is illustrated in Fig. E.1 as dashed curve. The in-

ⁱCompare also to the reference⁹ where the $\text{Ru}(\text{bpy})_3$ complex is described which exhibits a similar photocycle.

tegral of the ground state resonance delivers $A_{\text{GS}}^{\text{edge}} = 25.81 \text{ eV}$.

Afterwards, excited state spectra are generated according to Eq. (E.5) for different assumed photoexcitation yields. The corresponding spectral resonances, constituting a superposition of feature A' and B, are subsequently extracted in a similar procedure as for the ground state spectrum. The outcome is shown in Fig. E.2, showing the spectral resonances of interest for excitation yields ranging from 9 % to 20 %.

According to the ionic approximation, the relationship

$$A_{\text{ES}}^{\text{edge}} = \frac{5}{4} A_{\text{GS}}^{\text{edge}}.$$

where $A_{\text{ES}}^{\text{edge}}$ and $A_{\text{GS}}^{\text{edge}}$ are the integrals of the excited state and ground state resonance, respectively, must be fulfilled. The calculated integrals of the excited state

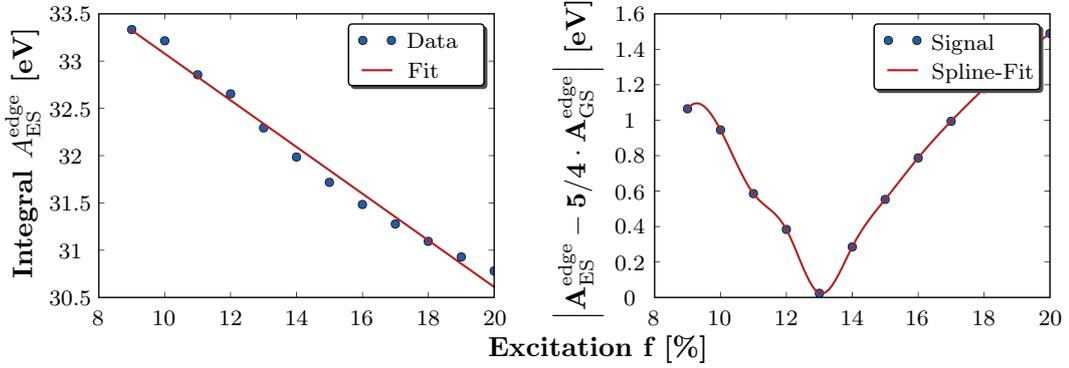


Figure E.3.: **Left:** Plotted integral values of the excited state resonances $A_{\text{ES}}^{\text{edge}}$ as a function of the photoexcitation yield.

Right: Plotted absolute difference $\Delta A = |A_{\text{ES}}^{\text{edge}} - 5/4 \cdot A_{\text{GS}}^{\text{edge}}|$ shows a minimum around $f \approx 13\%$.

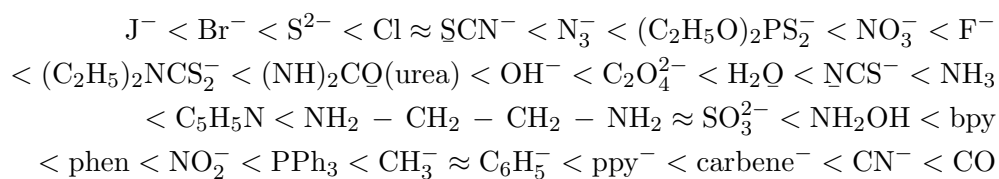
resonances as a function of the excitation yield f are shown in Fig. E.3 and illustrate a linear progression. Moreover, the plotted values of the absolute difference $\Delta A = |A_{\text{ES}}^{\text{edge}} - 5/4 \cdot A_{\text{GS}}^{\text{edge}}|$ exhibits a minimum around $f(t) \approx 13\%$.

Based on this ionic approximation the excitation yield in the experiments is determined to $\approx 13\%$. Since the L_2 -edge spectroscopy was performed at the same laser fluence level, this excitation yield is used for all experiments performed in the framework of this thesis.

E. Calculation of the Excitation Yield

F. Spectrochemical Series

The spectrochemical series and the corresponding description reported in the literature¹³ is shown below.



The series describes the ordering of the ligands based on their potential to induce crystal field splittings $10Dq$. In more detail, the series is starting with so-called *weak ligands* inducing small crystal field splittings and evolves further to so-called *strong ligands*, which in turn induce strong splittings. The ordering of the ligands can vary slightly due to their different binding properties in different complexes and the literature further emphasizes that "the positions of $(\text{ppy})^-$ and carbenes^- are only given tentatively".

Acknowledgments

First of all, I am very thankful to my family for all the support I have experienced within my PhD studies.

Furthermore, I would like to express my thankfulness to my supervisors Prof. Dr. Edgar Weckert and Dr. Alke Meents for giving me the opportunity to work at DESY in the research field of pump-probe experiments.

In particular I thank Edgar for always keeping his door open for my concerns despite his busy schedule. His advice on several scientific aspects helped significantly to realize this thesis.

I thank Alke for the intense supervision during and after the experiments and for creating the nice working atmosphere in the P11 group. His permanent accessibility through day and night times and his visionary thoughts and improvisational skills on different experimental topics had a significant impact for the outcome of this thesis. In addition, I thank Alke for giving me the opportunity to be an elemental part of the software development team at the beamline.

I sincerely thank Prof. Dr. Markus Drescher for taking over the second opinion of my thesis.

In an overall picture this thesis is the result of a long journey through various different scientific and engineering disciplines in which I experienced great help and support from other people. Many thanks go to:

- Philip Roedig for the strong and never-ending support during my beamtimes, many interesting and important scientific discussions and for reading of my complete thesis.
- My former colleagues Dr. Benjamin Dicke and Dr. Moritz Schlie for many endlessly hard pioneering and commissioning beamtimes we shared together at PETRA III.
- Dr. Sebastian Schulz for introducing me into the world of phase noise and timing jitter as well as many fruitful advice concerning the analysis of phase noise spectra. I also thank him for reading parts of my thesis and for providing the signal source analyzer on various occasions.
- The complete P11 crew for the nice working atmosphere at the beamline as well

F. Spectrochemical Series

as the support before, during and after the beamtimes. In particular I thank my office colleague Nicolas Stübe for realizing many CAD drawings related to the XAFS setup on extremely fast time scales and Jan Meyer for the significant help during the hardware and software commissioning of the experiment. Furthermore, I am thankful to Tim Pakendorf for the help with the kHz-sampled XBPM measurements and Jan Roever for the CAD drawing of the APD shielding.

- Dr. Wojciech Gawelda, Prof. Dr. Christian Bressler, Dr. Grigory Smolentsev and Prof. Dr. Frank de Groot for many inspiring discussions and advice during the analysis.
- Sebastian Bommel, Dr. Anja Burkhardt and Dr. Desiree Heintz for many scientific discussions related to my research field and other topics.
- Patrick Geßler for the support during the hardware testing of the gated integrator.
- Tadesse Assefa and Alexander Britz for their support during my last beamtime and for reading parts of my thesis.
- Dr. Olga Lorbeer and Dr. Resmi Raghunandan for their support in the chemistry labs.
- Dr. Jens Viehhaus for many experimental advice and his interest in our experiments.
- Dr. Andre Rothkirch for several advice concerning computer related problems.
- Boris Steffen for the support during the first XBPM installation.
- My former office colleague Dr. Michael Schulz for the nice atmosphere and many interesting discussions concerning laser physics.
- The workshops for the manufacturing of many parts of the setup and other wishes in time.

Thanks!

Selbstständigkeitserklärung

Ich erkläre, dass ich die vorliegende Arbeit selbstständig und nur unter Verwendung der angegebenen Quellen und persönlichen Mitteilungen angefertigt habe.

Hamburg, 2014

Dennis Görjes

Bibliography

- [1] W. C. RÖNTGEN, "*Eine neue Art von Strahlen*", Stahel **2nd** Edition, Würzburg, (1896).
- [2] F. W. LYTLE, "*The EXAFS family tree: a personal history of the development of extended X-ray absorption fine structure*", Journal of Synchrotron Radiation, Vol. **6**, 123-134 (1999).
- [3] C. BRESSLER and M. CHERGUI, "*Molecular Structural Dynamics Probed by Ultrafast X-Ray Absorption Spectroscopy*", Annu. Rev. Phys. Chem, Vol. **61**, 263-282 (2010).
- [4] L. X. CHEN, "*Taking Snapshots of Photoexcited Molecules in Disordered Media by Using Pulsed Synchrotron X-rays*", Angewandte Chemie Int. Ed., Vol. **43**, 2886-2905 (2004).
- [5] I. B. BERSUKER, "*Electronic Structure and Properties of Transition Metal Compounds: Introduction to the Theory*", John Wiley & Sons, **2nd** Edition, (2010). ISBN 0-47018-023-4.
- [6] B. DICKE, "*Time-resolved pump probe XAFS Spectroscopy of Gaq3*", PhD. Thesis, University of Hamburg, (2013).
- [7] M. SCHLIE, "*Time-resolved studies at PETRA III with a highly repetitive synchronized laser system*", PhD. Thesis, University of Hamburg, (2013).
- [8] F. SCHOTTE, J. SOMAN, J. S. OLSON, M. WULFF and P. A. ANFINRUD, "*Picosecond time-resolved X-ray crystallography: probing protein function in real time*", Journal of Structural Biology, Vol. **147**, 235-246 (2004).
- [9] W. GAWELDA, M. JOHNSON, F. M. F. DE GROOT, R. ABELA, C. BRESSLER and M. CHERGUI, "*Electronic and Molecular Structure of Photoexcited $[Ru^{II}(bpy)_3]^{2+}$ Probed by Picosecond X-ray Absorption Spectroscopy*", Journal American Chemical Society, Vol. **128**, 5001-5009 (2006).
- [10] M. SAES, C. BRESSLER, R. ABELA, D. GROLIMUND, S. L. JOHNSON, P. A. HEIMANN and M. CHERGUI, "*Observing photochemical Transients by Ultrafast X-ray Absorption Spectroscopy*", Phys. Rev. Lett., Vol. **90**, 047403 (2003).
- [11] EUROPEAN XFEL, <http://www.xfel.eu/>.
- [12] H. T. LEMKE, C. BRESSLER, L. X. CHEN, D M. FRITZ, K. J. GAFFNEY, A. GALLER, W. GAWELDA, K. HALDRUP, R. W. HARTSOCK, H. IHEE, J. KIM, K. H. KIM, J. H. LEE, M. M. NIELSEN, A. B. STICKRATH, W. ZHANG, D.

Bibliography

- ZHU and M. CAMMARATA, "Femtosecond X-ray Absorption Spectroscopy at a Hard X-ray Free Electron Laser: Application to Spin Crossover Dynamics", *J. Phys. Chem. A*, Vol. **117**, 735-740 (2013).
- [13] H. YERSIN and W. J. FINKENZELLER, "Highly Efficient OLEDs with Phosphorescent Materials", Wiley-VCH Verlag GmbH & Co, 1st Edition (2007), ISBN 3-52740-594-1.
- [14] C. ULBRICHT, B. BEYER, C. FRIEBE, A. WINTER and U. S. SCHUBERT, "Recent Developments in the Application of Phosphorescent Iridium(III) Complex Systems", *Advanced Materials*, Vol. **21**, 4418-4441 (2009).
- [15] T. HOFBECK and H. YERSIN, "The Triplet State of *fac*-Ir(ppy)₃", *Inorganic Chem.*, Vol. **49**, 9290-9299 (2010).
- [16] G. Y. PARK, J.-H. SEO, Y. K. KIM, Y. S. KIM and Y. HA, "New Heteroleptic Tris-Cyclometalated Iridium(III) Complexes Containing Difluorophenylpyridine and Phenylpyridine", *Journal of the Korean Physical Society*, Vol. **50**, 1729-1734 (2007).
- [17] J. FINE, K. DIRI, A.I. KRYLOV, C. NEMIROW, Z. LU and C. WITTIG, "Electronic structure of tris(2-phenylpyridine)iridium: electronically excited and ionized states", *Molecular Physics*, Vol. **110**, 1849-1862 (2012).
- [18] J. BREU, P. STÖSSEL, S. SCHRADER, A. STARUKHIN, W. J. FINKENZELLER and H. YERSIN, "Crystal Structure of *fac*-Ir(ppy)₃ and Emission Properties under Ambient Conditions and at High Pressure", *Chemistry of Materials*, Vol. **17**, 1745-1752 (2005).
- [19] W. J. FINKENZELLER and H. YERSIN, "Emission of Ir(ppy)₃. Temperature dependence, decay dynamics, and magnetic field properties", *Chemical Physics Letters*, Vol. **377**, 299-305 (2003).
- [20] G. J. HEDLEY, A. RUSECKAS and I. D. W. SAMUEL, "Ultrafast luminescence in Ir(ppy)₃", *Chemical Physics Letters*, Vol. **450**, 292-296 (2008).
- [21] K. NOZAKI, "Theoretical Studies on Photophysical Properties and Mechanism of Phosphorescence in [*fac*-Ir(2-phenylpyridine)₃]", *Journal of the Chinese Chemical Society*, Vol. **53**, 101-112 (2006).
- [22] G. J. HEDLEY, A. RUSECKAS and I. D. W. SAMUEL, "Ultrafast Intersystem Crossing in a Red Phosphorescent Iridium Complex", *Journal of Physical Chemistry Letters A*, Vol. **113**, 2-4 (2009).
- [23] M. NEWVILLE, "Fundamentals of XAFS", <http://xafs.org/Tutorials>, Consortium for Advanced Radiation Sources, Revision **1.7**, 23 July, (2004).
- [24] M. NEWVILLE, "Fundamentals of X-ray Absorption Fine Structure", <http://xafs.org/Tutorials>, Consortium for Advanced Radiation Sources, Version **1.6.1**, 20 July, (2005).

- [25] S. R. BARE, "XANES Measurements and Interpretation", http://cars9.uchicago.edu/xafs_school/APS_2005/Bare_XANES.pdf, UOP LLC, EXAFS Data Collection and Analysis Course, July 26-29 (2005). Last access: May 5th, (2013)
- [26] F. SETTE, J. STÖHR and A. P. HITCHCOCK, "Determination of intramolecular bond lengths in gas phase molecules from K shell shape resonances", The Journal of Chemical Physics, Vol. **81**, 4906-4914 (1984).
- [27] J. J. REHR and R. C. ALBERS, "Theoretical approaches to x-ray absorption fine structure", Reviews of Modern Physics, Vol. **72**, No. **3**, 621-654 (2000).
- [28] G. BUNKER, "Introduction to XAFS", Cambridge University Press, 1st Edition (2010). ISBN 0-521-76775-0.
- [29] E. A. STERN, "Theory of the extended x-ray-absorption fine structure", Phys. Rev. B, **10**, 3027-3037 (1974).
- [30] D. C. KONINGSBERGER and R. PRINS, "X-ray Absorption: Principles, Applications, Techniques of EXAFS, SEXAFS and XANES", John Wiley & Sons, Chemical Analysis Vol. **92** (1988). ISBN 0-471-87547-3.
- [31] T. M. HAYES and J. B. BOYCE, "Extended X-Ray Absorption Fine Structure Spectroscopy", Solid State Physics, Vol. **37**, 173351 (1983).
- [32] C. BRESSLER, M. SAES, M. CHERGUI, D. GROLIMUND and R. ABELA, "Towards structural dynamics in condensed chemical systems exploiting ultrafast time-resolved X-ray absorption spectroscopy", The Journal of Chemical Physics, Vol. **116**, 2955-2966 (2002).
- [33] M. SAES, "Picosecond X-ray Absorption Spectroscopy: Application to Coordination Compounds in Solution", PhD. Thesis **2970**, EPFL, Lausanne (2004).
- [34] W. GAWELDA, "Time-resolved X-ray Absorption Spectroscopy of Transition Metal Complexes", PhD. Thesis **3673**, EPFL, Lausanne (2006).
- [35] X-RAY ORIENTED PROGRAMS, "XOP on-line documentation", <http://www.esrf.eu/computing/scientific/xop2.1/>, Access: November 2013. Last Access: June 11th, 2014.
- [36] J. WONG, F. W. LYTLE, R. P. MESSMER and D. H. MAYLOTTE, "K-edge absorption spectra of selected vanadium compounds", Physical Review B, Vol. **30**, 5596-5610 (1984).
- [37] T. K. SHAM, "X-ray Absorption Spectra of Ruthenium L Edges in $Ru(NH_3)_6Cl_3$ ", Journal of the American Chemical Society, Vol. **105**, 2269-2273 (1983).
- [38] D. E. SAYERS, E. A. STERN and F. W. LYTLE, "New Technique for Investigating Noncrystalline Structures: Fourier Analysis of the Extended X-Ray - Absorption Fine Structure", Physical Review Letters, Vol. **27**, No. **18**, 1204-1207 (1971).

Bibliography

- [39] J. J. REHR, J. J. KAS, M. P. PRANGE, A. P. SORINI, Y. TAKIMOTO and F. VILA, "Ab initio theory and calculations of X-ray spectra", *Comptes Rendus Physique*, Vol. **10**, 548-559 (2009).
- [40] X-RAY DATA BOOKLET, "Center for X-ray Optics and Advanced Light Source", <http://xdb.lbl.gov/>, Lawrence Berkeley National Laboratory, Access: November 2013.
- [41] M. O. KRAUSE, "Atomic Radiative and Radiationless Yields for K and L Shells", *J. Phys. Chem. Ref. Data*, Vol. **8** No. **2**, 307 (1979).
- [42] D. HASKEL, "FLUO: Correcting XANES for self-absorption in fluorescence measurements", <http://xafs.org/Experiment/OverAbsorption>, May **27** (1999). Access: January 2014. Last Access: May **14th** (2014).
- [43] D. M. PEASE, D. L. BREWE, Z. TAN, J. I. BUDNICK and C. C. LAW, "Accurate x-ray absorption spectra obtained from concentrated bulk samples by fluorescence detection", *Phys. Lett. A*, Vol. **138**, 230-234 (1989).
- [44] J. JAKLEVIC, J. A. KIRBY, M. P. KLEIN, A. S. ROBERTSON, G. S. BROWN and P. EISENBERGER, "Fluorescence Detection of EXAFS: Sensitivity enhancement for dilute species and thin films", *Solid State Communications*, Vol. **23**, 679-682 (1977).
- [45] M. SAES, F. VAN MOURIK, W. GAWELDA, M. KAISER, M. CHERGUI ET AL. and C. BRESSLER, "A setup for ultrafast time-resolved X-ray absorption spectroscopy", *Review of Scientific Instruments*, Vol. **75**, 24-30 (2004).
- [46] LOOKCHEM INFOMARTION, <http://www.lookchem.com/cas-949/94928-86-6.html>, Access: January 2014. Last Access: May **14th** (2014).
- [47] SIGMA-ALDRICH CO., <http://www.sigmaaldrich.com>, Access: (09/2013).
- [48] G. A. LAWRENCE, "Introduction to Coordination Chemistry", John Wiley & Sons, 1st Edition (2010), ISBN 0-470-51931-2.
- [49] B J. VOLICER and S. F. TELLO, "d-Metal Complexes", <http://faculty.uml.edu/ndeluca/84.334/topics/topic6.htm>, Access: August 2013. Last Access: June **11th** (2014).
- [50] M. GERLOCH and E.G. CONSTABLE, "Transition Metal Chemistry: The Valence Shell in d-Block Chemistry", Wiley-VCH, (1994). ISBN 3-527-29218-7.
- [51] G. SMOLENTSEV, *Private Communication*, December **2nd**, (2013).
- [52] PETRA III INTRODUCTION, "PETRA III Facility Information", http://photon-science.desy.de/facilities/petra_iii/facility_information/index_eng.html and <http://petra3.desy.de>, Access: July 2013.

- [53] K. BALEWSKI, W. BREFELD, W. DECKING, H. FRANZ, R. RÖHLSBERGER and E. WECKERT, "*PETRAIII: A Low Emittance Synchrotron Radiation Source (2004)*", http://petra3-project.desy.de/general/tdr/index_eng.html, Hamburg Germany, Access: October 2013.
- [54] G. MARGARITONDO, "*Elements of Synchrotron Light*", Oxford University Press, 1st Edition, (2002), ISBN 0-19-850930-8.
- [55] MACHINE PARAMETERS PETRA III (DESIGN VALUES), "*Machine Parameters PETRA III (Design Values)*", http://photon-science.desy.de/facilities/petra_iii/machine/parameters/index_eng.html, Last access: January, 2014.
- [56] P11 INTRODUCTION, "*P11 - The Bio-Imaging and Diffraction beamline at PETRA III*", http://photon-science.desy.de/facilities/petra_iii/beamlines/p11_bio_imaging_and_diffraction/index_eng.html, Access: January, 2014. Last access: January, 2014.
- [57] J. ALS-NIELSEN and D. MCMORROW, "*Elements of Modern X-Ray Physics*", John Wiley & Sons, 1st Edition (2010). ISBN 0-471-49858-0.
- [58] P11 PARAMETERS, "*P11 - Unified Data Sheet*", http://photon-science.desy.de/facilities/petra_iii/beamlines/p11_bio_imaging_and_diffraction/unified_data_sheet_p11/index_eng.html, Access: January, 2014.
- [59] P. KIRKPATRICK and A. V. BAEZ, "*Formation of Optical Images by X-Rays*", Journal of the Optical Society of America **38**, 766-774 (1948).
- [60] T. PAKENDORF and A. MEENTS, *Private Communication*, May **16th**, (2013) and (2014).
- [61] W. H. BRAGG and W. L. BRAGG, "*X rays and crystal structure*", London G. Bell, **3rd** Edition (1918).
- [62] P. FISCHER, *Private Communication*, (2013).
- [63] PHAROS INFORMATION, "*PHAROS Description and Datasheet*", <http://lightcon.com>, Access: July 2013. Last Access: May **14th** (2014).
- [64] PHAROS MANUAL, "*PHAROS User Manual*", Version: March **7th**, (2014).
- [65] LIGHT CONVERSION, "*PHAROS Service Report*", *Private Communication*, March (2012).
- [66] P. ROEDIG, D. GOERIES, B. DICKE, N. STUEBE, J. MEYER, E. WECKERT and A. MEENTS, *Time-Resolved XAFS Experiments at PETRA III Beamline P11*, Photon Science User Meeting 2014.
- [67] CHIRPED-PULSE AMPLIFICATION, http://www.rp-photonics.com/chirped_pulse_amplification.html, Last Access: June **11th**, 2014.

Bibliography

- [68] R. L. OWEN, J. M. HOLTON, C. SCHULZE-BRIESE and E. F. GARMAN ,
"Determination of X-ray flux using silicon pin diodes", J. Synchrotron Rad. **16**,
143-151 (2009).
- [69] T. KRACHT and H. ZINK, "The VFC-ADC, a Programmable ADConverter",
[http://hasyweb.desy.de/science/annual_reports/2005_report/part1/
contrib/27/15460.pdf](http://hasyweb.desy.de/science/annual_reports/2005_report/part1/contrib/27/15460.pdf), Access: January, 2014. Last Access: June **11th**, 2014.
- [70] ORTEC, "Quad 200-MHz Constant-Fraction Discriminator",
www.ortec-online.com.
- [71] FMB OXFORD DATA SHEET, "APD-ACE Pulse Processing Unit User Manual",
FMB Oxford, Issue. **3.0**, DOCM0101 (2011).
- [72] FMB OXFORD DATA SHEET, "Avalanche Photodiode Detector Head: APD
Head 5 x 5 mm² User Manual", FMB Oxford, Issue. **2.0**, DOCM0102 (2010).
- [73] I. POOLE, "Photodiode Operation & Theory",
[http://www.radio-electronics.com/info/data/semicond/photo_diode/
operation-theory.php](http://www.radio-electronics.com/info/data/semicond/photo_diode/operation-theory.php), Access: March, 2014. Last Access: May **14th**, 2014.
- [74] A. R. J. MARSHALL, J. P. R. DAVID and C. HING TAN, "Impact Ionization in
InAs Electron Avalanche Photodiodes", IEEE Transactions on Electron Devices,
Vol. **57**, No. **10**, 2631 - 2638 (2010).
- [75] K. J. ÅSTRÖM and T. HÄGGLUND, "PID Controllers: Theory, Design, and
Tuning", **2nd** Edition (1995), ISBN 1-55617-516-7.
- [76] J. ZHONG, "PID Controller Tuning: A Short Tutorial", Mech. Eng., Purdue
University, (2006).
- [77] L. DICKSTEIN, "Introduction to Phase Noise in Signal Generators",
www.gigatronics.com/uploads/document/, White Paper **AN-GT140A**,
Access: October 2013; Last access: May **5th**, (2013).
- [78] I. POOLE, "RF Phase Noise & Phase Jitter Tutorial",
[http://www.radio-electronics.com/info/rf-technology-design/
phase-noise-jitter/basics-tutorial.php](http://www.radio-electronics.com/info/rf-technology-design/phase-noise-jitter/basics-tutorial.php) (an following pages), Access:
October 2013; Last access: May **5th**, (2013).
- [79] S. SCHULZ, *Private Communication*, (2012-2013).
- [80] S. SCHULZ, "Implementation of the Laser-Based Femtosecond Precision
Synchronization System at FLASH", PhD. Thesis, University of Hamburg,
(2013).
- [81] R. PASCHOTTA, "Noise of mode-locked lasers (Part I): numerical model", Appl.
Phys. B **79**, 153-162 (2004).
- [82] R. PASCHOTTA, "Noise of mode-locked lasers (Part II): timing jitter and other
fluctuations", Appl. Phys. B **79**, 163-173 (2004).
- [83] LIGHT CONVERSION, *Private Communication*, March **8th**, (2012).

- [84] MENLO SYSTEMS, "*RRE - Custom Repetition Rate Stabilization*", User Manual, www.menlosystems.com, Version **1.0**, October (2011).
- [85] MENLO SYSTEMS, "*DDS - Direct Digital Synthesizer*", User Manual, www.menlosystems.com, Version **1.0**, January (2009).
- [86] A. WINTER, F. Ö. ILDAY, O.D. MÜCKE, R. ELL, H. SCHLARBB, P. SCHMÜSER and F.X. KÄRTNER, "*Towards high-performance optical master oscillators for energy recovery linacs*", Nuclear Instruments and Methods in Physics Research A, Vol. **557**, 299-304 (2006).
- [87] B. STEFFEN, *Private Communication*, August **10th**, (2012); July **3rd** (2013).
- [88] PYTHON SOFTWARE FOUNDATION, "*Python Programming Language: Official Website*", <http://www.python.org/>, Access: April 2013.
- [89] TANGO CONTROLS SYSTEM, "*TANGO: Official Website*", <http://www.tango-controls.org/>, Access: April 2013.
- [90] A. L. STANCIK and E. B. BRAUNS, "*A simple asymmetric lineshape for fitting infrared absorption spectra*", Vibrational Spectroscopy, Vol. **47**, 66-69 (2008).
- [91] A. BELAFHAL, "*The shape of spectral lines: widths and equivalent widths of the Voigt profile*", Optics Communications, Vol. **177**, 111-118 (2000).
- [92] M. O. KRAUSE and J. H. OLIVER, "*Natural Width of Atomic K and L Levels, K_{α} X-ray Lines and Several KLL Auger Lines*", J. Phys. Chem. Ref. Data, Vol. **8** No. **2**, 329-338 (1979).
- [93] C. SUGIURA, M. KITAMURA and S. MURAMATSU, "*Xray absorption near edge structure of complex compounds $(NH_4)_3RhCl_6$, K_3RuCl_6 , and $Ru(NH_3)_6Cl_3$* ", The Journal of Chemical Physics, Vol. **84**, 4824-4827 (1986).
- [94] A. V. PENDHARKAR and C. MANDE, "*Molecular Orbital Interpretation of the Rhenium L_3 Absorption Discontinuity in some Compounds*", The Journal of Chemical Physics, Vol. **7**, 244-254 (1975).
- [95] B. RAVEL, "*Demeter: A comprehensive system for processing and analyzing X-ray Absorption Spectroscopy data*", <http://bruceravel.github.io/demeter/>, Access: December 2013. Last Access: June **11th**, 2014.
- [96] B. RAVEL and M. NEWVILLE, "*ATHENA, ARTEMIS, HEPHAESTUS: Data analysis for X-ray absorption spectroscopy using IFEFFIT*", Journal of Synchrotron Radiation, Vol. **12**, 537-541 (2005).
- [97] C. R. NATOLI, M. BENFATTO and S. DONIACH, "*Use of general potentials in multiple-scattering theory*", Physical Review A, Vol. **34**, 4682-4694 (1986).
- [98] S. TAKAYASU, T. SUZUKI and K. SHINOZAKI, "*Intermolecular Interactions and Aggregation of fac-Tris(2-phenylpyridinato- C^2,N)iridium(III) in Nonpolar Solvents*", The Journal of Physical Chemistry B, Vol. **117**, 9449-9456 (2013).

Bibliography

- [99] W. HOLZER, A. PENZKOFER and T. TSUBOI, "Absorption and emission spectroscopic characterization of $Ir(ppy)_3$ ", Chemical Physics, Vol. **308**, 93-102 (2005).
- [100] S. REINEKE, K. WALZER and K. LEO, "Triplet-exciton quenching in organic phosphorescent light-emitting diodes with Ir-based emitters", Physical Review B, Vol. **75**, 125328 (2007).
- [101] B. H. MILOSAVIJEVIC and J. K. THOMAS, "Photochemistry of Compounds Adsorbed into Cellulose. 1. Decay of Excited Tris(2,2-bipyridine)ruthenium(II)", Journal of Physical Chemistry, Vol. **87**, 616-621 (1983).
- [102] I. ALPEROVICH, G. SMOLENTSEV, D. MOONSHIRAM, J. W. JURSS, J. J. CONCEPCION, T. J. MEYER, A. SOLDATOV and Y. PUSHKAR, "Understanding the Electronic Structure of 4d Metal Complexes: From Molecular Spinors to L-Edge Spectra of a di-Ru Catalyst", Journal of the American Society, Vol. **133**, 15786 (2011).
- [103] E. KÖNIG and K. J. WATSON, "The Fe-N bond lengths, the ionic radii of iron (II), and the crystal field parameters (10Dq) in a high-spin and low-spin [FeII-N6] complex", Chemical Physics Letters, Vol. **6**, 457-459 (1970).
- [104] F.M.F. DE GROOT, "Multiplet effects in X-ray spectroscopy", Coordination Chemistry Reviews, Vol. **249**, 31-63 (2005).
- [105] E. STAVITSKI and F.M.F. DE GROOT, "The CTM4XAS program for EELS and XAS spectral shape analysis of transition metal L edges", Micron, Vol. **41**, 687-694 (2010).
- [106] F. BRIDGES, J.B. BOYCE and X. WANG, "Minimizing "glitches" in XAFS data: A model for glitch formation", Nuclear Instruments and Methods in Physics Research A, Vol. **307**, 316-324 (1991).
- [107] O. LORBEER, *Private Communication*, October **17th**, (2013).
- [108] M. POPE and C. E. SWENBERG, "Electronic Processes in Organic Crystals and Polymers", Oxford University Press, **2nd** Edition (1999), ISBN 0-19512-963-6.